POLITECNICO
MILANO 1863

SCUOLA DI INGEGNERIA INDUSTRIALE
E DELL'INFORMAZIONE

SmallSats Mars Aerocapture Optimal Guidance with Direct Force Control

Tesi di Laurea Magistrale in
Space Engineering - Ingegneria Spaziale

Author: **Iñigo Prieto Boveda**

Student ID: 964514
Advisor: Prof. Michèle Roberta Lavagna
Co-advisors: Daniele Barberi Spirito
Academic Year: 2022-23

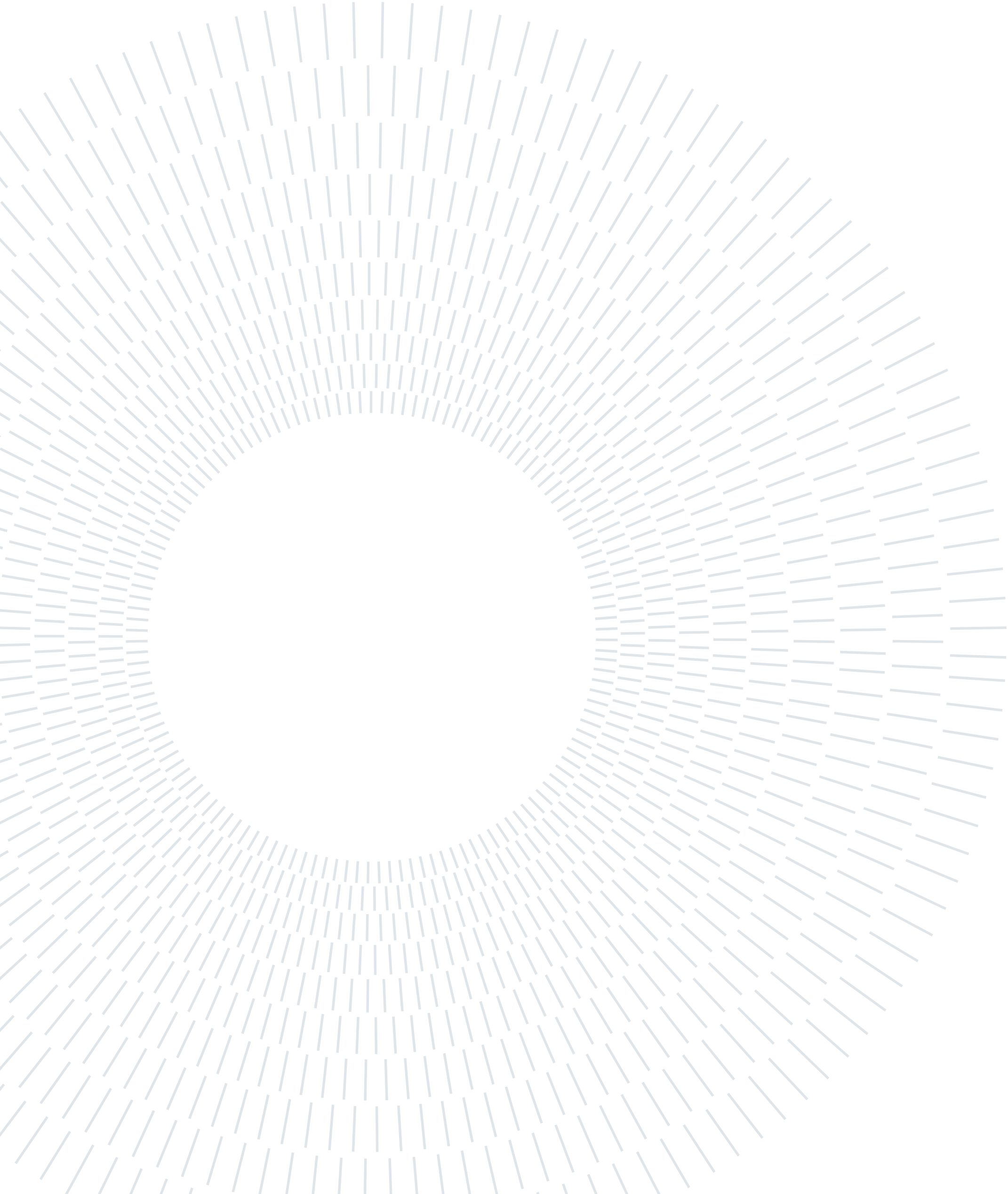

Abstract

Main developed aerocapture guidance control schemes suffer on correctly controlling the longitudinal and lateral channels (in and out of plane targets, respectively). While the most common Bank Angle Modulation suffers from a coupling between the two channels, as it only exerts a single control variable, Drag Modulation directly lacks the lateral control.

As a result, the Direct Force Control approach arises to separate them, introducing two decoupled control variables, improving the manoeuvre performance capabilities. The control variables are not found to get saturated throughout the trajectory, which also leads to higher robustness against atmospheric uncertainty. However, this control strategy is relatively new, and studies on small satellite integration have yet to be conducted. Hence, its feasibility in applying to small Mars ride-share satellite missions for aeroshell capsule-like vehicles is studied, and an optimality-based NPC guidance scheme is developed. Expected advantages of the system will be confronted with the obtained results. Algorithm performance validation, sensitivity navigation uncertainty analysis, and Monte Carlo simulations will be conducted to verify the system's robustness, reliability, and performance.

Aerocapture is found to provide a mission enabler technology, with the already-existing state-of-the-art performance when sized in comparison to the fully-propulsive capture. Lower target orbits are better suited for Direct Force Control applied to small satellite aeroshell-like vehicles. Finally, the critical points of the developed study identified technological bottlenecks, and future developments are suggested.

Keywords: Mars Aerocapture, Optimal NPC Guidance, Direct Force Control, Aeroshell Capsule SmallSat aerocapture, Optimal Aerocapture.

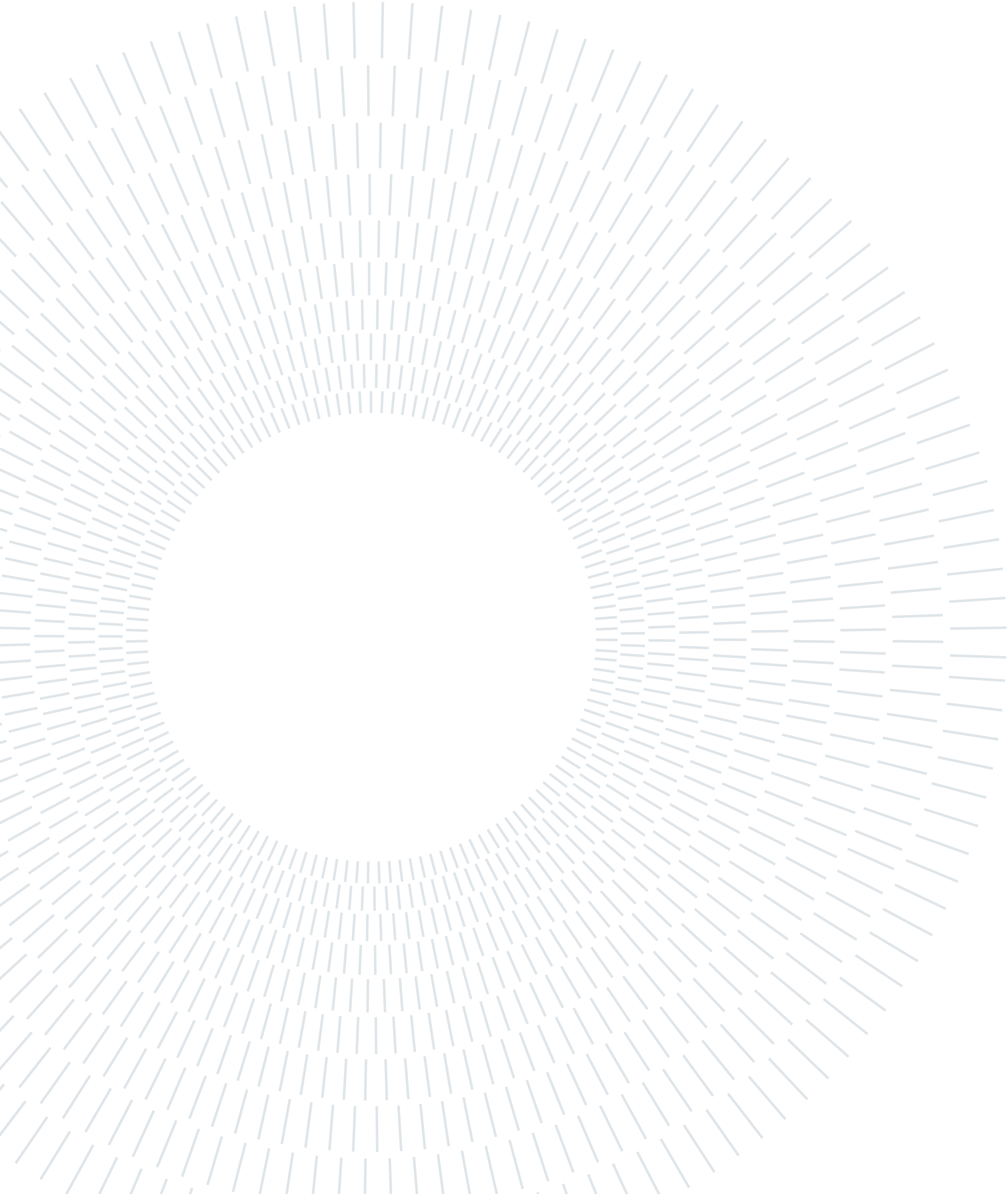

Abstract in lingua italiana

I principali schemi di guida e controllo per l'aerocattura hanno difficoltà nel controllo delle dinamiche longitudinali e laterali (rispettivamente nei target interni ed esteri al piano). Il più comune, il Bank Angle Modulation, soffre di un accoppiamento tra le due dinamiche in quanto esercita il controllo su una sola variabile, mentre il Drag Modulation manca direttamente del controllo laterale.

L'approccio del Direct Force Control può essere usato per separare le due dinamiche, introducendo due variabili di controllo disaccoppiate. Le variabili di controllo non saturano lungo la traiettoria, il che porta ad una maggior robustezza nei confronti dell'incertezza dell'atmosfera. Questa strategia è però relativamente nuova, e studi sull'integrazione in piccoli satelliti devono ancora essere condotti. Perciò, la fattibilità di applicarla a missioni rideshare di small-satellites per Marte è studiata, e uno schema di guida NPC optimality-based è svilupato. I miglioramenti attesi sono confrontati con i risultati ottenuti. Inoltre sono eseguite analisi sulla sensibilità dell'incertezza di navigazione, valutazioni sulle prestazioni dell'algoritmo, simulazioni Monte Carlo, per verificare la robustezza, affidabilità, e prestazioni del sistema.

L'aerocattura risulta essere una mission enabling technology, con prestazioni allo stato dell'arte se paragonate alla cattura completamente propulsiva. Le orbite di arrivo più basse risultano più adatte a un Direct Force Control applicato a piccoli satelliti di tipo aeroshell. Infine, i punti critici dello studio identificano i bottlenecks della tecnologia, e sono suggeriti i possibili futuri sviluppi.

Parole chiave: Aerocattura di Marte, Guida Ottimale NPC, Controllo Diretto Della Forza, Aerocattura di SmallSat con Capsula aeroshell, Aerocattura Ottimale.

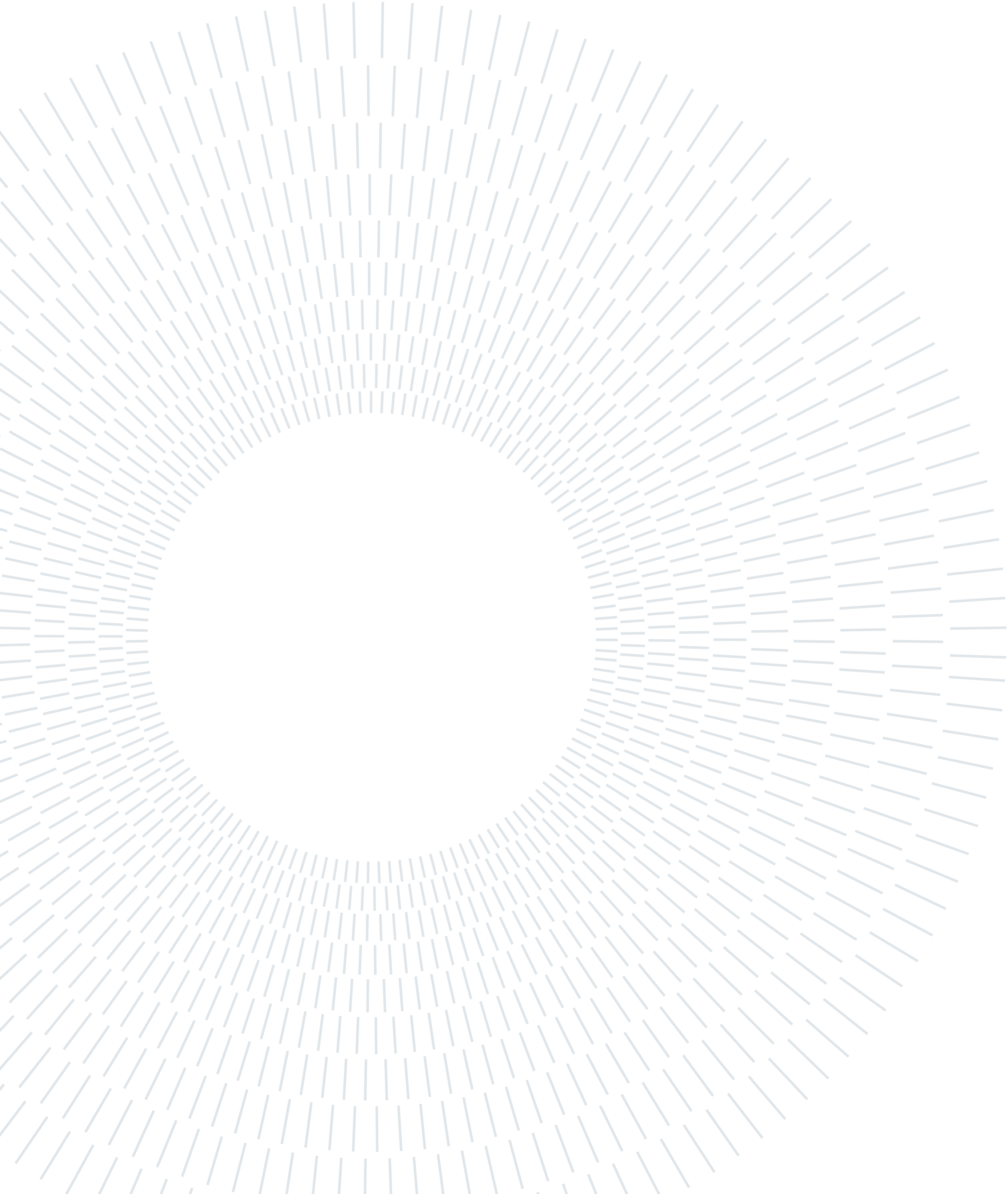

Acknowledgements

I would like to use this opportunity to convey my profound gratitude to Prof. Michèle Lavagna for allowing me to perform this research on the Aerocapture topic and for serving as my thesis advisor. Also, I want to convey my sincere gratitude to Daniele Barberi, my co-advisor, for his assistance, direction, and encouragement throughout the research process. His opinions and feedback have been really beneficial in forming the final thesis outcome.

Giovanni Zanotti and Jacopo Prinetto, PhD researchers at Politecnico di Milano, deserve my gratitude for their readiness to assist me during the research on Navigation and Optimal Control matters. Also, I wish to thank PhD David De La Torre Sangrà from UPC for sharing the MEMM engineering tool with me and giving me insightful recommendations regarding atmospheric modelling.

Finally, I sincerely thank my family, friends, and colleagues for their unwavering support and encouragement during my academic career. Their love, patience, and understanding have been a constant source of motivation and inspiration.

Thank you all for being a part of my academic journey.

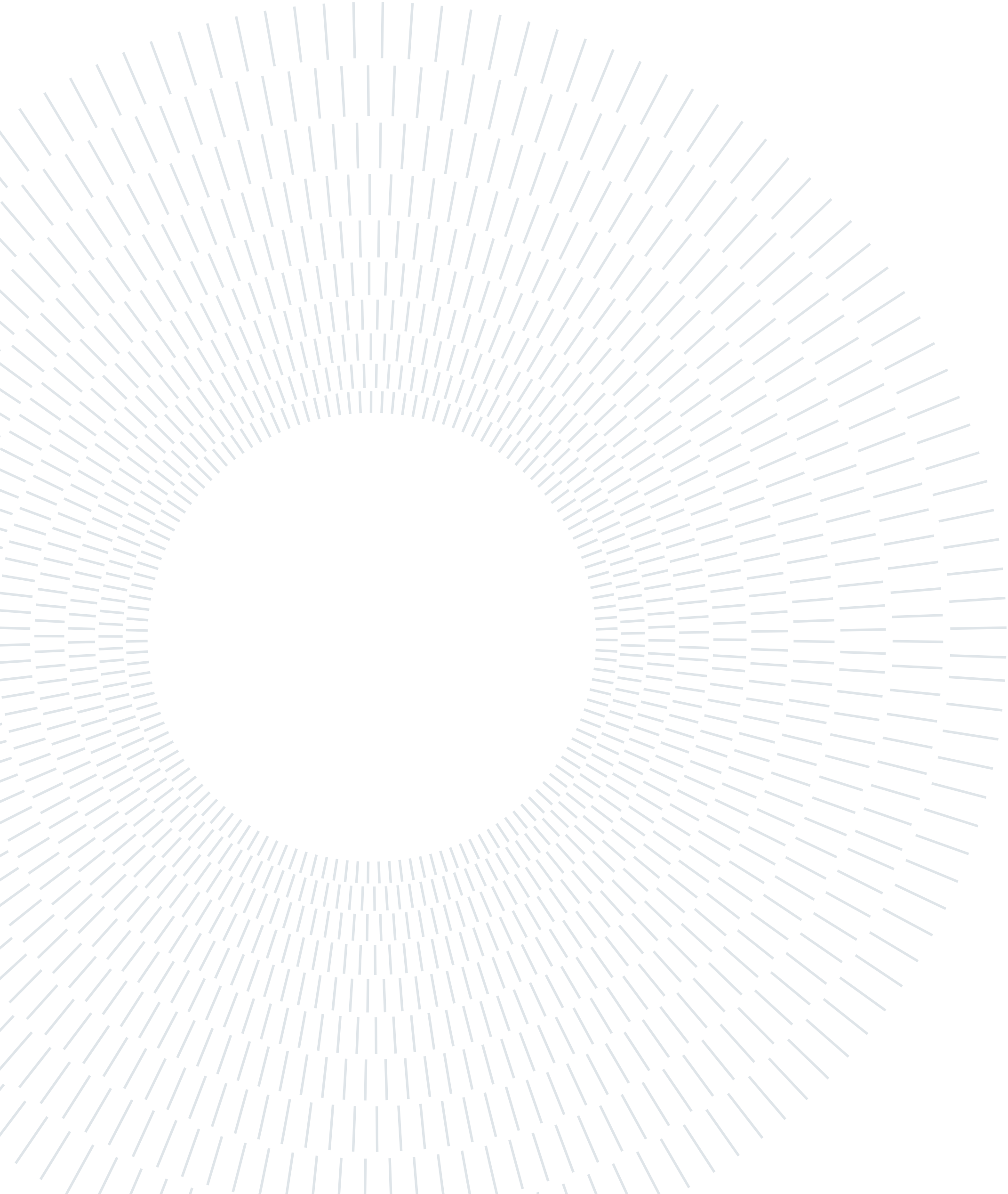

Contents

Abstract i

Abstract in lingua italiana iii

Acknowledgements v

Contents vii

List of Figures xi

List of Tables xv

Acronyms xvii

List of Symbols xix

1 Introduction 1
- 1.1 State-of-The-Art . . . 1
  - 1.1.1 Aerocapture Concept and Evolution . . . 1
  - 1.1.2 Expected Benefits and Risks . . . 3
  - 1.1.3 Small Satellites at Mars . . . 4
  - 1.1.4 GN&C . . . 5
- 1.2 Research Questions . . . 15
- 1.3 Thesis Outline . . . 16

2 Modelling 17
- 2.1 Aerodynamics . . . 17
  - 2.1.1 Low-Density Flow . . . 17
  - 2.1.2 Modelling . . . 18
  - 2.1.3 Code Validation . . . 20
  - 2.1.4 Convergence Analysis . . . 21

2.1.5 1-D Aerodynamic Coefficients 22
2.2 Equations of Motion 23
2.2.1 Relative Spherical 24
2.2.2 Inertial Cartesian 25
2.2.3 Validation 25
2.3 Atmospheric Models 26
2.3.1 Exponential Model 27
2.3.2 Piece-wise Linearization 27
2.4 Aeroheating 28
2.5 Integrators Study 29
2.5.1 Dimensional Dynamics 29
2.5.2 Dimension-less Dynamics 31
2.5.3 Required Computational Time 33
2.5.4 Conclusions 33
2.6 Real System 34
2.6.1 Atmospheric Model 34
2.6.2 Aerodynamic Coefficients 35
2.6.3 Winds Implementation 35
2.7 Fully-Propulsive Computations 37

3 DFC Feasibility for SmallSats at Mars 39
3.1 Introduction 39
3.1.1 Possible Points of Concern 39
3.1.2 Assumptions Made 41
3.1.3 Objective of the Chapter 42
3.2 SmallSats Constraints Definition 43
3.2.1 Spacecraft Category Definition 43
3.2.2 ESPA Rings Constraints 43
3.2.3 Vehicle Constraints 44
3.2.4 Trajectory Constraints 44
3.3 Capsules Parametric Design 45
3.3.1 Design Introduction 45
3.3.2 Aerodynamic Results 47
3.3.3 Conclusions 50
3.4 Nominal Corridors 50
3.4.1 Concept 50
3.4.2 Hyperbolic Parameter Variation Effect 53

3.4.3 ESPA-Grande and ESPA-Compatible Radius of Apoapsis Variation 54
3.4.4 Mass Variation Effect 56
3.4.5 Entry Conditions Effect 56
3.4.6 Summary of Nominal Corridor Conclusions 57
3.5 Test Mission Selections 57
3.5.1 Capsule Selection 58
3.5.2 Operational Corridor and Feasible Region 58

4 Guidance 65
4.1 Optimal Control Problem 65
4.1.1 Problem Statement 65
4.1.2 Longitudinal Channel Resolution 67
4.1.3 Weighted Optimal 74
4.1.4 Lateral Channel Resolution 78
4.2 Online Guidance 82
4.2.1 OCP Solution Implementation 83
4.2.2 Overall Guidance Architecture 84
4.2.3 NPC 85
4.2.4 Pseudo Actuator 87
4.2.5 Atmospheric Model 88
4.2.6 Navigation Filter 89
4.2.7 Aerodynamic Coefficients 90
4.2.8 Relief Logic 90
4.3 Guidance Failure Cases and Solutions 91
4.3.1 Failure Case 1 92
4.3.2 Failure Case 2 93
4.4 Algorithm Validation 94
4.5 Navigation Dispersion Sensitivity Analysis 95
4.6 Monte Carlo Analysis 97
4.6.1 Test Conditions 97
4.6.2 Obtained Results 99
4.6.3 Sizing and Fully-Propulsive Comparison 103
4.6.4 Conclusions 103

5 Conclusions 105
5.1 Thesis Conclusions 105
5.2 Critical Points 106
5.3 Suggested Future Work 108

Bibliography **A**

A Appendix A - Reference Frames and Transformations **I**
A.1 Reference Frames (RF) Definition I
A.2 Spherical Components Definitions . . . . J
A.3 Frame Transformations . . . . K

B Aerodynamic Results **M**

C Transformation between Cartesian and Rotational Components **S**

D Mars Environment Multi-Model (MEMM) Scientific-Tool **U**

List of Figures

1.1 Original Aerocapture Mission Concept [49] 2
1.2 Modern Aerocapture Mission Concept [13] 3
1.3 Control Variables in Aerocapture [12] 6
1.4 DownRange and CrossRange Representation on a Entry, Descent and Landing Trajectory [74] 7
1.5 DHS Mission with Italian Re-entry Nacelle for Microgravity Experiments (IRENE) drag sail [32] 8

2.1 Knudsen Number Evolution at Mars for SmallSats 18
2.2 Cylinder 21
2.4 Percent Error from Convergence Analysis 22
2.3 Considered Discretizations for Convergence Analysis 22
2.5 Regression Aerodynamic Model EELV Secondary Payload Adapter (ESPA)-Compatible a=1.5 capsule 23
2.6 Absolute Error between Inertial Cartesian and Spherical Rotational Dynamics 26
2.7 Percent Error of Piece-wise Atmospheric Model 28
2.8 Dimensional Variable Step Integrators Convergence fixed ‘AbsTol’=1e-14 . 30
2.9 Dimensional Variable Step Integrators Convergence for Variation on ‘AbsTol’ 31
2.10 Dimensional Fixed Step Convergence Analysis 31
2.11 Dimensionless Step Integrators Convergence Analysis 32
2.11 Dimensionless Step Integrators Convergence Analysis 33
2.12 Computational time for Dimensional and Dimensionless Propagation . . . 34
2.13 ‘ODE113’ Trade-off Analysis 35

3.1 ESPA and ESPA Grande Size Constraints [15] 44
3.2 Hayabusha Design Hyperbolic Parametrization [54] 46
3.3 Vehicle’s Design Trade-offs 46
3.4 Capsule Design 47
3.5 Aerodynamic Coefficients vs Hyperbolic Parameter 48

3.6 Coefficient Error for ESPA Compatible a=1.3 Capsule 49
3.7 Corridor Concept 50
3.8 Atmospheric Expected Interface Velocities [26] 52
3.9 Nominal Corridor Variation for ESPA Hyperbolic Coefficient Variation . . 53
3.10 Nominal Corridor Variation for ESPA and ESPA-Grande r_a Variation . . . 55
3.11 ESPA-Grande Corridor r_a variation 55
3.12 Nominal Corridor for ESPA-Compatible Mass Variation 56
3.12 Circular Target Orbit Feasibility $h_a = 400[km]$ 61
3.12 Elliptical Target Orbit Feasibility $r_a = 33000[km]$ 62

4.1 Smoothing [37] 69
4.2 Splines used in Trapezoidal Method for Control and State approximation [37] 70
4.3 Results of ΔV Optimization 71
4.4 ΔV Optimization Error Estimation 72
4.4 ΔV Optimization Error Estimation 73
4.5 Results of Total Convective Heat Optimization 74
4.6 Total Convective Heat Optimization Error Estimation 75
4.7 Results of Weighted Optimization 76
4.7 Weighted Optimization Error Estimation 77
4.8 Propulsion and Thermal Protective System (TPS) Sizing for trajectory selection 78
4.9 Phases Schematic 84
4.10 Online Guidance General Architecture 85
4.11 Temporal Flow-Chart 86
4.12 Numerical Predictor-Corrector (NPC) Architecture 87
4.13 Phase Identifier 88
4.14 Relief Logic Demonstration 92
4.15 Failure Cases on 25 samples Monte Carlo Analysis 93
4.16 Failure Case 1 Profile 94
4.17 Failure Case 2 Profile 95
4.17 Approach Navigation Error vs Guidance Performance 97
4.18 Online Guidance Commanded Aerodynamic Angle Profiles 101
4.18 Monte Carlo Analysis Trajectory Results 102

5.1 Online Model State Variables Drift 107

A.1 Spherical Parameters Definition [51] . . . . K

B.1 Capsule Design Iterations with hyperbolic parameter Variation . . . . M
B.2 C_Q ESPA and ESPA Grande compatible capsules . . . . N
B.3 C_Q Error on ESPA and ESPA Grande compatible capsules . . . . O
B.4 L/D on ESPA and ESPA Grande compatible capsules . . . . P
B.5 L/D error on ESPA and ESPA Grande compatible capsules . . . . Q
B.6 Reference Surface Loss . . . . R

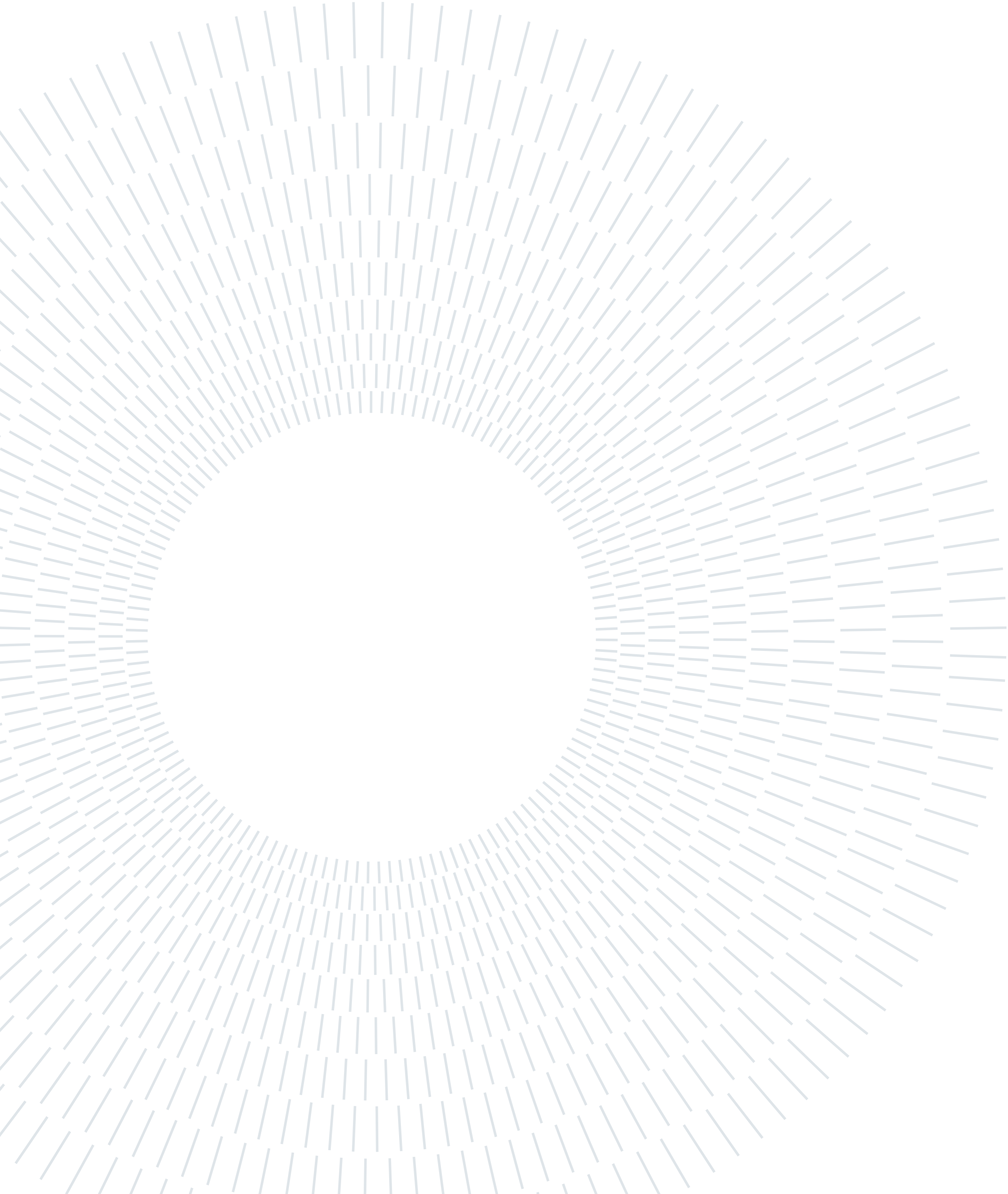

List of Tables

1.1 Pros and Cons of aerocapture trajectory 4
1.2 Aerocapture Guidance Schemes pros and cons summary 15

2.1 Aerodynamics Code Validation Results 21
2.2 Low Velocity Radiation Correlation Polynomial Coefficients. 29
2.3 High Velocity Radiation Correlation Polynomial Coefficients. 29
2.4 Dimensional Variable Step Solver Convergence fixed ‘AbsTol’=1e-14 30

3.1 Qualified ESPA and ESPA Grande contraints [15] 44
3.2 Vehicle Selected Constraints 45
3.3 Test Mission Capsule’s Properties 58
3.4 Feasibility Test 59

4.1 Initial Conditions and Target for Longitudinal Optimization 70
4.2 ΔV Optimal Trajectory Results 72
4.3 Q_{Conv} Optimal Trajectory Results 73
4.4 Control Limiter Values 88
4.5 Monte Carlo Dispersions of [48] 94
4.6 Algorithm Validation Results 95
4.7 Monte Carlo Baseline Dispersion [59][23] 96
4.8 Monte Carlo Dispersions of the Analysis 98
4.9 Monte Carlo Analysis Initial Conditions 99
4.10 Monte Carlo Analysis Target Orbit 99
4.11 Monte Carlo Analysis Results 100
4.12 0.6[deg] Flight Path Angle (FPA) Dispersion Aerocapture vs Fully-Propulsive Capture 103
4.13 0.3[deg] FPA Dispersion Aerocapture vs Fully-Propulsive Capture 103

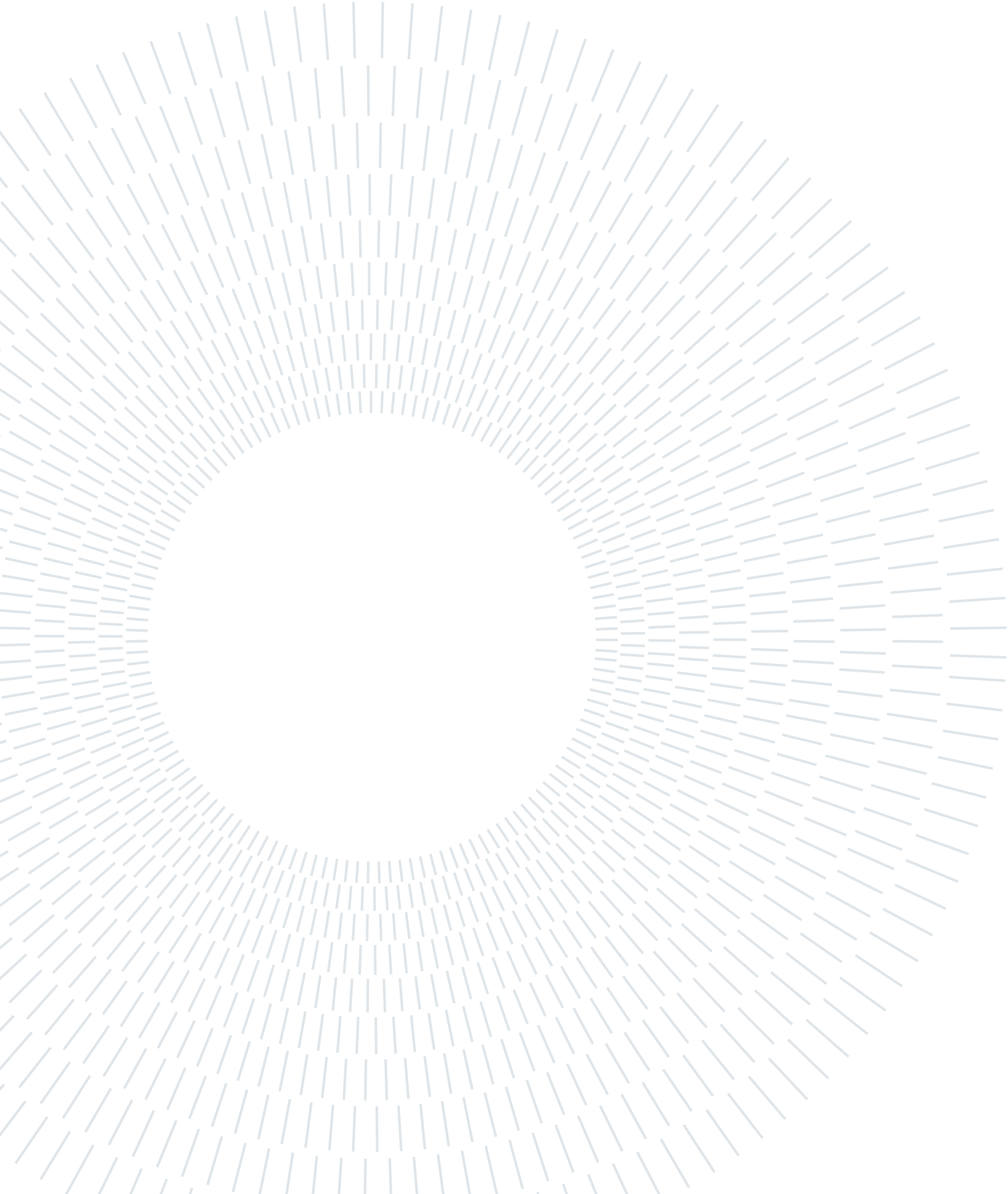

Acronyms

ADEPTS Adaptable Deployable Entry and Placement Technology. xv, 7, 14, 40, 62

AI Atmospheric Interface. xv, 96, 108

AoA Angle of Attack. xv, 84

APC Analytical Predictor-Corrector. xv, 12, 13, 15

ASI Italian Space Agency. xv, 8

AutoNav Autonomous Optical Navigation. xv, 10

BAM Bank Angle Modulation. xv, 6, 11

CNES French Space Agency. xv, 11, 12

DFC Direct Force Control. xv, 8, 22, 35, 50, 63, 67, 88, 94, 104, 105, 106

DM Drag Modulation. xv, 7, 8, 106

DSN Deep Space Network. xv, 10, 97, 106

EDL Entry Descent and Landing. xv, 6, 9

EI Entry Interface. xv, 84, 101

ESPA EELV Secondary Payload Adapter. xi, xii, xv, 5, 21, 23, 43, 44, 45, 47, 49, 54, 55, 56, 58

FADS Flush Air Data Systems. xv, 10

FNPAG Fully Numerical Predictor-corrector Aerocapture Guidance. xv, 11, 94

FPA Flight Path Angle. xv, 14, 50, 53, 73, 75, 77, 93, 99, 100, 101, 102, 103

GN&C Guidance Navigation and Control. xv, 1, 2, 5

GNSS Global Navigation Satellite System. xv, 5

HIADS Hypersonic Inflatable Devices. xv, 7, 40, 62

IMU Inertial Measurement Unit. xv, 10

IRENE Italian Re-entry Nacelle for Microgravity Experiments. xi, xv, 8, 40

MGCM NASA Ames Mars General Circulation Model. xv, 26

MSL Mars Science Laboratory. xv, 7, 14, 40, 44, 95

MTGCM Mars Thermospheric General Circulation Model. xv, 26

NPC Numerical Predictor-Corrector. xii, xv, 12, 14, 15, 16, 33, 34, 82, 83, 84, 85, 86, 87, 89, 93, 104, 107, 108

OpNav Optical Navigation. xv, 10, 106

RCS Reaction Control System. xv, 7

SF Safety Factor. xv, 59, 96

TCM Trajectory Correction Manoeuvre. xv, 90, 107

TPS Thermal Protective System. xii, xv, 1, 3, 4, 13, 40, 77, 78, 103, 105

List of Symbols

Variable	**Description**	**SI unit**
V_∞	Hyperbolic Excess Velocity	km/s
L/D	Lift-to-Drag ratio	
ΔV	Velocity Increment or decrement	m/s
q_∞	Dynamic Pressure	N/m^2
S_{Ref}	Aerodynamic Reference Surface	m^2
C_D	Drag Coefficient	
C_Q	Lateral Coefficient	
C_L	Lift Coefficient	
ρ	Atmospheric Density	kg/m^3
V	Velocity	m/s
r	Radial Distance from the Center of the Planet	m
θ	Longitude	rad
ϕ	Latitude	rad
γ	Planet-relative Flight Path Angle	rad
ψ	Planet-relative Heading Angle	rad
CoG	Center of Gravity	m
Q_{Max}	Maximum Total Heat	J/m^2
n_{Max}	Maximum Load Factor	g
a	Capsule's Hyperbolic Parameter	
R_N	Capsule's Nose Radius	m
α	Angle of attack	rad
β	Side-slip angle	rad
α^*	Optimal Angle of attack	rad
β^*	Optimal Side-slip angle	rad
σ	Bank angle	rad

h	Altitude	m
r_a	Radius of apoapsis	m
r_p	Radius of periapsis	m
r_a^*	Target Radius of apoapsis	m
r_p^*	Target Radius of periapsis	m
a	Orbit Semi-major axis	m
V_I	Inertial Velocty	m/s
μ	Standard Gravitational Parameter of the Planet	m^3/s^2
γ_I	Inertial Flight-Path Angle	rad
ψ_I	Inertial Heading Angle	rad
ω	Planets Rotation rate	rad/s
V_{EI}	Velocity at Atmospheric Interface	m/s
r_0	Initial Radial Distance	m
V_{range}	Range of Velocities	m/s
R_m	Mars Equatorial Radius	m
Φ	Final Trajectory Cost	
$\boldsymbol{x}(t_f)$	Final State	
w	Weight	
$L(\boldsymbol{x})$	Lagragian or Path Cost	
$\dot{\boldsymbol{x}}$	Dynamics	
$\boldsymbol{u}$	Control Vector	rad
$\boldsymbol{x}_0$	Initial State	
t_f	Final Time	s
ΔV_1	Perapsis Raise	m/s
ΔV_2	Apoapsis Correction	m/s
ΔV_3	Inclination Correction	m/s
$\Delta V_{Tot.}$	Total Manoeuvre Cost	m/s
i	Inclination	rad
$\dot{Q}_{Conv.}$	Convective Heat Rate	W/m^2
$Q_{Conv.}$	Convective Total Heat	J/m^2
$\boldsymbol{\lambda}$	Co-state Vector	
$\boldsymbol{\lambda}^*$	Optimal Co-state Vector	
$H(\boldsymbol{x}, \boldsymbol{\lambda})$	Hamiltonian	

y_{α_s}	Hyperbolic Tangent Smoothing Function	
α_s	Smoothing Parameter	
ϵ	Interpolation Error	
$\boldsymbol{\lambda}$	Co-state Vector	
η_k	State error	
t_{TPS}	TPS thickness	m
t_k	Temporal time	s
$\Delta t_{Man.}$	Maneuvering time	s
t_s	Switch time	s
$\dot{u}_{Max}$	Rate Limit	rad/s
$\ddot{u}_{Max}$	Acceleration Limit	rad/s^2
u_0	Initial Control State	rad
$\tilde{\boldsymbol{\rho}}^k$	Temporal State of Navigation Filter Multiplier Vector	
$\boldsymbol{a}_{Aero}^{IMU}$	IMU Measured Aerodynamic Accelerations Vector	m/s^2
$\boldsymbol{a}_{Aero}^{Model}$	Model Computed Aerodynamic Accelerations Vector	m/s^2
$\boldsymbol{x}_{EI}$	Atmospheric Entry Interface State	
h_a^*	Target Apoapsis Altitude	m
h_p^*	Target Periapsis Altitude	m
i^*	Target Inclination	rad
Kn	Knudsen Number	
λ	Particles Mean Free-path	m
L	Vehicles' Mean Chord	m
$\hat{\boldsymbol{n}}$	Normal unitary vector	
ΔA_i	i-th Triangle Area	m^2
ϕ	Visibility Factor	rad
θ	Local Inclination	rad
C_p	Pressure Coefficient	
$\boldsymbol{F_B}$	Body Relative Aerodynamic Force Vector	N
$\boldsymbol{C}_B$	Body Aerodynamic Coefficient Vector	
$\hat{\boldsymbol{V}}_{\boldsymbol{0}}$	Free-stream aerodynamic velocity Vector	m/s
$\boldsymbol{C}_w$	Wind Aerodynamic Coefficients	
$\boldsymbol{C_{XX}}$	Reference Frame Transformation Matrix	
g_r	Radial Component of the gravitational acceleration	m/s^2

g_ϕ	Latitudinal Component of the gravitational acceleration	m$/s^2$
J_2	Zonal Harmonic Term	
$g_{x,y,z}$	Cartesian components of the gravitational acceleration	m$/s^2$
ρ_0	Sea-level atmospheric density	kg$/m^3$
H_s	Atmospheric Scale Height	km
$\dot{Q}_{Rad}$	Radiative Heat Rate	W$/m^2$
t_s	Time Normalization Factor	s
r_s	Length Normalization Factor	m
V_s	Velocity Normalization Factor	m/s
$\boldsymbol{x}_w$	Wind Relative State	
$\boldsymbol{x}_A$	AirSpeed Relative State	
I_{sp}	Propulsion System Specific Impulse	s
g_0	Standard Acceleration Due to Earth's Gravity	m$/s^2$
m_0	Initial Mass	kg
m_p	Propellant Mass	kg
ΔV_{FP}	Fully-Propulsive ΔV	m/s

1 | Introduction

The notion of the aerocapture manoeuvre and the most recent Guidance Navigation and Control (GN&C) state-of-the-art will be covered in this chapter. The present work's research questions will be discussed, and the report's outline will follow.

1.1. State-of-The-Art

1.1.1. Aerocapture Concept and Evolution

Aerocapture falls within the larger set of aeroassist manoeuvres, including aerobraking, aero-gravity and direct entry. These types of manoeuvres require a sufficient atmosphere on the targeted planet for their completion. While direct entry and aerobraking have already been used on missions at Venus and Mars, mainly by exploiting the use of the spacecraft's solar panels [45] [34] [70] [42], aerocapture and aero-gravity have yet to be attempted. The first study related to aeroassist manoeuvre dates from 1962 [40] and investigated the use of aerodynamic forces for plane change in Earth orbit.

The term aerocapture appeared in literature in 1979 by [49], at the conference paper *'The Aerocapture Vehicle Mission Design Concept'*. The suggested mission concept investigated the samples return from Mars by exploitation of the trajectory reported on Figure 1.1. The critical difference between aerocapture and aerobraking, sometimes misunderstood, comes from the fact that aerocapture performs a single atmospheric pass for the orbital energy depletion to jump from a positive to negative energy of the orbit in the Keplerian model, which is exploited for closing the orbit. Instead, aerobraking requires an already closed orbit and focuses on lowering its energy. Thus, the former requires a deeper dive into the planet's atmosphere, while the second performs the manoeuvre over the higher layers. As a result, some implications from a configuration-wise perspective arise since aerocapture will introduce the implementation of TPS and shell-like vehicles to prevent excessive heating, while aerobraking does not. However, the aerobraking shall be equipped with a propulsion subsystem capable of performing the capture manoeuvre. Also, a higher time for arriving at the target orbit is required, making it an operationally intensive manoeuvre.

Later studies kept on developing the concept up till today's well-established aerocapture concept reported on Figure 1.2, and consists of the following stages:

- **Exoatmospheric Approach:** Will affix the initial conditions for the atmospheric pass and will play a major role in aerocapture's feasibility.
- **Atmospheric Pass:** The necessary control actions shall be completed to obtain the desired final orbit.
- **Reorientation:** A slew manoeuvre is needed to point the propulsion system in the direction to perform the periapsis raise.
- **Periapsis Raise:** Performed to increase the orbit periapsis and prevent the re-entry during the next orbital pass.
- **Inclination Correction**: Performed to reduce the wedge (angle formed between the current and target orbit) angle.
- **Apoapsis Correction:** Performed at periapsis to target the orbit apoapsis.

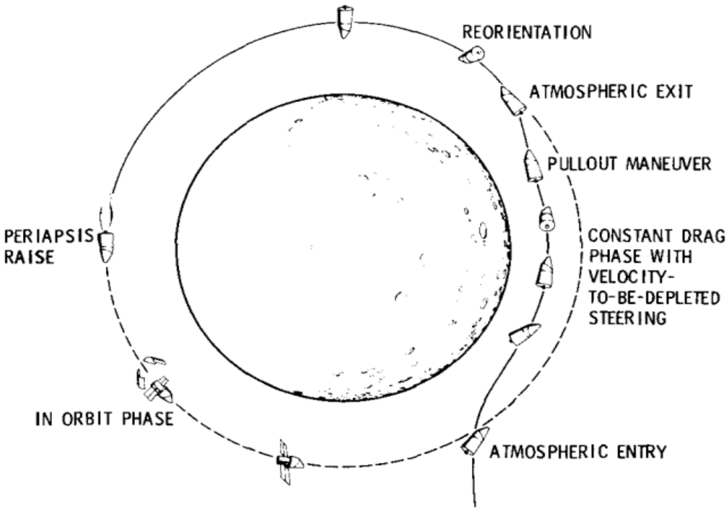
REORIENTATION
ATMOSPHERIC EXIT
PULLOUT MANEUVER
CONSTANT DRAG PHASE WITH VELOCITY-TO-BE-DEPLETED STEERING
PERIAPSIS RAISE
IN ORBIT PHASE
ATMOSPHERIC ENTRY

Figure 1.1: Original Aerocapture Mission Concept [49]

From previously listed stages, apoapsis and inclination correction are introduced because of the trajectory error, mainly provoked by the day-of-flight uncertainty. As a result, the GN&C cannot perfectly target the apoapsis radius and the final inclination, and these propulsive exoatmospheric manoeuvrers are used to reduce errors after the atmospheric pass.

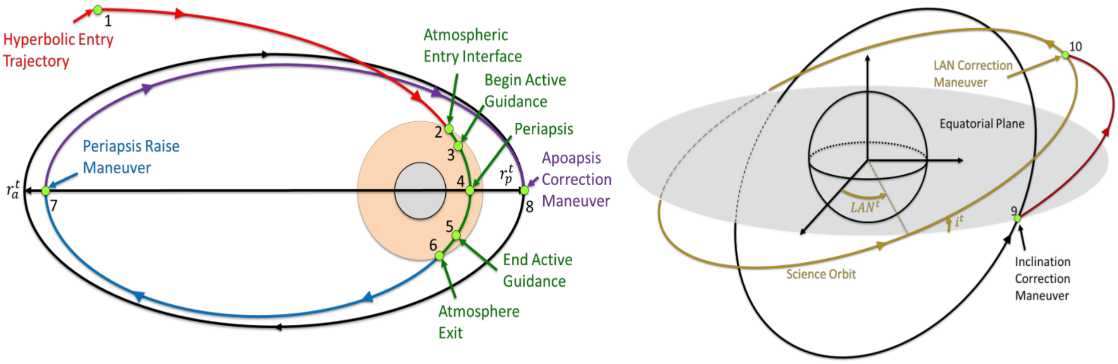
Hyperbolic Entry Trajectory
1
Atmospheric Entry Interface
Begin Active Guidance
Periapsis
Apoapsis Correction Maneuver
Periapsis Raise Maneuver
r_a^t
r_p^t
2
3
4
5
6
7
8
End Active Guidance
Atmosphere Exit
LAN Correction Maneuver
10
Equatorial Plane
LAN^t
i^t
9
Science Orbit
Inclination Correction Maneuver

Figure 1.2: Modern Aerocapture Mission Concept [13]

A different approach is also suggested in the literature. The final apoapsis correction manoeuvre is deleted, as aerobraking is used to obtain the final desired orbit and just the periapsis raise is performed to prevent the spacecraft re-entry. Consequently, the main objective of aerocapture in these mission scenarios would be to achieve a high eccentricity closed orbit around the target planet. It could be advantageous in several mission scenarios, and its adequacy depends on several factors. One of the primary penalties of this approach is related to the time required for the aerobraking manoeuvre to take place, which could elapse for several months. However, when such a manoeuvrability time is allowable, this approach can reduce the propulsive requirements on the spacecraft, which may prove advantageous for example, on some Mars mission scenarios as stated by [20].

1.1.2. Expected Benefits and Risks

Aerocapture was selected for the 2001 Mars Orbiter Mission [80][33]. However, the failures on the Mars Climate Orbiter and Mars Polar Lander missions [73] led to a more conservative approach when dealing with atmospheric flight missions, and the aerocapture manoeuvre was discarded [17]. More recently [38] determined, based on a probabilistic risk assessment comparing propulsive capture, aerobraking and aerocapture, that aerocapture could provide a lower risk when compared to aerobraking, and comparative numerical risk factor to fully propulsive. Further knowledge of the Mars atmosphere from recent missions has helped lower the main risk aerocapture faces, the atmospheric prediction errors [12].

On [84] was concluded that already well-proven technology of blunt-body capsules protected by TPS (Thermal Protective System) allowed Mars aerocapture, providing sufficient control authority for the mission scenario. On [6] it is stated that no demonstration mission was necessary for aerocapture as all the required technologies for the manoeuvre were already well flight-proven and could be implemented for the martian flight.

On the one hand, improving mission scenarios that would otherwise be impractical with current rocket technology is one of the primary advantages that make aerocapture appealing for various mission concepts. Also, it would increase the effectiveness of some mission sets that are now feasible, according to [27]. When compared to fully propulsive, the break-even point for aerocapture will be encountered at the mass and volume budgets for the mission. While aerocapture reduces the propulsion subsystem size, introduces the addition of TPS, and shape constraints affecting the volume utilization factor of the platform since a shell-like vehicle is needed. Some of the primary benefits of aerocapture are described in [71]. Here reported in Table 1.1, where aerocapture cons are also summarized.

Table 1.1: Pros and Cons of aerocapture trajectory

Pros	**Cons**
Potential reduction of initial mass, implying cost reduction of the mission for given mission scenarios	Aeroshell and TPS addition, resulting in a penalty on the volume utilization and mass budget impact to be addressed.
Potential decrement in travel time. Higher V_∞ is possible at capture for equal mass and equal target orbit.	Risk addition, as it is an untested manoeuvre with no historical precedent, will result in higher development costs and greater risk for the initially created missions.
Potential increase in payload mass ratio for certain mission scenarios.	Associated manoeuvres sensitivity to planet's atmospheric uncertainty (Earth included), therefore, the manoeuvre robustness is not ensured.

1.1.3. Small Satellites at Mars

Recent scientific interest in the planet Mars has highly increased the future number of planned missions to the red planet. Consequently, the number of ride-share opportunities for missions which fit inside the secondary payload constraints intended as small satellite-class to Mars could be positively affected. Most recent scientific missions target polar or high inclination orbits due to their scientific purposes, as reported on [22]. Allowing an independent capture technology for small satellite-class would provide a reduced-cost platform to target different scientific investigations, which may require different target orbits to the one given by the rider mission. Performing such highly demanding orbital manoeuvre may be unfeasible because of the current propulsive technology limitations. Because of chemical propulsion's bad performance to volume relation, preventing its use on smallsats for capture manoeuvre due to small satellite's tight volumetric constraints. Aerocapture could enable higher flexibility to the ride-share missions, extending the range of available target orbits and reducing the influence on the mission provided the rider's mission objective.

Some other strategies, such as performing a propellant cheaper propulsive capture into a very eccentric orbit for later use of aerobraking manoeuvrer, will still lead to excessively expensive volume and mass manoeuvre and operationally intensive for small satellite class missions [22]. Therefore, aerocapture poses as an alternative to enable such a mission-kind manoeuvre, allowing lower-cost, higher-risk and quicker scientific and commercial return missions to the Mars system, fitting the shape and mass constraints imposed by ESPA rings used for secondary payloads. Some of the missions that could take benefit from such a technology are reported to mention [22][5]:

1. Missions to target Mars's moons.
2. Missions to study Mars's upper atmosphere.
3. Global Mars coverage constellations for communications.
4. Global Mars coverage constellations for observation.
5. Mars-Earth communication relays on geostationary orbits.
6. Constellation for remote sensing for weather observations.
7. Global Navigation Satellite System (GNSS) Constellation.

Moreover, such technology will potentially accelerate the Mars understanding and colonisation, providing quicker, cheaper and easier access to the planet's state information.

1.1.4. GN&C

As previously briefly introduced in subsection 1.1.2, the GN&C will be one of the main actors to deal with most of aerocapture's risks, together with thermal protection and structural materials. Consequently, most work has been centred on this aspect over the last decades.

In a nutshell, aerocapture requirements can be synthesised as arriving at a specific spot of the atmospheric interface with a predetermined state. At the entry point of the atmospheric interface, the initial conditions are provided, together with state, atmospheric, and aerodynamic uncertainty. The guidance shall withstand them and provide an effective manoeuvre. In the present section, some of the introduced ideas will be depicted, and the key technologies to address the aerocapture's risk will be introduced. Some of the primary guidance schemes will be commented on, and their advantages and disadvantages will be explained.

Aerocapture Type According to Used Control Variables

Actuators are needed to achieve the desired control of the spacecraft. Actuators have their own dynamics and error, accumulating into the real state vector and history in time. According to the different existent variables to manipulate the aerocapture trajectory, three main control strategies for aerocapture can be differentiated: Bank Angle Modulation, Drag Modulation and Direct Force Control [12].

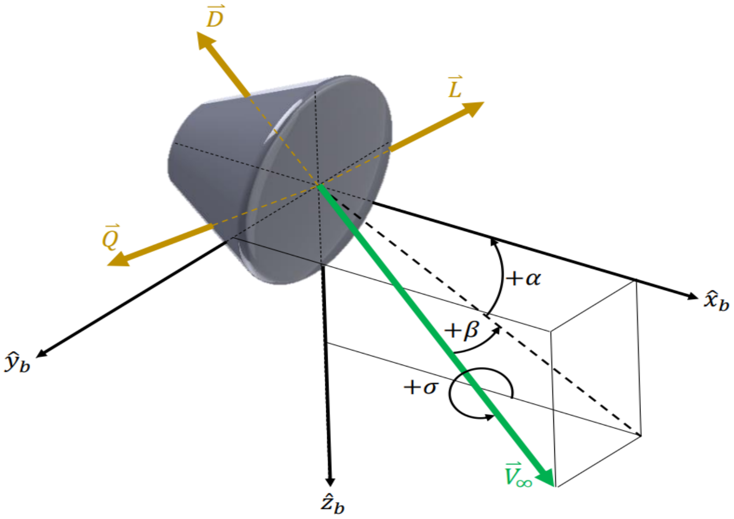

Figure 1.3: Control Variables in Aerocapture [12]

Bank-Angle Modulation The Bank Angle Modulation (BAM) is the most commonly studied control method for aerocapture in literature [17]. It consists of rotating the Lift vector around the free-stream velocity vector. By convention, positive angles are measured clockwise, leading to 0 degrees corresponding to full lift-up attitude and 180 degrees to full lift-down, as reported in Figure 1.3. With constant trimming of the angle of attack, and of the side-slip angle.

Lateral (orbital out of the plane, crossrange) and longitudinal (orbital in-plane, downrange) channel controls are coupled on a single control variable, the bank angle, where the downrange and crossrange concepts are depicted in Figure 1.4 for an Entry Descent

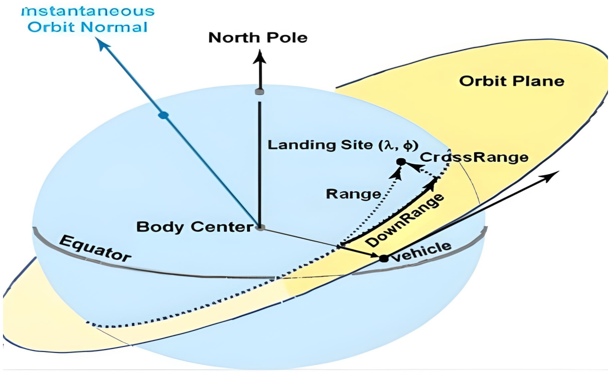

Figure 1.4: DownRange and CrossRange Representation on a Entry, Descent and Landing Trajectory [74]

and Landing (EDL). The longitudinal channel is controlled by the magnitude of the angle, while the sign of the bank angle affects the lateral one. As a result, different guidance schemes throughout the literature have relied on separate logics, differentiating the one in charge of performing the bank-angle reversals for the lateral control which is based upon a simple error dead-band scheme and the logic controlling the bank angle's magnitude for the longitudinal channel [69].

Some portions of Apollo's entry guidance were based on the control over the bank angle [14]. Also, more recently, Mars Science Laboratory (MSL) utilised it for compensation for the trajectory dispersions produced during the atmospheric entry [79]. Consequently, Mars 2020 mission utilised it, using an MSL-derived bank angle modulation strategy for its entry guidance.

This control strategy is intended for lifting bodies, requiring L/D sufficient shapes for its realisation, which is provided by the vehicle's aerodynamics. Usually, for commanding the aerodynamic angles, Reaction Control System (RCS) is used for the attitude control of the spacecraft and will take charge of constantly trimming the angle of attack and actuating the bank angle.

Drag Modulation This method has been mainly developed in the last decade. Consist of modifying the ballistic coefficient by changing the vehicle's aerodynamic reference surface. The change in the reference surface impacts the ballistic coefficient reported on Equation 1.1. The leading figure of merit affecting the Drag Modulation (DM) corridor width (further explanation on the corridor figure is found on subsection 3.4.1) is the ballistic coefficient ratio formed between the maximum reference surface configuration and the minor one. High ratios could be obtained using NASA's Hypersonic Inflatable Devices (HIADS) [31] or Adaptable Deployable Entry and Placement Technology (ADEPTS)

[76][68]. Also, in Europe, some similar devices are being developed, IRENE is an Italian Space Agency (ASI) development, and its Mars aerocapture feasibility is studied on [32]. It consists of an umbrella-like device reported in Figure 1.5.

$$C_B = \frac{m}{C_D S_{Ref}} \tag{1.1}$$

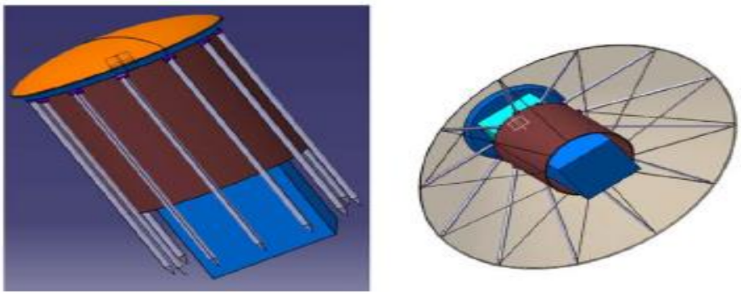

Figure 1.5: DHS Mission with IRENE drag sail [32]

By increasing the vehicle's drag by means of reference surface augmentation, the orbital energy depletion rate increases too, and it can be used as a control variable to manage the aerocapture's longitudinal channel. As no lift is used, this manoeuvre is intended for ballistic bodies with zero lift. It is often applied on symmetrical blunt body shapes with spin stabilisation to nullify the angle of attack.

Consequently, the out-of-plane, referred to as lateral channel, cannot be controlled. Despite this limitation, DM is a popular option for Mars' aerocapture due to its simplicity. Two main classes of DM techniques exist Staged Jettison and Continuously Variable.

In the jettison strategy, control events are based on the jettisoning of the drag skirt, leading to a discretised increase in the ballistic coefficient. Hence, this can be a single or multi-jettison strategy. The main drawback of this approach comes from the control saturation vulnerability. As the atmosphere behaves stochastically, the dispersions encountered after the control event cannot be counteracted. With the increase in the number of stages, this problem is reduced, as it will approach more to a continuous control. Single event jettison has been studied for Mars aerocapture [59], for big and small satellites missions [23][81]. It is the main current path study for small satellites' aerocapture. [62] Addressed the performance improvement of multi-staging as it results in mitigation over the control saturation.

Direct Force Control Direct Force Control (DFC) [48] method arose to address some of the inconveniences the previous aerocapture techniques presented on specific case scenarios. This method has the advantage of controlling both the longitudinal channel, which takes charge of meeting the apoapsis target of the exoatmospheric orbit, and the uncoupled lateral channel control-ability, responsible for controlling the out-of-plane component of the final orbit. To do so two different control variables are used. The angle of attack controls the longitudinal channel, while the side-slip angle controls the lateral one, these angles can be found in Figure 1.3.

Performance improvements were already encountered in EDL problems when angle of attack is introduced in the control. Then, further improvement in those results was observed when the direct force control was introduced on the Mars landing problem [18], where higher precisions on the landing spot target were obtained.

Another noteworthy characteristic of the direct force control is the non-saturated control authority throughout the atmospheric pass. This provides a higher robustness against day-of-flight uncertainty, leading to smaller exoatmospheric impulsive corrections, which would imply a size reduction over the propulsive subsystem.

The decoupling of the dynamics to target the longitudinal and lateral channels separately is performed by trimming the bank angle to zero degrees and discarding second-order dependencies in the aerodynamic forces. It is accomplished by using a small enough angle of attack and side-slip, the values of these angles will be dependent on the capsule's aerodynamic properties [18].

To the authors' knowledge, no attempt for this kind of control has yet been studied in Mars aerocapture for small satellite aeroshell class missions. Hence, the feasibility of such a manoeuvrer shall be addressed. If feasibility is verified, the Optimal Control problem shall be conducted on an open loop, searching to minimise the two main figures of merit that represent the manoeuvrer's cost: the exoatmospheric ΔV and the total heat during the atmospheric pass. For a final implementation of an optimality-based online guidance scheme, where the optimal solution is applied.

Navigation

Navigation determines the spacecraft's state. Depending on the mission phase of aerocapture, it may be differentiated into two subsections: approach navigation and in-flight navigation.

The approach navigation deals with the trajectory estimation previous to the atmospheric entry of the vehicle once inside the planet's sphere of influence. The combination of the orbit determination errors and the manoeuvre's execution error drive the delivery errors at the entry interface [12]. During this phase, the state reconstruction is performed through standard radiometric tracking from Deep Space Network (DSN), and it can be augmented employing Optical Navigation (OpNav), as done in the *Voyager 2* mission [17]. The optical augmentation allows the improvement of the angular position of the spacecraft with respect to the planetary body. The hybridisation of the measurements significantly reduces the state uncertainty, being the targeted planet's ephemeris the dominant source of error[17]. Autonomous Optical Navigation (AutoNav) could further improve the navigation capabilities since the data accuracy increases linearly with the decreasing distance, and information from minutes prior to the atmospheric entry could be used autonomously on the spacecraft [7].

The estimation precision at the atmospheric interface entry (approach navigation) is of paramount importance for the aerocapture's feasibility, as later will be assessed on chapter 3 and chapter 4, when dealing with trajectory feasibility and performance. The uncertainty, mainly on the flight path angle, shall stay within the corridor (the corridor concept is explained in subsection 3.4.1). Hence, the spacecraft has sufficient control authority to mitigate this effect and will be one of the main concerns determining the aerocapture's mission feasibility given a specific mission scenario.

The in-flight navigation takes charge of performing the trajectory reconstruction during the atmospheric pass of aerocapture. It shall be performed with onboard taken measurements and are responsible for closing the feedback loop to account for day-of-flight uncertainty. During the aerocapture's atmospheric phase, the navigation shall be autonomous due to two main factors: the short time it takes the manoeuvre to be performed (on the order of some hundreds of seconds), the existent delays on the communications from Earth, and the ionisation encountered by the high temperatures produced during the hypersonic flight regime, which prevent the communications to happen. As a result, translation accelerations and gyroscopic measurements from an Inertial Measurement Unit (IMU) will produce the primary data for the state estimation filtering. Also, some Flush Air Data Systems (FADS) measurements could be recovered and compared to a model to produce state estimate updates [36].

The onboard sensor's measurement error, the state error at the atmospheric interface given by the approach navigation and the filtering limited capabilities drive the in-flight navigation error. The guidance shall account for the drift produced over the state estimation, a consequence of the error integration along the aerocapture trajectory. Some recent efforts have been made by [61] to improve the navigation filters applied to aerocapture due to the saturation that drag modulation presents. However, this study makes many simplifications, and the developed filters are based on following the atmospheric model.

As a result, the conclusion is stated that further investigation shall be performed.

Guidance

Two main broad categories of guidance schemes for aerocapture can be found in the literature: implicit and explicit guidance. The former is based on following a pre-planned reference trajectory. Here the Terminal Point Controller will be introduced. In contrast, the second one is based on recomputing onboard a near-optimal path from the present state to the target state without the use of pre-planned off-line computed trajectories. Inside the branch of Explicit Guidance algorithms, two subcategories can be distinguished: Predictor Correctors and Energy Controllers. Some other more disruptive approaches have been attempted too and will be presented later in the subsection.

During the last decade, the aerocapture guidance research trend has varied. Previously, guidance schemes were mainly focused on targeting the radius of apoapsis. Since [39] demonstrated, under some analytical assumptions, that was different, minimising the ΔV and targeting the apoapsis for specific mission scenarios, and introduced a ΔV optimal mode on NASA's Fully Numerical Predictor-corrector Aerocapture Guidance (FNPAG) software. Then [44], solved the optimal control problem for the bank angle modulation and minimum ΔV trajectory, introduced the obtained Bang-Bang control structure into the guidance scheme, and reported comparably better results than all previous existing guidance modes.

Terminal Point Controller Most aerocapture guidance schemes to date are based on BAM techniques. For implicit guidance, a Terminal Point Controller was developed on [60] and evaluated on a French Space Agency (CNES) and NASA joint study [65]. It was found to be the most robust guidance algorithm, but with a poor performance in the presence of Dust Storms at Mars. Few works within this respect are found currently, mainly due to the missions specificness of the algorithm, as the trajectory shall be specially designed for each mission, which ends up leading to a lack of adaptability.

Energy Controller Inside the explicit guidance branch, control over the spacecraft's energy is performed, where the target apogee determines the final orbital energy. By altering the energy gain, which is computed through the ratio of a function of the drag, called the energy rate, and the energy error. The idea behind this guidance scheme is to zero both the energy error and the energy rate. The altitude rate is obtained from the energy gain, and a vertical acceleration analytical equation is used for the bank angle computation.

This concept was developed in the 1980s [24], and during 2001 on the CNES and NASA study [65] [64], this energy controller guidance type was compared against other algorithms and resulted in being a good compromise between robustness and accuracy. However, recent developments have yet to be found on aerocapture guidances that exploit this concept, and the current trend is the development of rather simpler or optimality-based aerocapture schemes.

Predictor-Corrector Two main subcategories can be distinguished inside the predictor-corrector: Analytical Predictor-Corrector (APC) and Numerical Predictor-Corrector (NPC). The radical difference between these two comes from the way of propagating the atmospheric trajectory. While APC introduces simplifications into the equations of motion in order to achieve analytically integrable equations, the NPC, on the other side, makes use of numerical integrators of the full dynamics on the predictor side to obtain the propagation throughout the atmospheric pass.

APC In 1985 [8] introduced a control algorithm for bank angle based on two phase control for the longitudinal channel, consisting of the equilibrium glide and exit phases. The equilibrium glide phase attempts to zero the altitude acceleration by introducing this condition into the vertical dynamic equations, from which the equilibrium bank angle for this phase is obtained. Then, the control equation is computed by introducing a damping term on the altitude rate, and a proportional term on the dynamic pressure part. During the exit phase, a predictor-corrector strategy was used through the integration of a constant bank angle till the exit condition, performed by the exploitation of an exponential atmosphere and a constant altitude rate to target the exoatmospheric apoapsis.

Later, some improvements to the previous scheme were introduced during the early 2000s. The NASA-CNES collaboration campaign worked on the improvement of APC algorithms [47] for its implementation on the Mars Sample Return Orbiter. Later the aerocapture utilisation for this mission was dropped. Two main changes were introduced: on the equilibrium glide phase, the dynamic pressure proportional term was replaced by a term related to the drag acceleration, and on the exit phase, an easier method to compute the constant altitude rate to target the apoapsis was implemented. Afterwards, some further improvements were developed by [28] when computing the transition velocity condition and the inclusion of a new equivalent density height to improve the robustness of previous results.

Since the works of [39] and [44], most of the focus was set on optimality-based aerocapture guidance. The APC version of this algorithm [10] tries to mimic the bang-bang control structure obtained from optimal control problem resolution on bank angle control. It achieves so by exploiting the Fourier series and an exponential function to parametrise the aerodynamic acceleration effects and the flight path angle. This results in an equation to predict the atmospheric exit velocity and a possible ascent path by iterating over the exit flight path angle. The parametrisation used is mission dependent, and each mission would require a good amount of tuning for its implementation.

Some APC developments are also encountered for drag modulation control method [55] [56][11]. Where the optimal control problem is addressed for drag-modulated aerocapture by [29]. The optimal control strategy followed a bang-bang control structure, analogously to what occurred on bank angle modulation.

NPC In the early 1990s, [58] introduced a 6 DOF numerical predictor-corrector scheme. The main idea behind this algorithm was to develop an adaptable algorithm for a range of vehicles with minimal modifications and get closer to the theoretical performance limits, exploiting the enhanced available computational power onboard. By numerically integrating with constant bank angle magnitude, a load relief logic was introduced in case of predicted g-load exceeding the mission's design limits. Once the maximum deceleration point is passed, the vehicle rolls to the bank angle required to produce the proper atmospheric exit conditions.

Over this concept, NASA developed *'PredGuid'* software based in Fortran, which has been very popularly used on the Aerocapture mission designs, where different modes were implemented. Later [39] developed *PredGuid+A*, where a *Golden Search* ΔV minimisation mode was implemented. It was discovered that certain cases exist where apoapsis targeting is not correlated with ΔV minimisation. The guidance will improve the targeting of the apoapsis at the expense of an increase in the exoatmospheric propulsive cost. According to the analytically developed inequality assuming constant bank angle, it demonstrated highly improved performance where apoapsis targeting and ΔV were not equivalent.

Related to optimality, [67] studied the minimisation of the total convective heat, where introduced the idea that the effectiveness of the aerocapture manoeuvre depends on the ratio between the fuel mass reduction and the weight of the TPS. Bang-bang control was identified to heat load minimising, on bank angle modulation, from full lift-up to full lift-down. It also suggests the possibility of multiple deep entries instead of just one single pass to lower the orbital parameters and the heat shield requirements accordingly. Exploiting the required thermal protection needed for the aerocapture manoeuvre, the later aerobrake could be more profound than usual as the size of the already existing thermal protection would allow so, reaching the target earlier.

Later, [44] demonstrated by the use of optimal control theory that as a general property, aerocapture will have a bang-bang bank angle magnitude profile for post atmospheric ΔV minimisation. This leads to 40% improved results compared to the ΔV optimal model developed on *PredGuid+A* algorithm. Since the latter limits the solution to a functional space to which the optimal solution does not belong. During the descent phase, full lift-up will have the highest endo-atmospheric periapsis altitude, which helps reduce the velocity loss. During the ascent phase, full lift-down helps produce the smallest FPA exit.

The minimisation of radiative thermal load [86] proved on bank angle modulation that the optimal control structure coincides with the one of ΔV, and added the concept of attitude kinematic constraints to the guidance scheme, giving a more realistic behaviour to the algorithm. The algorithm uses a bang-bang structure, but its objective function is apoapsis radius targeting. The guidance scheme developed is called OAK.

All previously commented algorithms are developed for the bank-angle modulation, proving its popularity during the last decades when studying aerocapture trajectory. Different NPC algorithms have been developed for other control methods. For drag modulation, [59][62] developed numerical schemes, and [23] studied its applicability to SmallSats at Mars and compared to heuristic velocity trigger, proving NPC to have a more robust performance and a ΔV improvement of up to 115 m/s.

For the direct force control, [48] presented the development of an NPC algorithm applied to aerocapture, containing different control methods, reporting better results when bang-bang type control was employed. Later [25] obtained the ΔV optimal control strategy based on a numerical basis for a particular vehicle and mission scenario at Mars. Results proved to follow and almost near bang-bang control structure. This method has also been used on [13] for Neptune aerocapture with an MSL-kind vehicle using an NPC algorithm.

Different Approaches Different guidance strategies from the already commented ones have been developed for aerocapture trajectory. Based on ADEPTS NASA's vehicle concept, a tree-based approach [9] and convex programming [85] algorithms have been developed. On these algorithms, an hybrid control strategy combining bank angle modulation and angle of attack was exploited. These methods present an albeit of optimality, but no proof is given that guarantees that the sequential minimisation problem leads to global trajectory optimisation. However, they prove to have robust behaviour against uncertainties, and they provide more predictable results when compared to NPCs.

The stochastic Optimisation algorithm is implemented for bank angle modulation through two-stage optimisation [87], where a first decision is made previous to the random variable

Table 1.2: Aerocapture Guidance Schemes pros and cons summary

Guidance Scheme	**Pros**	**Cons**
Terminal Point Controller	Robustness	Performance during Dust Storms, Lack of Adaptability (mission speciousness)
Energy Controller	Robustness, Accuracy	Complexity, Non Optimality-based
APC	Computationally Efficient, Robustness	Lack of Adaptability, Complex, Performance
NPC	High Adaptability, Modularity, Performance, Robustness, Global Optimality	Higher Computational Burden
Tree Based & Convex Programming	Robustness, Predictable Outcomes	Not global optimality guarantee
Stochastic Optimization	Performance, Optimality-based, Robustness	Highest Computational Burden

realisation, considered to be atmospheric density, and then a second decision is made as a deterministic optimisation problem. Some simplifications are introduced when considering that the density is a function of a single random variable and that the perturbation derivation happening along the whole trajectory is revealed as soon as the first decision is made. The results outperform the NPC presented on [86] in terms of ΔV minimisation at the cost of a much higher computational cost. Even if computational parallelisation is considered, it will lead to a four times higher computational burden when compared with the NPC.

Summary The commented advantages and disadvantages of the different guidance schemes have been reported on Table 1.2.

1.2. Research Questions

SmallSat aerocapture has been mainly studied in literature by means of Drag Modulated Aerocapture and the use of drag increment devices such as drag skirts. The promising advantages that direct force control can provide, and the higher technological readiness level of aeroshell capsule-like vehicles make its study applied to small satellites appealing. Since higher thermal and structural load constraints can be faced, aerocapture manoeuvre could be enabled.

This study will assess two main topics:

- The feasibility of the manoeuvre using the direct force control with an aeroshell capsule respecting Smallsat form factor constraints.
- The development of an optimality-based aerocapture guidance scheme.

A numerical simulation environment is developed, and used to address the guidance method feasibility and enable the guidance algorithm development. Mathematical analysis has been employed to obtain the optimal control strategy.

The performed study attempts to answer the following research questions:

- **Q1:** Is using the direct force control on a small-satellite class mission with an aeroshell capsule-like vehicle feasible for Mars aerocapture?
- **Q2:** Does the guidance present enough robustness against expected trajectory uncertainties?
- **Q3:** Does this approach provide any advantage compared to existing SmallSat aerocapture concepts?

1.3. Thesis Outline

In chapter 2, models used for the developed numerical software is presented, and its verification is addressed.

In chapter 3, a parametric study dealing with different capsule designs and entry conditions is made, accounting for the shape, volume and mass constraints faced on small satellite class missions. The aerocapture corridor concept and the employed numerical models are introduced. A final test mission is selected for the later guidance algorithm testing, where the trajectory and vehicle operational constraints are introduced to obtain the trajectory's feasible region.

In chapter 4, the Optimal Control strategy is developed for the selected mission, and the online Guidance Design is performed. Here the NPC selection for the guidance controller is argued. The algorithm performance is verified, and sensitivity and robustness analyses are performed. Final sizing comparison with fully-propulsive capture is reported.

Finally, in chapter 5 conclusions concerning the overall research will be drawn. Providing the obtained research question answers, limitations of the study and suggested future works.

2 | Modelling

During this chapter, the mathematical models used in the thesis are presented. These are of paramount importance and will influence the validity of the work. Introduced simplification and trade-offs will be discussed, and their implications will be assessed. Aerodynamics, trajectory dynamics, atmospheric and propagators will be discussed. Finally, information about the real system modelling will be depicted.

2.1. Aerodynamics

2.1.1. Low-Density Flow

A spacecraft coming from space will phase the whole range of low-density effects [3]. For higher altitudes, molecular flow is present. As altitude is reduced, the mean free path of the atmospheric particles decreases, and the transition regime appears, also known as *'rarified flow'*, where velocity and temperature slip conditions happen. Finally, if the altitude is further decreased, the continuum model applies, where *Euler equations* are derived from applying the boundary conditions to the *Navier Stokes equations*.

The similarity parameter that identifies these regimes is the *Knudsen Number*. It is defined as the ratio between the particle's mean free path over the mean length of the vehicle, $Kn = \lambda/L$. Continuum assumption can be performed for Kn<0.2.; slip effects are accounted for 0.3<Kn<1.0 denominated as transition regime, and for higher Kn, free molecular flow is present [3].

Considering the mean free-path for the Martian atmosphere [57], and from Table 3.1 L=0.96[m] for the medium chord of a small-satellite class, the Knudsen number has been computed Figure 2.1. Some conclusions can be extracted from the obtained results for the aerocapture case on Mars. A continuum flow assumption can be made up to 95 [km] of altitude. The transition and molecular flow regimes will be encountered from 95 [km] up to 140 [km].

On aerocapture, very high velocities will be encountered, and the core of the trajectory will

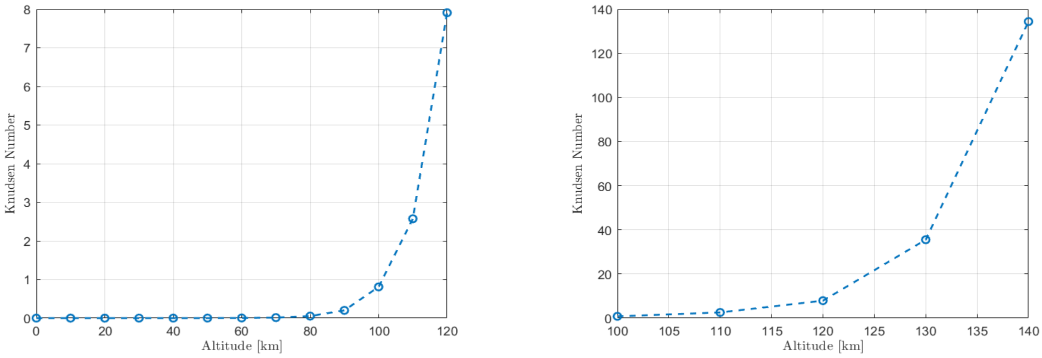

(a) Kn for 0 to 100 km Altitude.

(b) Kn for 100 to 130 km Altitude.

Figure 2.1: Knudsen Number Evolution at Mars for SmallSats

happen at altitudes lower than 95 [km]. Some rough conservative numbers can be taken, considering an entry flight-path angle at the entry interface equal to -12 degrees. Assuming a 6 [km/s] velocity, the vertical component found will be 1.25 [km/s]. Assuming, due to the low presence of particles in the high region of the atmosphere, that the spacecraft velocity is constant from 130 to 95 [km], the vehicle will take 28 seconds to pass through that region. The same will happen for the ascending leg of the trajectory. When assuming a 4 km/s velocity, around 40 seconds will be required to pass over the region. Therefore, a total time of 68 seconds from an average 800 seconds trajectory will represent 9% total trajectory time. Remember, the effect provoked by these transition regions will be small and not uniform, being stronger in the 95-100 km range and smaller for higher altitudes.

Consequently, the assumption of continuum aerodynamics for the aerocapture trajectory is a good approximation. Transition and molecular flow regimes can be assumed as a perturbation, where even the assumption of continuum mechanics cannot be exploited for the aerocapture control as it will lack control authority due to the negligible density encountered and hence, lack of dynamic pressure. The online guidance will not require these considerations and could be implemented on a high-fidelity real system model or even account for their effect in a perturbation way. It can also be stated that these effects could be captured by the IMU measurements and fed into the online model by the Navigation Filter subsection 4.2.6 even with continuum aerodynamic modelling assumption.

2.1.2. Modelling

The aerodynamic study has been performed with an ad hoc developed application based on local inclination surface methods. This application is based on [63], where *Standard Triangulation Language (STL)* file formats are exploited for geometry discretisation. The main advantage of this method comes from the fact that design can be performed in a 3D modelling program, such as *SolidWorks*, and then exported in STL. The body is discretised into various triangles, with a list of vertices and elements given by a connectivity list.

Matlab has been used to develop the aerodynamic calculator. It provides some already built-in functions that ease the implementation, such as reading the STL file and reporting the list of points and elements.

Firstly, the reference surface shall be computed for the force normalisation. To do so, the triangle normal vector can be computed by constructing two plane vectors within each triangle and performing the cross product, which would retrieve a normal vector to the surface Equation 2.1. Then, the vector is divided by its norm to make it unitary, as reported on Equation 2.2.

$$\boldsymbol{N} = (\boldsymbol{x}_2 - \boldsymbol{x}_1) \wedge (\boldsymbol{x}_3 - \boldsymbol{x}_1) \tag{2.1}$$

$$\hat{\boldsymbol{n}} = \frac{\boldsymbol{N}}{||\boldsymbol{N}||} \tag{2.2}$$

To compute the area of each triangle composing the surface of the 3D model Equation 2.3, the connectivity list of the triangles is used to get the linked point on each triangle.

$$\Delta A_i = \frac{1}{2} ||((\boldsymbol{x}_2 - \boldsymbol{x}_1) \wedge (\boldsymbol{x}_3 - \boldsymbol{x}_1))|| \tag{2.3}$$

In the current work, the reference surface for the spacecraft capsules will be defined as the hypersonic wet surface when set at zero angle of attack and side-slip. Hence, the velocity vector for the computation of the reference surface is defined as $\hat{\boldsymbol{V}}_0 = [1, 0, 0]^T$. The triangles found on the hypersonic aerodynamic light are found by direct application of Equation 2.4, from which by using Equation 2.5, the flow deflection angle is obtained. If the deflection angle is positive, it means the triangle is set on aerodynamic light, and Equation 2.6 is used to account for its contribution, being j the number of triangles found.

$$\phi = arccos\left(\hat{\boldsymbol{V}}_0 \cdot \hat{\boldsymbol{n}}\right) \tag{2.4}$$

$$\theta = \frac{\pi}{2} - \phi \tag{2.5}$$

$$S_{Ref} = \sum_{1}^{j} \Delta A_i \tag{2.6}$$

For the computation of the aerodynamic coefficients, Equation 2.4 and Equation 2.5 are again used. If the triangle is found to be on aerodynamic light, this will contribute to the force; otherwise, it does not. The Newtonian method is employed to compute the pressure coefficient Equation 2.7. The total force by momentum exchange on that triangle is given by Equation 2.8. Finally, to get the coefficient on the body axis, Equation 2.9 is employed.

$$C_p^j = 2\sin^2(\theta_j) \tag{2.7}$$

$$\boldsymbol{F}_B = \sum^{j} C_P^j \hat{\boldsymbol{n}}_j A_j \tag{2.8}$$

$$\boldsymbol{C}_B = \frac{\boldsymbol{F}_B}{S_{Ref}} \tag{2.9}$$

The incoming velocity vector is varied following the Equation 2.10 to obtain the coefficients for different angles of attack and side-slip angles.

$$\hat{\boldsymbol{V}}_{\boldsymbol{0}} = [\cos\alpha\cos\beta, \sin\beta, \sin\alpha\cos\beta]^T \tag{2.10}$$

Finally, the body coefficients are projected into the wind frame to obtain the final aerodynamic coefficients through Equation 2.11, where $\boldsymbol{C}_{WB}$ is reported in Appendix A.

$$\boldsymbol{c}_W = \boldsymbol{C}_{WB} \cdot \boldsymbol{c}_B \tag{2.11}$$

2.1.3. Code Validation

The correctness of the code shall be addressed. For this purpose, a cylinder shape body will be used, and the obtained result will be compared to an analytically computed value. The cylinder geometry is reported on Figure 2.2, consisting of 248 vertices and 492 elements. The analytical results are obtained from [3], and comparison results are reported in Table 2.1. Even if not a very high-resolution discretization is used, good compromise results are obtained within a 0.1% error compared to analytical results. Hence, the software can be considered validated.

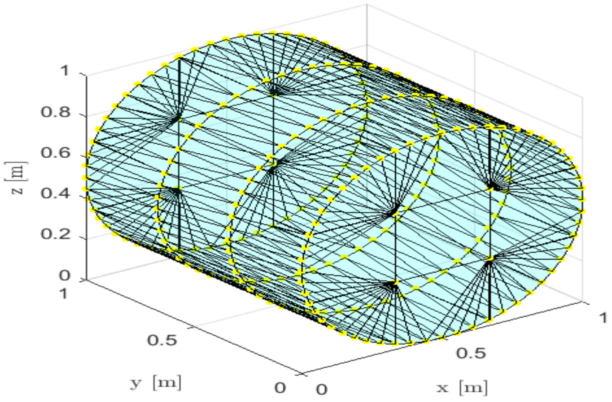

Figure 2.2: Cylinder

Table 2.1: Aerodynamics Code Validation Results

Property	Computed	Analytical	Percent Error
S_{Ref} $[m^2]$	4.7074	4.7124	0.1051%
Force Coefficient	-1.3326	-4/3	0.05%

2.1.4. Convergence Analysis

This aerodynamic computational method is based on the local discretisation technique and will require a convergence analysis of the results. The discretisation shall be selected for computational reasons, performing a trade-off between the accuracy and the associated computational burden.

The analysis has been conducted by the computation of the aerodynamic coefficients varying the angle of attack and trimming to zero the bank angle for a medium and a high fidelity discretisation of ESPA-compatible a=1.5 capsule Figure 2.3. The medium fidelity capsule is obtained from default parameters provided by *SolidWorks*, in this case consisting of 1697 vertices and 3390 elements. For the high-fidelity model, the higher allowed resolution is set at the time of geometry exportation, resulting in 51840 vertices and 103680 elements. This high-fidelity model is computationally expensive and will be used to analyse the convergence of the aerodynamic results provided by the default discretisation settings, which allows milder computational requirements.

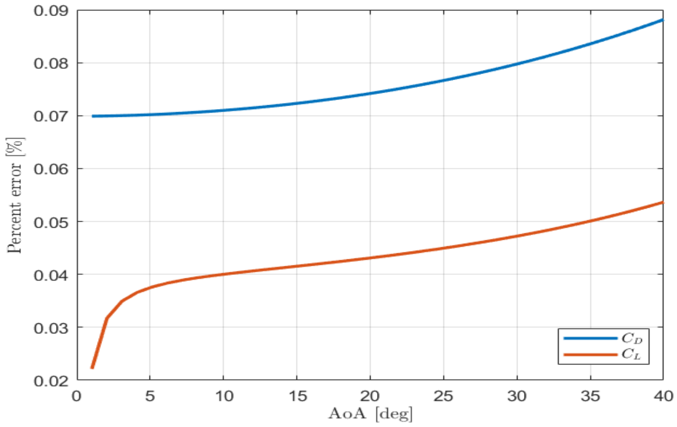

Figure 2.4: Percent Error from Convergence Analysis

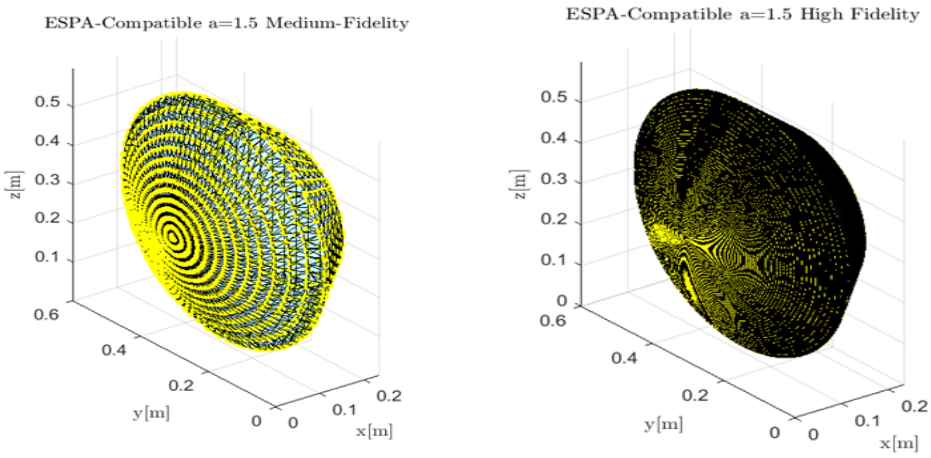
ESPA-Compatible a=1.5 Medium-Fidelity
ESPA-Compatible a=1.5 High Fidelity
z[m]
y[m]
x[m]
0.5
0.4
0.3
0.2
0.1
0
0.6
0.4
0.2
0
0.1
0.2

(a) Medium Fidelity Body. (b) Very High Fidelity Body.

Figure 2.3: Considered Discretizations for Convergence Analysis

The percent error between both discretisations is reported on Figure 2.4. Therefore, it can be concluded that the medium fidelity model reports good convergence within 0.1% error compared to the high fidelity model, providing a good compromise between accuracy and computational burden for the aerodynamic study.

2.1.5. 1-D Aerodynamic Coefficients

DFC is based on the decoupling of longitudinal and lateral channels. To do so, the lift and drag coefficient on the online model will only depend on the angle of attack, while the lateral coefficient is on the side-slip. The 1-D aerodynamic coefficients are reported on Figure 3.5.

Since for the guidance testing ESPA compatible capsule with hyperbolic parameter equal to 1.5 is employed, its aerodynamic coefficients have been used to perform a polynomial regression for the aerodynamic modelling, as polynomial functions present computational advantages. From the maximum aerodynamics angle used during the manoeuvre, given on Table 3.3, the aerodynamic linear region will be encountered for the lift and lateral coefficient. On the contrary, the drag coefficient is not linearly behaved. Establishing an $R^2 \geq 0.99$ condition, drag is well represented by a second-order polynomial. The obtained results are given in Figure 2.5.

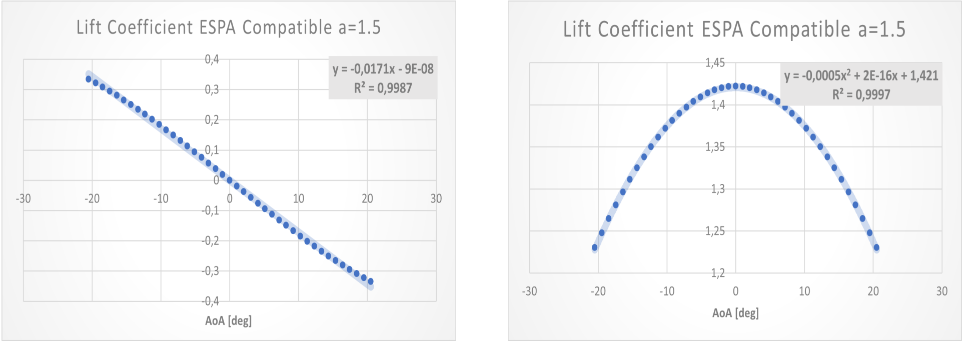

(a) Lift Coefficient Linear Regression (b) Drag Coefficient Polynomial Regression

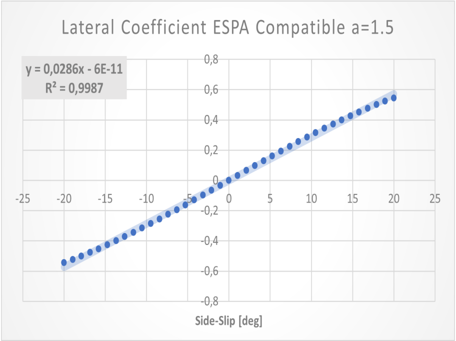

(c) Lateral Coefficient Linear Regression

Figure 2.5: Regression Aerodynamic Model ESPA-Compatible a=1.5 capsule

2.2. Equations of Motion

Different sets of equations of motion do exist to represent the motion of a flying object across the atmosphere. Among these sets, Rotational Spherical dynamics provide an intuitive interpretation of the vehicle's state and fast computational capabilities. Consequently, they have been the preferred set of equations used in aerocapture studies. Other more straightforward dynamics, such as the Inertial Cartesian equation, will also be presented and used for the spherical equations verification. This thesis employed reference system definitions and Euler angles are reported in Appendix A.

2.2.1. Relative Spherical

The rotational equations of motion are represented on the rotational planet's fixed frame. The complete set of equations of motion can be found on [51] and are here reported from Equation 2.12 to Equation 2.17. This set of equations presents two singularities due to the Euler angles reference transformation performed on its development and are found on $\gamma = \pm\frac{\pi}{2}$, and $\phi = \pm\frac{\pi}{2}$.

$$\dot{r} = V\sin\gamma \tag{2.12}$$

$$\dot{\theta} = \frac{V\cos\gamma\cos\psi}{r\cos\phi} \tag{2.13}$$

$$\dot{\phi} = \frac{V\cos\psi\cos\gamma}{r} \tag{2.14}$$

$$\dot{V} = -\frac{D}{m} - g_r\sin\gamma - g_\phi\cos\gamma\cos\psi + \omega^2 r\cos\phi(r\sin\gamma\cos\phi - \cos\gamma\sin\phi\cos\psi) \tag{2.15}$$

$$\begin{aligned}\dot{\gamma} = \frac{1}{V}[\frac{L}{m}\cos\sigma + \frac{Q}{m}\sin\sigma + \left(\frac{V^2}{r} - g_r\right)\cos\gamma + g_\phi sin\gamma\cos\psi \\ + 2\omega V\cos\phi\sin\psi + \omega^2 r\cos\phi(\cos\gamma\cos\phi + \sin\gamma\cos\psi\sin\phi)]\end{aligned} \tag{2.16}$$

$$\begin{aligned}\dot{\psi} = \frac{1}{V}[\frac{L\sin\sigma}{m\cos\gamma} - \frac{Q\cos\sigma}{m\cos\gamma} + \frac{V^2}{r}\cos\gamma\sin\psi\tan\phi + g_\phi\frac{\sin\psi}{\cos\gamma} + \\ 2\omega V(\sin\phi - \tan\gamma\cos\psi\cos\phi) + \frac{\omega^2 r}{\cos\gamma}\sin\psi\sin\phi\cos\phi]\end{aligned} \tag{2.17}$$

Gravitational Model

Employed gravitational model for the radial and latitudinal components up to J_2 term is reported on Equation 2.18 [13].

$$\begin{aligned} g_r &= \frac{\mu}{r^2}\left[1 + J_2\left(\frac{R_M}{r}\right)^2(1.5 - 4.5\sin^2\phi)\right] \\ g_\phi &= \frac{\mu}{r^2}\left[J_2\left(\frac{R_M}{r}\right)^2(3\sin\phi\cos\phi)\right]\end{aligned} \tag{2.18}$$

2.2.2. Inertial Cartesian

The dynamic equation of the Inertial Cartesian equation of motion is the direct application of Newton's law, where the translational motion of a rigid body is described by the derivative in time of its movement quantity, defined as $\boldsymbol{p} = \boldsymbol{m} \cdot \boldsymbol{v}$. Assuming the mass to be a scalar constant quantity, it reduces to Equation 2.19.

$$\begin{aligned} \frac{d\boldsymbol{V}_I}{dt} &= \frac{\boldsymbol{F}_I}{m} \\ \frac{d\boldsymbol{x}_I}{dt} &= \boldsymbol{V}_I \end{aligned} \tag{2.19}$$

The $\boldsymbol{F}_I$ vector stands for the external forces applied to the vehicle. During the atmospheric flight, aerodynamic forces shall be considered on top of gravitational ones. The aerodynamic forces are defined on the aerodynamic reference frame and shall be transformed into the inertial one. This transformation can be achieved by $\boldsymbol{C_{I,A}} = \boldsymbol{C_{I,R}} \boldsymbol{C_{R,V}} \boldsymbol{C_{V,A}}$, where the unitary transformation matrices can be found in Appendix A.

Gravitational Model

The gravitation model, including the J_2 effect on Cartesian inertial components, is reported on Equation 2.20 [77].

$$\begin{aligned} g_x &= -\frac{3}{2}\mu J_2 \frac{R_M^2}{r^5} x \left(1 - 5\frac{z^2}{r^2}\right), \\ g_y &= -\frac{3}{2}\mu J_2 \frac{R_M^2}{r^5} y \left(1 - 5\frac{z^2}{r^2}\right), \\ g_z &= -\frac{3}{2}\mu J_2 \frac{R_M^2}{r^5} z \left(1 - 5\frac{z^2}{r^2}\right), \end{aligned} \tag{2.20}$$

2.2.3. Validation

The relative spherical equations of motion have been validated by comparing the results with ones in Cartesian inertial equations of motion. If both propagators provide equivalent results, using the two completely different models presented implies the correctness on both sets, as getting the same results with two different wrong models would be improbable, as the same error should have happened on both systems.

A Matlab implemented fifth order Runge Kutta fixed step h=0.1[s] has been used, for which higher information will be given in section 2.5. The relative spherical state variables

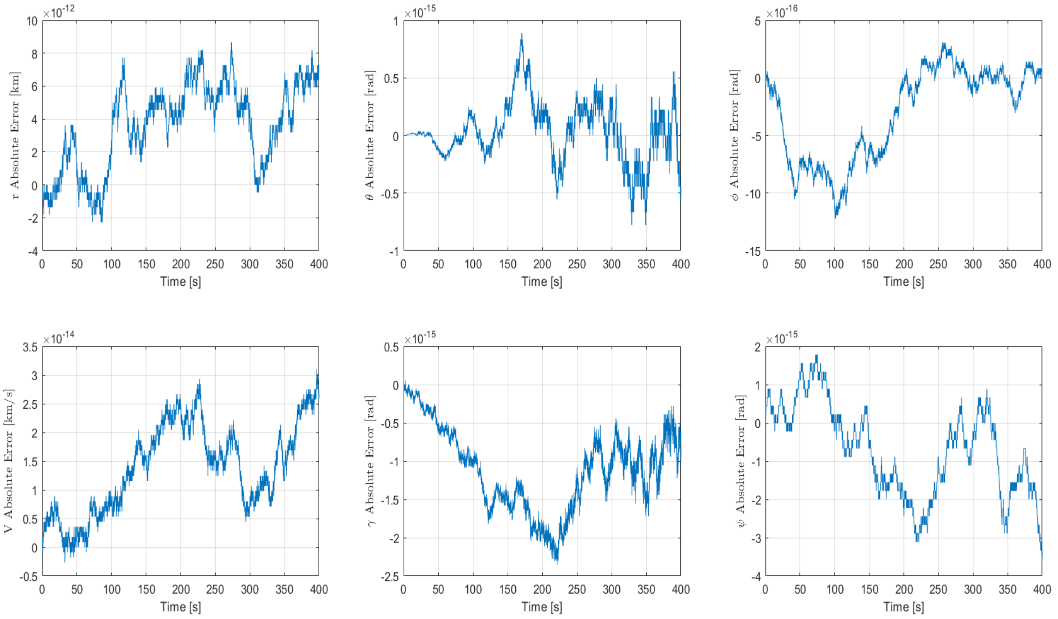

Figure 2.6: Absolute Error between Inertial Cartesian and Spherical Rotational Dynamics

to Cartesian transformation, and its inverse, are reported in Appendix D. Rotational spherical variables are employed for the comparison, and the absolute error for each state variable will be provided.

Planar aerocapture trajectory, full lift-down to full lift-up, with subsection 2.3.2 atmosphere is conducted. Obtained results are reported on Figure 2.6, with a maximum error of 8.64 [nm] for the position. Therefore, dynamic equations can be considered to be verified.

2.3. Atmospheric Models

The reference atmospheric model used during this thesis is *'MarsGram 2010'* engineering-level model. Its applications include aerocapture and aerobraking, making it the perfect fit for the present study [35]. The model is based on NASA Ames NASA Ames Mars General Circulation Model (MGCM) and the University of Michigan Mars Thermospheric General Circulation Model (MTGCM). Its perturbation modelling capability is usually used in Monte Carlo mode, providing the capability of performing high-fidelity engineering simulations. Modifying the dust optical depth parameter also accounts for dust storm simulations' capability. The model is FORTRAN 90/95 based, and a wrapper is required for its use on Matlab. *MEMM* Engineering tool has been used for this purpose. More information on it is provided on Appendix D.

MarsGram is a high-fidelity, computationally intensive model. During some parts of the study, not such a level of precision is required. Less precise but computationally faster models are preferred. These are presented in the following subsections.

2.3.1. Exponential Model

The exponential atmosphere is a well-known model for computing the atmospheric density profile. Where a single-stage exponential function is employed, this is the roughest density model used in the study. It presents the advantage of providing excellent computational efficiency. Its use will be limited where trends want to be analysed and not precision results are required for the computations.

$$\rho(h) = \rho_0 e^{-h/H_s} \tag{2.21}$$

The term ρ_0 stands for the density encountered at zero altitude on Mars, and extracted from MarsGram's nominal density has been set to 0.0123 [kg/m^3]. H_s stands for the Mars' scale height and can be found to be 11.1[km] [53].

2.3.2. Piece-wise Linearization

An intermediate resolution is also required, as the exponential model's predictions diverge towards higher atmospheric altitudes. This model shall provide a better representation of the atmosphere while maintaining a low computational cost.

The density's first-order state variable is altitude. Discarding second-order variables and lumping the variable for zero longitude and latitude, the MarsGram's nominal, high and low-density profiles are stored on 500 element equidistant array spanning from 0 to 150 kilometres in altitude. A piece-wise linear interpolation is performed for altitudes between two array values. The model results are compared to MarsGram's 2000 array value on the application region, and results are reported on Figure 2.7 for the nominal value model. The same result is found for low and high-density profiles since the exact discretisation is employed. The percent error stands for the good representation achieved by this model. A smaller percent error than 1% can be found, leading to precise but computationally efficient modelling of Mars' density profiles.

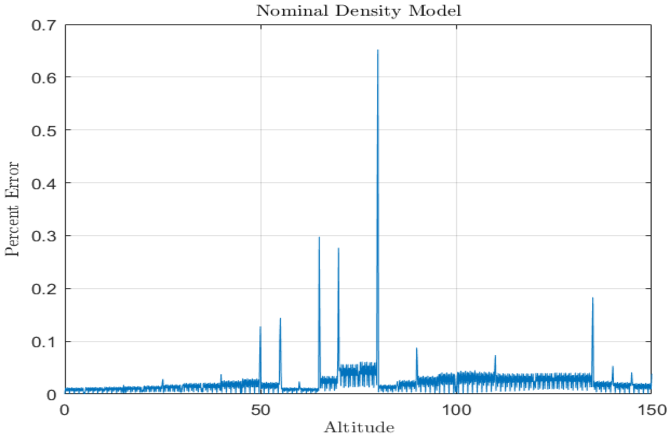

Figure 2.7: Percent Error of Piece-wise Atmospheric Model

2.4. Aeroheating

The model will be based on the stagnation point aeroheating as not a detailed heat modelling is pretended. This assumption can be stated to be a conservative approach, where the heat environment is computed on the worst-case scenario. Since heats are introduced constraint-wise from the vehicle capability perspective, this is sufficient at the current development stage.

The model used is the one presented in [82]. An engineering correlation for Mars Entry Vehicles is developed, considering available information from recent experimental testing. For the convective heating, a Sutton-like equation was found to correctly fit the experimental data Equation 2.22 [82].

$$\dot{Q}_{Conv} = 7.207\rho^{0.47}R_N^{-0.54}V^{3.5} \tag{2.22}$$

On the contrary, the radiative heat at Mars, even if depreciable, when compared to convective as stated by [84], required separation between high and low velocities and a high-order 35th-order polynomial regression. The polynomials are introduced on Equation 2.23. The low-velocity correlation spans from 2 to 6 km/s velocity and the polynomial coefficients are reported on Table 2.2. The high-speed correlation stands for velocities higher than 6 km/s [82], and polynomial coefficients can be found on Table 2.3.

$$\dot{Q}_{Rad} = e^{f(V,\rho,R_N)} \tag{2.23}$$

Table 2.2: Low Velocity Radiation Correlation Polynomial Coefficients.

Term	Coefficient	Term	Coefficient	Term	Coefficient	Term	Coefficient	Term	Coefficient
Constant	-2.1851	$ln(\rho)^2$	0.0674	VR_N^2	-2.7369e-03	$V^3\ln(\rho)$	-6.4747e-03	V$ln(\rho)^2R_N$	2.3530E-04
V	2.7138	$\ln(\rho)R_N$	-0.1056	V $\ln(\rho)R_N$	0.0108	V^3R_N	-2.9409e-03	V $\ln(\rho)R_N^2$	-7.4458E-04
$\ln(\rho)$	0.5949	R_N^2	-0.0545	$\ln(\rho)$	30.0114	$V^2\ln(\rho)$	24.4518e-04	$\ln(\rho)$	42.2040E-04
R_N	0.0400	V^3	-0.3602	$ln(\rho)^2R_N$	-3.8751e-03	$V^2\ln(\rho)R_N$	2.2275e-03	$ln(\rho)^3R_N$	-2.5058E-04
V^2	0.8212	$V^2ln(\rho)$	0.0660	$ln(\rho)R_N^2$	2.5431e-03	$V^2R_N^2$	5.5876e-04	$ln(\rho)^2R_N^2$	-1.5449E-04
V$\ln(\rho)$	0.1017	V^2R_N	0.0386	R_N^3	3.8852e-03	V$ln(\rho)^3$	2.5481e-04	$ln(\rho)R_N^3$	-5.8732E-05
VR_N	-0.0220	V $ln(\rho)^2$	0.0259	V^4	0.0326	VR_N^3	-2.1412e-04	R_N^4	-7.0997E-05

Table 2.3: High Velocity Radiation Correlation Polynomial Coefficients.

Term	Coefficient	Term	Coefficient	Term	Coefficient	Term	Coefficient	Term	Coefficient
Constant	-776.1295	$ln(\rho)^2$	-0.8472	VR_N^2	-7.7139e-3	$V^3\ln(\rho)$	0.1704	V$ln(\rho)^2R_N$	2.9523e-3
V	327.0352	$\ln(\rho)R_N$	-0.2324	V $\ln(\rho)R_N$	0.0310	V^3R_N	0.0125	V $\ln(\rho)R_N^2$	1.9937e-4
$\ln(\rho)$	-69.4125	R_N^2	-0.0615	$\ln(\rho)$	-0.0352	$V^2ln(\rho)^2$	3.8018e-3	$ln(\rho)^4$	1.6924e-4
R_N	-4.8702	V^3	2.5044	$ln(\rho)^2R_N$	-0.0385	$V^2\ln(\rho)R_N$	1.3922e-3	$ln(\rho)^3R_N$	-1.2821e-3
V^2	-46.6552	$V^2ln(\rho)$	-3.6385	$ln(\rho)R_N^2$	-0.0155	$V^2R_N^2$	7.4385e-4	$ln(\rho)^2R_N^2$	-6.1914e-4
V$\ln(\rho)$	28.0329	V^2R_N	0.0386	R_N^3	6.8871e-4	V$ln(\rho)^3$	9.9250e-3	$ln(\rho)R_N^3$	5.8098e-5
VR_N	2.1226	V$ln(\rho)^2$	0.2091	V^4	-0.0256	VR_N^3	-1.4599e-5	R_N^4	-1.9117e-7

2.5. Integrators Study

2.5.1. Dimensional Dynamics

To address the integrator selection to be used in the different phases of the study, a first reference shall be considered preliminarily for the comparison. In this case, a fixed size step integrator Runge-Kutta of eighth order has been used following [41]. The step size for the propagation has been set to h=0.01, and a planar aerocapture trajectory has been computed, with a control switch during aerocapture, to introduce difficulties for the solver.

Secondly, Matlab's built-in variables step integrators 'ODE113','ODE45','ODE78','ODE23', have been used for the comparison setting fixed *'AbsTol'=1e-14*. With the sole variation of the *'RelTol'* parameter, the compared result is the radius of apoapsis obtained from the aerocapture manoeuvre by use of Equation 3.7 and the deterministic atmospheric model reported on subsection 2.3.2. Results are reported on 2.9a and show a convergence of the variable step solvers toward lower values of the relative tolerance. The worst performing solvers are 'ODE78' and 'ODE45', requiring lower relative tolerance to converge into the result. The convergence of the solvers' is found to be 8.8 kilometres.

Even if the convergence is found for higher relative tolerance, the figure of merit to be looked for in terms of computational burden is the number of function evaluations. Hence, the number of function evaluations for the relative tolerance where they have converged is reported in Table 2.4. The best-performing integrator when the Absolute Tolerance

Table 2.4: Dimensional Variable Step Solver Convergence fixed ‘AbsTol’=1e-14

Integrator	Converged RelTol	Number of Function Evaluations
ODE113	$10^{-}9$	$5 \cdot 10^3$
ODE45	$10^{-}11$	$1 \cdot 10^4$
ODE78	$10^{-}12$	$5 \cdot 10^4$
ODE23	$10^{-}9$	$1 \cdot 10^3$

is fixed is ‘ODE113’, requiring almost an order of magnitude lower number of function evaluations.

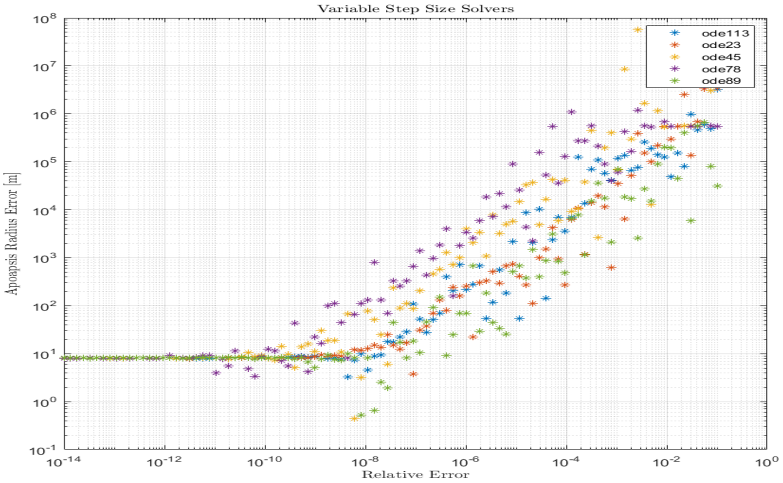

Figure 2.8: Dimensional Variable Step Integrators Convergence fixed ‘AbsTol’=1e-14

Now vary the absolute tolerance of the solvers, and fix the corresponding relative tolerance to the convergence value reported on Table 2.4. For the comparison, the apoapsis radius reference is now substituted by the obtained from the converged value of previous solvers. The results are reported on Figure 2.9. The required number of function evaluations from ‘ODE113’ is comparatively smaller until absolute tolerance 10^{-9}, and in this region, better agreement on the result occurs. Therefore, ‘ODE113’ provides the best-performing results among variable-size step integrators implemented in Matlab. These results will be later used on the integrators’ selection justification.

Also, fixed step Runge-Kutta integrators ‘ODE1’,‘ODE2’,‘ODE3’,‘ODE4’, and ‘ODE5’ have been studied. Results of the convergence analysis are reported on Figure 2.10. To be within 10 meters of error on the apoapsis, the size of the integrator shall be within $h \approx 0.01[s]$. Assuming an average aerocapture trajectory can take around 800 seconds to be completed, considering the lower number of function evaluations given by the second-order Runge Kutta integrator. The number of function evaluations would be

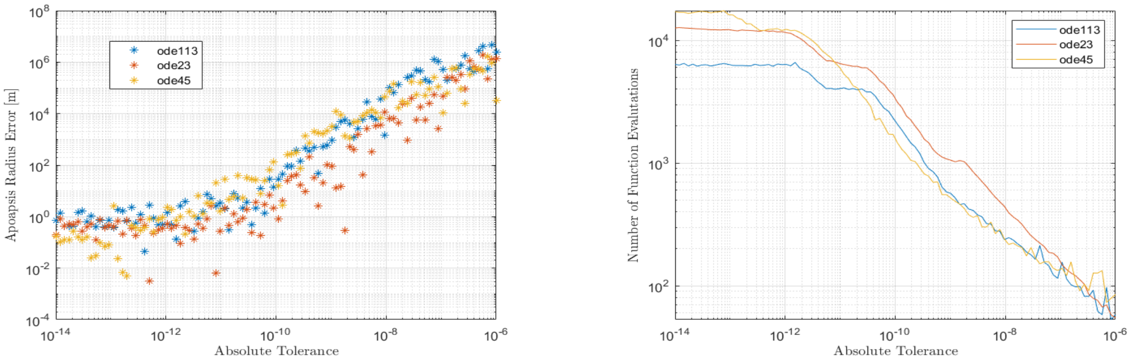

(a) Error on r_a of Integration. (b) Number of Function Evaluations

Figure 2.9: Dimensional Variable Step Integrators Convergence for Variation on ‘AbsTol’

$2 \cdot \left(\frac{800}{0.01}\right) = 1.6 \cdot 10^5$ function evaluations. These results are more than an order of magnitude more computationally expensive when compared to variable step solvers. The expected polynomial convergence rate of the integrators is not the expected theoretical one and could be caused by the high level of discontinuities to be faced during the integration. Atmospheric neat exponential behaviour, and aggressive control actions on the angle-of-attack, could be responsible for the shown behaviour.

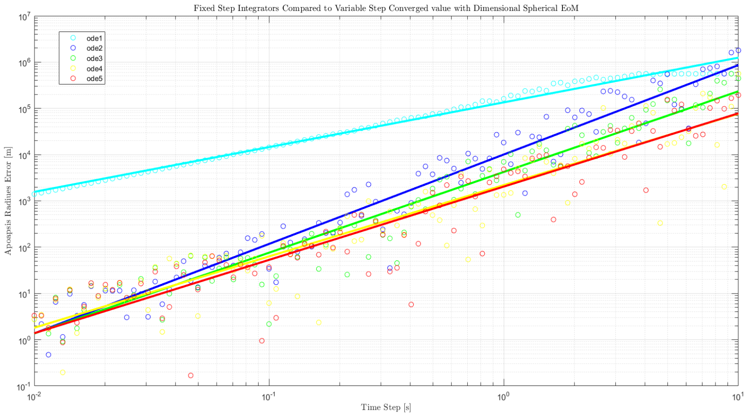

Figure 2.10: Dimensional Fixed Step Convergence Analysis

2.5.2. Dimension-less Dynamics

The non-dimensional set of dynamic equations has also been studied, as it could be computationally advantageous. For the normalisation of the length, the time and the velocity, the scale parameters reported on Equation 2.24 are introduced on the dynamic equations. For example, the aerodynamic accelerations can be normalised as reported on Equation 2.25. As the aerodynamic model is built on top of dimensional equations, these normalisations shall be performed at each stage, consequently increasing the number of operations performed at each integrator's function evaluation. The overall result will determine whether this approach is computationally advantageous or not.

$$\begin{cases} t_s = \sqrt{\dfrac{R_M^3}{\mu}}[s] \\ r_s = R_M[km] \\ V_s = \sqrt{\dfrac{\mu}{R_M}}\left[\dfrac{km}{s}\right] \end{cases} \tag{2.24}$$

$$\overline{\boldsymbol{a}}_{Aero} = \frac{t_s}{V_s}\boldsymbol{a}_{Aero} \tag{2.25}$$

The equivalent convergence analysis in dimensional dynamics is performed, obtaining comparable results for fixed and variable step size solvers, reported on Figure 2.11. It shall be noted that the size of the step shall also be normalised. The same conclusion for the dimensionless equations can be depicted from the obtained results.

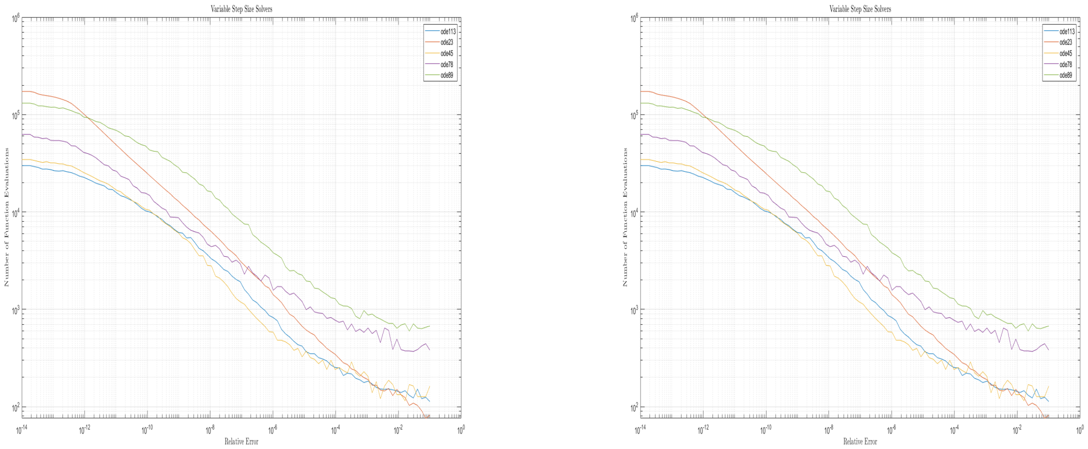

(a) Error on r_a of Integration Variable Step size Solvers

(b) Number of Function Evaluations

Figure 2.11: Dimensionless Step Integrators Convergence Analysis

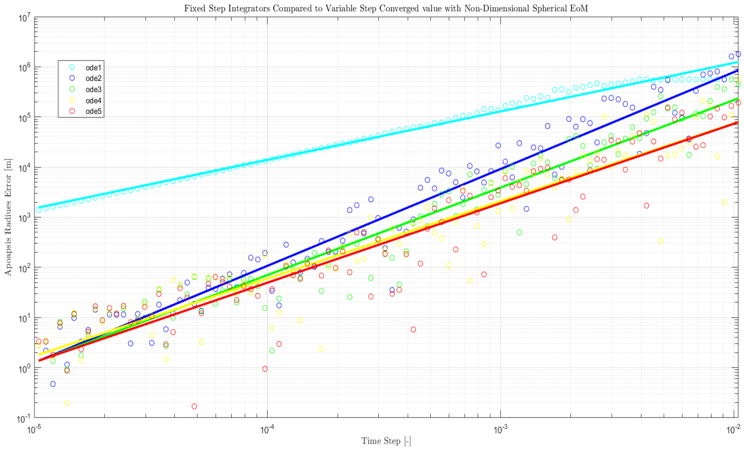

(c) Error on r_a of Integration Fixed Step Solvers

Figure 2.11: Dimensionless Step Integrators Convergence Analysis

2.5.3. Required Computational Time

The present study has been performed without a real-time operating system. Therefore, results shall be looked on a comparative way, and the operating system's internal subprocesses may produce dispersion on time. To prevent any of the scenarios commented on, the study has been performed for 100 samples, and the integrations have been performed alternately.

The mean shows that shorter computational time is obtained on dimensional equations Figure 2.12. This could come from implementation-wise matters, as the aerodynamic forces and gravity accelerations are dimensionally introduced to the function, and an extra computation shall be performed. So each time the gravity or the aerodynamic forces are called, the non-normalised variables shall be introduced on their respective functions. Then, their output shall be normalised before being introduced to the equation of motion.

2.5.4. Conclusions

On the online guidance, two integrators must be present. One corresponds to the NPC, which shall perform several integrations at every guidance call, and computational velocity is preferred at the cost of reducing its accuracy. Conversely, the online propagator will only require single and shorter propagation from t_k till t_{k+1} at each guidance call, and better resolution is preferred.

'ODE113' outperformed the other set of solvers. Fixing the Absolute Tolerance for the

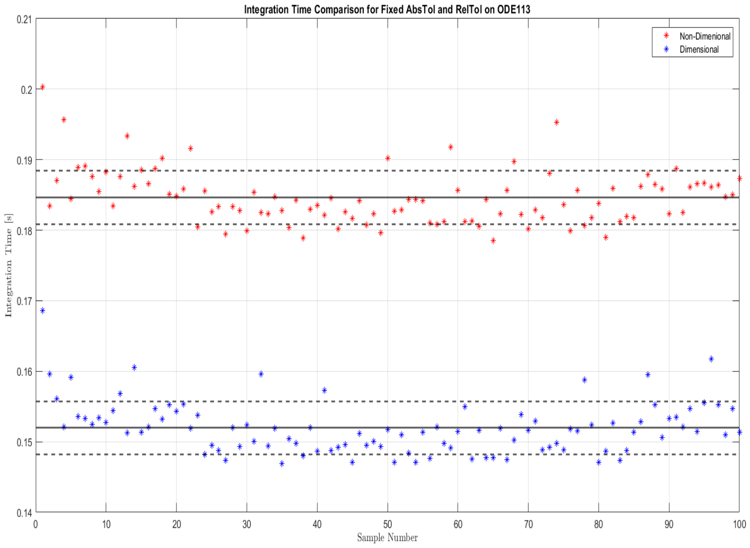

Figure 2.12: Computational time for Dimensional and Dimensionless Propagation

convergence one and varying the Relative, Figure 2.13 is obtained. In 2.13b, it can be appreciated how a significant decrease in the number of function evaluations for ‘RelTol’ of 1e-9, at the cost of 10 meters error on the radius of apoapsis altitude. This trade-off between accuracy and performance perfectly suits the requirements of the NPC integrator and has been chosen for this purpose. For the predictor case, milder integration requirements are introduced and are not required to perform extensive integrations. Hence, an error below 5 m can be considered adequate.

2.6. Real System

The real system is used as a simulation test-bed for guidance. Higher fidelity models are implemented to capture better the trajectory’s reality. The real system is of paramount importance for Monte Carlo and sensitivity analysis results validity.

2.6.1. Atmospheric Model

‘MarsGram 2010’ model, already introduced on section 2.3, has been employed for the simulations of outer loop. For its implementation on the trajectory, a function calling the MEMM engineering tool has been developed. The function updated the input’s file time and position-related components at each instant of the trajectory.

The two main parameters retrieved on the real system modelling from MarsGram are the

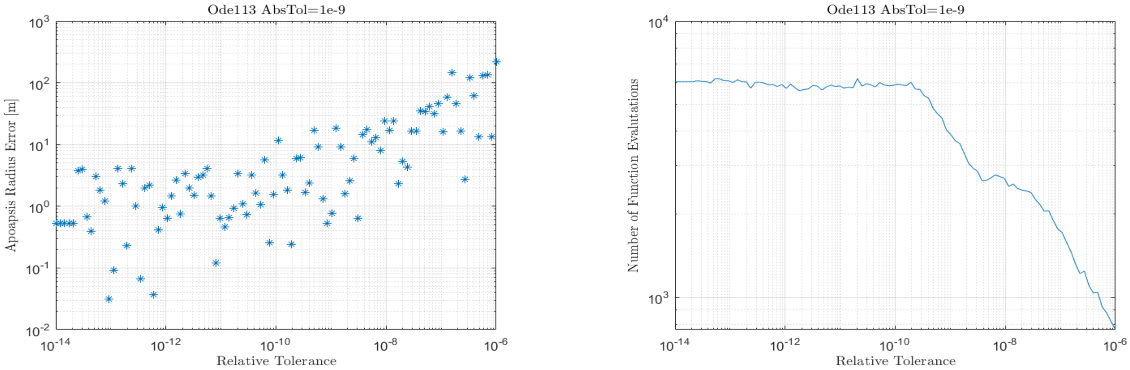

(a) Error on r_a of Integration

(b) Number of Function Evaluations

Figure 2.13: ‘ODE113’ Trade-off Analysis

density and wind velocities, as the guidance wants to be studied in the presence of dust storms. Provided Monte Carlo capability has been exploited to obtain the behaviour on the simulated perturbed environment.

2.6.2. Aerodynamic Coefficients

The 2-Dimensional aerodynamic study obtained results to obtain the control limits reported on Appendix B has been used for the real system. In this case, a two-dimensional linear interpolation is used to compute intermediate values. This model’s critical point is not to precisely follow the aerodynamic study’s outcome, since a preliminary aerodynamic study has been performed. Its main objective is to provide a systematic error compared to the online model of the aerodynamic coefficients.

Even if a high-fidelity aerodynamic study is performed, some simplifications will be introduced for its onboard implementation, and such an error will exist. Hence, the guidance scheme shall be capable of dealing with it satisfactorily. A different implementation could have been introduced. For example, introducing a 10% perturbation to the online model. However, this implementation does not introduce the systematic error the DFC considers for its implementation, and the 2-D modelling has been preferred as a result.

2.6.3. Winds Implementation

The algorithm introduced in [51] has been applied to implement the winds into the dynamics. The equations of motion are ground-based, while the aerodynamic forces are based on the velocity with respect to the atmosphere. Consequently, if the wind velocity and the direction differ, the resulting trajectory with respect to the ground may change.

These winds may be considered a perturbation at hypersonic velocities because of the high vehicle speed. However, wind gusts are expected to be faced in the presence of dust storms. Its modelling would provide a further taste of realism and will address the online guidance robustness.

From MarsGram, the winds in m/s can be retrieved. Given the wind vector on the local-vertical local-horizontal reference frame, the wind parameters are computed from Equation 2.26.

$$\begin{cases} V_w = \sqrt{v_x^2 + v_y^2 + v_z^2} \\ \gamma_w = -\arcsin\left(\dfrac{v_z}{V_w}\right) \\ \psi_w = \arctan\left(\dfrac{v_y}{v_x}\right) \end{cases} \tag{2.26}$$

The airspeed components computation is performed through Equation 2.27.

$$\begin{cases} V_A^2 = V^2 + V_w^2 - 2VV_w(\cos\gamma\cos\gamma_w\cos(\psi_w - \psi) + \sin\gamma\sin\gamma_w) \\ \psi_A = \arctan\left(\dfrac{\sin\gamma\cos\gamma V - \sin\psi_w\cos\gamma_w V_w}{\cos\psi_w\cos\gamma V - \cos\psi_w\cos\gamma_w V_w}\right) \\ \gamma_A = \arcsin\left(\dfrac{\sin\gamma V - \sin\gamma_w V_w}{V_A}\right) \end{cases} \tag{2.27}$$

Given the ground-speed components for the aerodynamic angles, as they are known since they will be commanded from the guidance scheme, the airspeed-based angles are computed. From $\boldsymbol{C}_{B,TA} = \boldsymbol{C}_{B,V}\boldsymbol{C}_{V,TA}$, where the transformation matrices are described on Equation 2.28. The aerodynamic attitude with respect to the airspeed can then be computed from Equation 2.29.

$$\begin{cases} \boldsymbol{C_{B,V}} = \boldsymbol{C_2}(\alpha)\boldsymbol{C_3}(-\beta)\boldsymbol{C_1}(-\sigma)\boldsymbol{C_2}(\gamma)\boldsymbol{C_3}(\psi) \\ \boldsymbol{C_{V,TA}} = \boldsymbol{C_3}(-\psi_A)\boldsymbol{C_2}(-\gamma_A) \\ \boldsymbol{C_{B,TA}} = \boldsymbol{C_2}(\alpha_A)\boldsymbol{C_3}(-\beta_A)\boldsymbol{C_1}(-\sigma_A) \end{cases} \tag{2.28}$$

$$\begin{cases} \beta_A = \arcsin\left(\boldsymbol{C_{B,TA}}(2,1)\right) \\ \alpha_A = \arctan\left(\dfrac{\boldsymbol{C_{B,TA}}(3,1)}{\boldsymbol{C_{B,TA}}(1,1)}\right) \\ \sigma_A = \arctan\left(-\dfrac{\boldsymbol{C_{B,TA}}(2,3)}{\boldsymbol{C_{B,TA}}(2,2)}\right) \end{cases} \tag{2.29}$$

From Equation 2.29, the airspeed aerodynamic force components are computed and transformed into the ground-based frame of the equation of motion Equation 2.30. Where the transformation matrix is defined as $\boldsymbol{C_{AG,AA}} = \boldsymbol{C_1}(-\sigma)\boldsymbol{C_2}(\gamma)\boldsymbol{C_3}(\Delta\psi_{GA})\boldsymbol{C_2}(-\gamma_A)\boldsymbol{C_1}(\sigma_A)$. Finally, the obtained forces are introduced in the dynamic equations. This process is computed sequentially.

$$\boldsymbol{F_{A,AG}} = \boldsymbol{C_{AG,AA}}\boldsymbol{F_{A,AA}} \tag{2.30}$$

2.7. Fully-Propulsive Computations

For every point in the hyperbolic trajectory, the Equation 2.31 stands, from which the hyperbolic excess velocity given the atmospheric entry interface condition can be computed.

$$\frac{V_I^2}{2} - \frac{\mu}{r} = \frac{V_\infty^2}{2} \tag{2.31}$$

The orbital insertion is computed through Equation 2.32 [26]. If the final target orbit is circular, the velocity for the periapsis can be computed through Equation 2.33.

$$\Delta V_{FP} = \sqrt{V_\infty^2 + \frac{2\mu}{r_p^*}} - V_p^* \tag{2.32}$$

$$V_{Circular} = \sqrt{\frac{\mu}{r_p^*}} \tag{2.33}$$

Using Tsiolkovsky's rocket equation, the propellant mass is computed through Equation 2.34.

$$m_p = m_0 \left(1 - \exp\left(-\frac{\Delta V}{I_{sp} g_0}\right)\right) \tag{2.34}$$

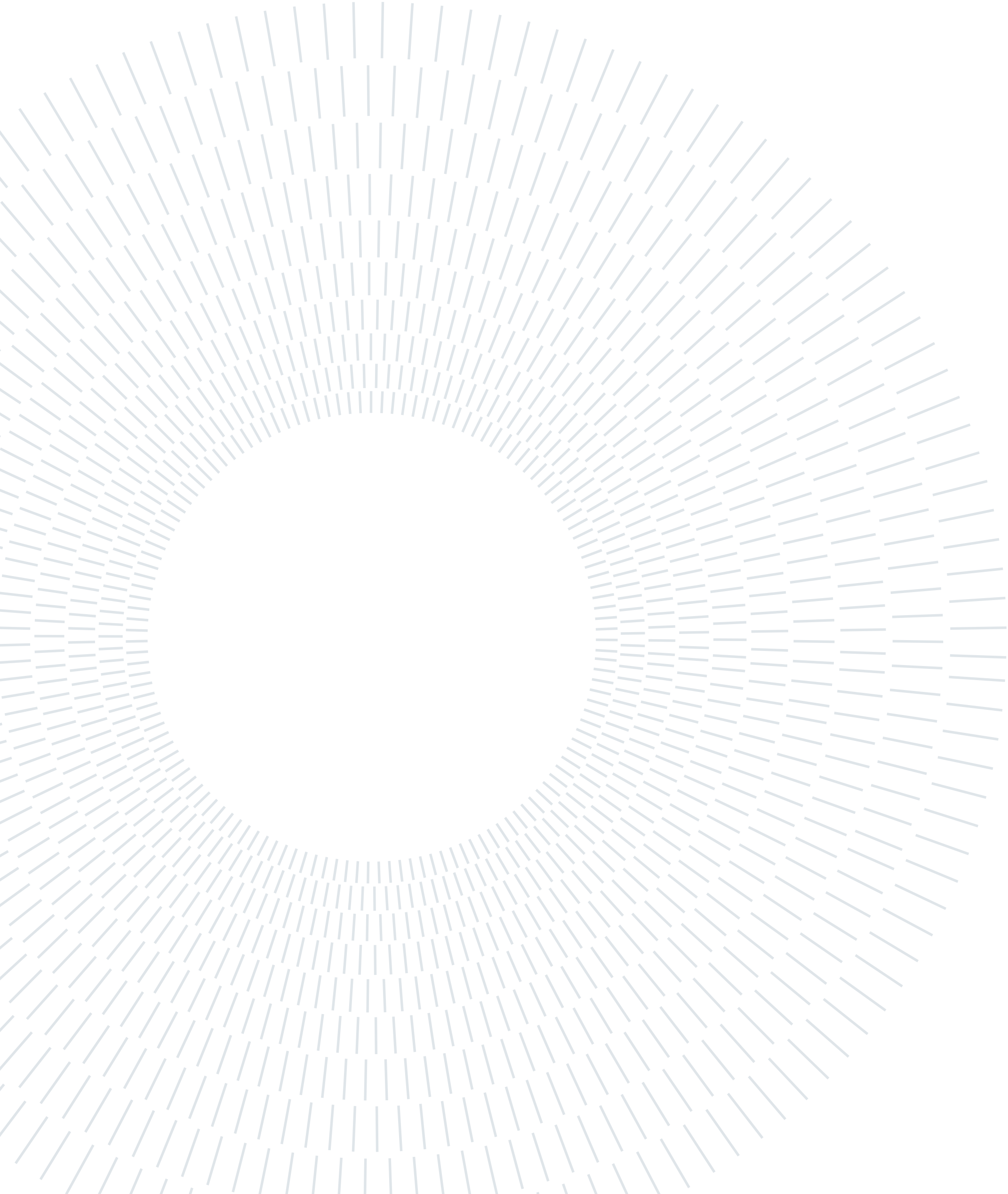

3 | DFC Feasibility for SmallSats at Mars

This chapter aims to answer the first research question in section 1.2. A brief overview of the solution structure will be given and the reasoning behind it will be explained. To get a clear picture of the problem feasibility trends, the chosen SmallSats limitations are defined, and nominal corridors for several parametric capsule designs are presented. Later, the Operational Corridor is computed using some operational and trajectory constraints, and the feasible region of the trajectory is then determined for the chosen test mission.

3.1. Introduction

Here the solution structure will be presented. Some possible points of concern will be explained, and the assumptions made to get the feasibility results will be provided.

3.1.1. Possible Points of Concern

To the writer's knowledge, no studies of aeroshell-kind capsule-like vehicles exploiting direct force modulation on Mars have yet been conducted. As a result, its applicability needed to be clarified. Some points of concern arise from the constraints on the size of the spacecraft, where the vehicle and trajectory constraints could prevent its feasibility. Another limiting factor could come from the lack of control authority, leading to a non-viable trajectory scenario.

As commented in the introduction chapter, some of the advantages the direct force method could provide, when compared to other aerocapture strategies, would be related to a decrease in the mission's propulsive requirements. Firstly, this could be stated because none of the channels get saturated across the trajectory. This could lead to more robust guidance, capable of dealing with uncertainty throughout the complete atmospheric pass, reducing the error that could be produced, and leading to less expensive exo-atmospheric manoeuvring corrections to achieve the target orbit.

Conversely, the out-of-plane manoeuvre is controlled during the whole trajectory, unlike bank-angle modulation, where the lateral channel is only controlled during the last part, where control reversals are performed. Consequently, it is expected to highly increase the lateral's channel manoeuvrability. As it relates to the longitudinal channel on a second-order dependency, better behaviour on the longitudinal channel would also be expected.

Increasing the number of design mission options is an excellent advantage for mission designers. Different performance and trade-offs will likely happen, allowing the possibility of selecting the option that better suits each mission case. This would increase the number of ride-share missions that could benefit from aerocapture.

Even if commented expected advantages could sound promising, this method's feasibility for the small-satellite class mission on Mars is not guaranteed for aeroshell vehicle kinds, where incremental surface devices are not used, such as previously introduced ADEPTS, HIADS, or IRENE. These devices introduce tighter constraints on the vehicle and the trajectory. The maximum dynamic pressure and maximum heat rate are highly decreased when compared to existing aeroshell-compatible technology for both the structure and the TPS. For example, as provided in [19], HIADS's trajectory would be designed for a maximum dynamic pressure of 4.2 kPa. At the same time, the aeroshell vehicle, such as MSL, could be expected to be within 15.5 kPa [78]. As a result, the possible trajectories that each type could offer are due to each technology's benefits and limitations.

The main concern would be the maximum reference surface appearing on the aerodynamic equation Equation 3.1. Small-satellite mission class has tight volumetric constraints that do affect proportionally on the control authority. Suppose we assume that the aerodynamic coefficient during a hypersonic flight has a small change with the flight speed and Reynolds number. In that case, it can be said that it is only dependent on the vehicle's aerodynamics and the aerodynamic angles of the vehicle. Even if setting the vehicle at its configuration of maximum aerodynamic efficiency, the coefficient is given by the vehicle design, and only a little can be done within this respect apart from a correct aerodynamic design of the capsule vehicle to increase the trajectory's viability.

$$\underline{F}_{Aero} = q_\infty S_{Ref} \begin{pmatrix} C_D(\alpha,\beta) \\ C_\beta(\alpha,\beta) \\ C_L(\alpha,\beta) \end{pmatrix} \tag{3.1}$$

$$q_\infty = \frac{1}{2}\rho(h,\phi,\theta,etc.)V^2 \tag{3.2}$$

Hence, the only remaining term inside the aerodynamic force vector is the dynamic pressure, reported on Equation 3.2. Two terms appear, the density and the free-stream velocity (or aerodynamic speed). The trajectory would provide the velocity, and on aerocapture, this is expected to be very high, at several kilometres per second. Given an entry trajectory from a hyperbolic interplanetary leg into the Mars atmosphere, the only option left would come from the density term. Several factors affect the atmospheric density at Mars, and significant variations could be expected from day-of-flight, considering different seasons, mean sun longitude or solar activity, among others. However, the flight altitude is the most relevant variation, usually considered a first-order variable.

Then, a lower altitude trajectory would be anticipated when a drop in the reference surface exists, as requires depleting the same amount of orbital energy. This lower trajectory would imply higher structural and heat loads on the vehicle due to the expected deeper dive. Hence, the problem's behaviour and trends must be correctly understood on this vehicle kind, and a test mission for one of the most compromising cases shall be studied. Addressing the feasible region correctly, when all the constraints and uncertainties of the problem are added, would lead to demonstrating the mission feasibility. The main question to answer is whether the improvement in structural and heat constraints, provoked by the aeroshell-like vehicles, compensates indeed for the loss in reference surface for the Mars aerocapture mission case.

3.1.2. Assumptions Made

Several assumptions have been made in order to address the feasibility issue. Firstly, the 3DOF spherical rotational equations Equation 2.12-Equation 2.17 of motion have been used for the dynamic modelling. As commented in subsection 2.2.1, these set of equations do present singularities for the following cases: $\gamma = \pm\frac{\pi}{2}$ and $\phi = \pm\frac{\pi}{2}$. For the gravitational model, 'J2' perturbation has been considered to account for Mars' oblateness Equation 2.18.

To lower the computational load, an atmospheric patch of *'MarsGram 2010'* density has been completed. The nominal medium, minimum and maximum density values have been computed at zero longitude and latitude for 500 points spanning from 0 up to 200 kilometres of altitude. A piece-wise linear interpolation is carried out from these positions, as explained in subsection 2.3.2. This loss of precision does not significantly affect the feasibility results, which comes with a significant boost in computational efficiency. This issue might be addressed in the study later by adding an uncertainty component to obtain a conservative approach to the solution.

Second-order dependencies on the aerodynamic coefficients are discarded to entirely decouple the lateral and longitudinal channels. Allowing the drag and lift coefficients to depend solely on the angle of attack, and the lateral coefficient to depend on the side-slip angle Equation 3.3. From this simplification, an error is introduced in the system. For a given small enough error it could be handled in the guidance phase. Therefore, limitations over the maximum and minimum aerodynamic angles to be used are introduced. This limitation would come from the capsule's aerodynamics and would be highly dependent on its aerodynamic behaviour. From [13], a 10% error on aerodynamic coefficients was used in the mission design phase, and the same value has been selected in the present research. These maximum angles will provide the maximum and minimum values of the aerodynamic coefficients for the feasibility study.

$$\begin{cases} c_D(\alpha), \\ c_Q(\beta), \\ c_L(\alpha). \end{cases} \tag{3.3}$$

No wind effect has been introduced in this part of the study, and a more straightforward analysis has been employed. As previously commented, this can be addressed through the uncertainty factor to obtain simple and efficient but conservative results.

For the heat modelling constraints, stagnation point heat rates have been computed. The stagnation point would vary according to the vehicle's attitude and will be somewhere in the bare front of the capsule. On this varying point, the maximum heat loads will be encountered and could be considered the worst-case scenario. As considering point mass actuations, the dynamic pressure value is also considered to be lumped into the vehicle's state and not a distributed value over the capsule. The same consideration as in the heat rate case applies.

3.1.3. Objective of the Chapter

The capsule design logic will be presented in this chapter, and the choice of constraints will be discussed. The capsule parametric design will then be presented, together with the results of its aerodynamic research and the determined trade-off based on the design parameters. The trajectory trends are then examined, the Nominal Corridor result is investigated, and other mission parameters are modified. In order to determine the region where aerocapture is viable, a test mission is selected from the previous results, and the trajectory and vehicle limitations are added to the operational corridor.

3.2. SmallSats Constraints Definition

SmallSat vehicle constraints shall be defined, both on mass and size, as well as on structural and heating-related terms. Some constraints shall also be introduced from the trajectory standpoint to prevent unfeasible trajectories. Its combination will be used to obtain the aerocapture's feasible region given a set of initial conditions and a target orbit.

3.2.1. Spacecraft Category Definition

A clear definition for SmallSat class spacecraft category is needed. According to [4], "The existence of many classifications (based on size categories and mass range values) makes inaccurate their common global characterisation" even in the new classification suggested in the study, the expected SmallSat concept would be somewhere inside the 'Mini' classification, except for Heavy subclass.

This categorisation only deals with the spacecraft masses but not the sizes. Hence, a more pragmatic approach is followed. As an interplanetary mission is intended with a small-satellite class, this is expected to arrive on Mars well at a ride-share mission, or well, by means of an Orbit Transfer vehicle kind, containing several small satellites on it. In any of both cases, the spacecraft would be treated by the rider mission as a secondary payload. Typically, secondary payloads are attached to ESPA class interface rings. According to the selected ring, design constraints are introduced on the vehicle, which would help with the task of realistically defining it.

To sum up, the intended SmallSat concept fits adequately on the ride-share mission-type vehicle, which shall comply with secondary mission constraints. Making the capsule compatible with ESPA ring constraints would imply a realistic spacecraft design. Therefore, this design path has been followed during the research. This decision is in accordance with the vehicle type used on [23] for the study of Drag-Modulation aerocapture on Mars for SmallSats.

3.2.2. ESPA Rings Constraints

The ESPA is the current standard adapter used to send secondary payloads into launch vehicles. Their main advantage comes from reducing the impact on the primary mission and providing standardisation for the secondary missions, which will positively impact development costs.

In agreement with ESPA User's Guide [15], two different kinds of rings are already qualified at the analysis level: ESPA Class and ESPA Grande. The second option would allow for bigger spacecraft both in size and mass. The vehicle constraints of size and interface are reported for these two cases on Table 3.1.

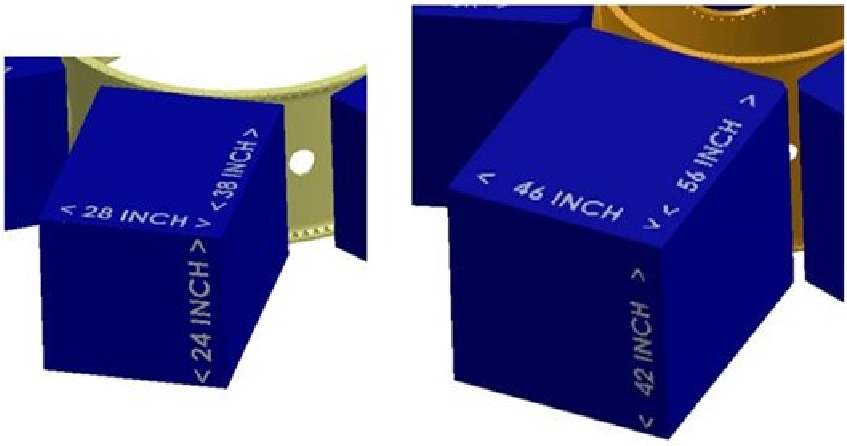

Figure 3.1: ESPA and ESPA Grande Size Constraints [15]

Table 3.1: Qualified ESPA and ESPA Grande contraints [15]

Constraint	ESPA Class	ESPA Grande
Mass	181 [kg]	318 [kg]
Size	71.12x60.96x96.52 [cm]	116.84x106.68x142.24 [cm]
Interface Diameter	38.1 [cm]	60.96 [cm]
CoG Offset	50.8 [cm]	50.8 [cm]

3.2.3. Vehicle Constraints

Apart from the already presented size-related constraints, structural and heat-related ones have yet to be introduced. Some other aeroshell-like limits have been searched for their definition, and similar values have been introduced.

A well-established solution for the thermal protection system is Phenolic Impregnated Carbon Ablator (Pica) aeroshell. This technology presents a maximum heat rate of 1 [kW/cm^2][1]. From [78], 3σ values for the dynamic pressure and load factor are given for MSL mission: 17.2 [kPa] and 14.3 [g's]. As a result, the values reported on Table 3.2 for the test mission case are selected in the present work.

3.2.4. Trajectory Constraints

On Mars, very high mons exist, and a list of them is reported on [83]. The highest are Olympus Mons which presents an elevation of 21.28 [km], which, when compared to the

Table 3.2: Vehicle Selected Constraints

Property	Maximum Value
$\dot{Q}_{Max}$	1 [kW/cm^2]
q_{∞}^{Max}	16 [kPa]
n_{Max}	13 [g's]

highest mountain on Earth, Mount Everest, Olympus Mons, do present more than twice its elevation.

Apart from Olympus Mons, other mons such as Ascraeus, Arsia, Pavonis, Elysium, Tharsis, and Tholus present elevations ranging from 18 to 8 kilometres altitude.

Then it can be concluded that Mars does present a sheer landscape, and a constraint on the flight altitude shall be introduced during the study to prevent a vehicle crash against the mountains. Hence, a conservative value has been considered, applying a 25% margin to Olympus Mons:

- Minimum Flight Altitude of 26.6 kilometres with respect to the equator spheroid.

3.3. Capsules Parametric Design

From subsection 3.2.2 it has been reported that two different ESPA rings are encountered with two different sets of constraints. As explained on subsection 3.1.1, the feasibility of SmallSats is not guaranteed, and the loss on the reference surface could play a significant role in it. As a result, both ESPA rings compatible vehicles are studied to understand how the variations in mass and surface affect the aerocapture manoeuvre.

3.3.1. Design Introduction

A single parameter for parametric aerodynamic characteristic modification by the use of hyperbolic contours is introduced by [54], where it is applied to *'Hayabusha'* entry capsule vehicle, reported on Figure 3.2.

This design concept proves an improvement on the aerodynamic coefficient for the increasing value of the hyperbolic parameter, where some trade-offs are performed. The increase of 'a' also implies an increase in the vehicle's nose radius given by Equation 3.4, leading to lower convective heat loads, which proves beneficial for the mission designer. However, on the other side of the coin, the increase in the aerodynamic coefficients is obtained at the expense of the capsule's available volume reduction 3.3a and of reference

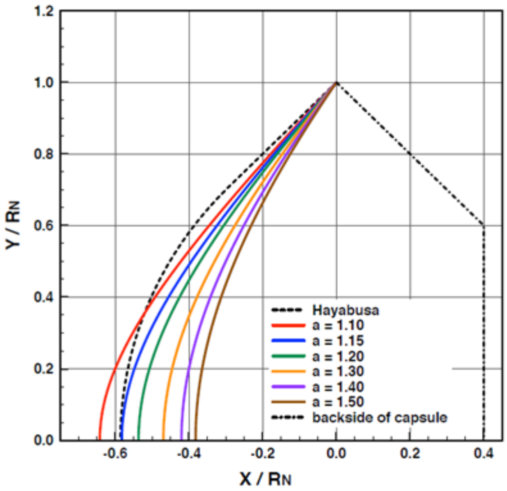

Figure 3.2: Hayabusha Design Hyperbolic Parametrization [54]

surface reduction, as reported on 3.3b. It shall be investigated whether the increase of hyperbolic contour really means an increase in control authority when reference surface loss and aerodynamic coefficient increase are combined on the applicability region of the Direct Force Control.

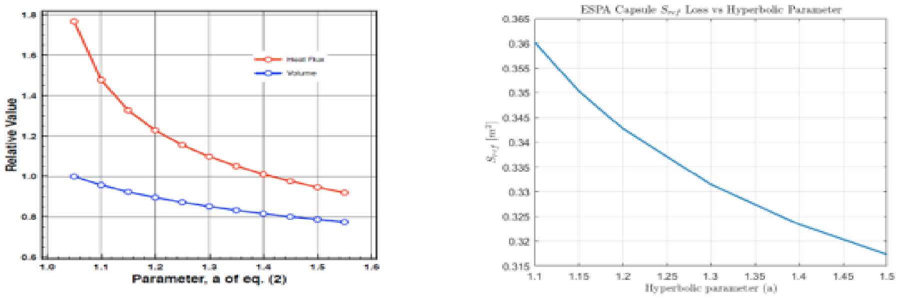

(a) Qualitative Heat vs Volume trade-off [54].

(b) Reference Surface Loss.

Figure 3.3: Vehicle's Design Trade-offs

$$R_N(a) = \sqrt{a^2 - 1} \tag{3.4}$$

[54] Also reports that the static stability of the capsule is not significantly affected by hyperbolic contour utilisation. However, some concerns may arise with regard to dynamic stability during the transonic regime phase. As aerocapture's mission only deals with hypersonic flight regimes, this is not found to be a concern in the present study.

Based on this concept, 12 capsule vehicles have been designed, six compatible with ESPA Class ring constraints and the others with ESPA Grande. Size and interface constraints reported on Table 3.1 have been respected. The design has been conducted by the use of *'SolidWork's Equation Driven Curve'* on the sketch, followed by a *'revolve'* operation for the body creation. Afterwards, the correct scaling factor is applied to get the final capsule's designs, some examples are reported on Figure 3.4. For each ESPA-compatible design, the hyperbolic parameter variation study cases are 1.1, 1.15, 1.2, 1.3, 1.4, and 1.5.

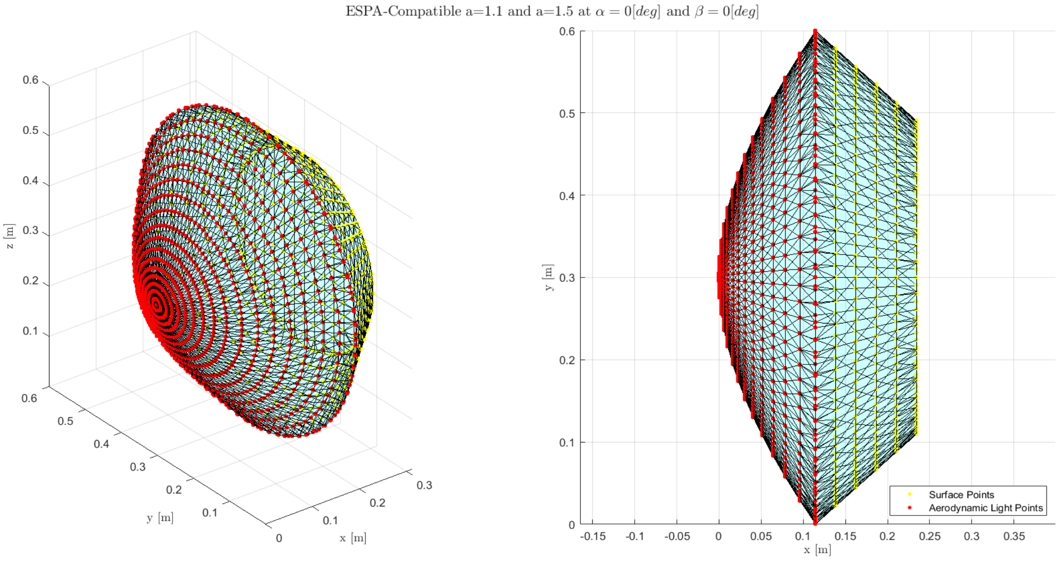

Figure 3.4: Capsule Design

3.3.2. Aerodynamic Results

To perform the aerodynamic study of the designed capsules, an ad hoc developed program that integrates local inclination surface methods has been utilised, introduced in section 2.1. As commented later, the number of discretisation points would affect the aerodynamic solution and shall be selected to balance accuracy and computational burden.

The 1-D aerodynamic coefficients commented on subsection 3.1.2 are obtained from the performed analysis. It can be seen on Figure 3.5 how the increase in the capsule's hyperbolic parameter greatly impacts the aerodynamic coefficients. The loss in reference surface due to the hyperbolic parameter increment shall be accounted for to understand if an overall performance improvement is obtained. To keep it short, 3.5d and 3.5e are reported. The lateral control authority is not much affected. At the same time, the drag is slightly improved, and the lift is substantially increased, reporting a higher L/D ratio 3.5f, which could potentially affect the aerocapture's feasibility. Hence, hyperbolic contour utilisation leads to an L/D improvement.

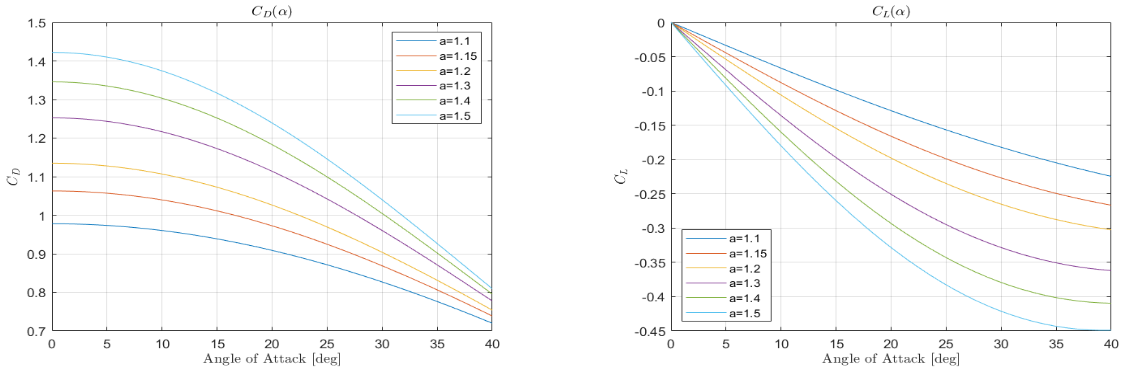

(a) Drag Coefficient. (b) Lift Coefficient.

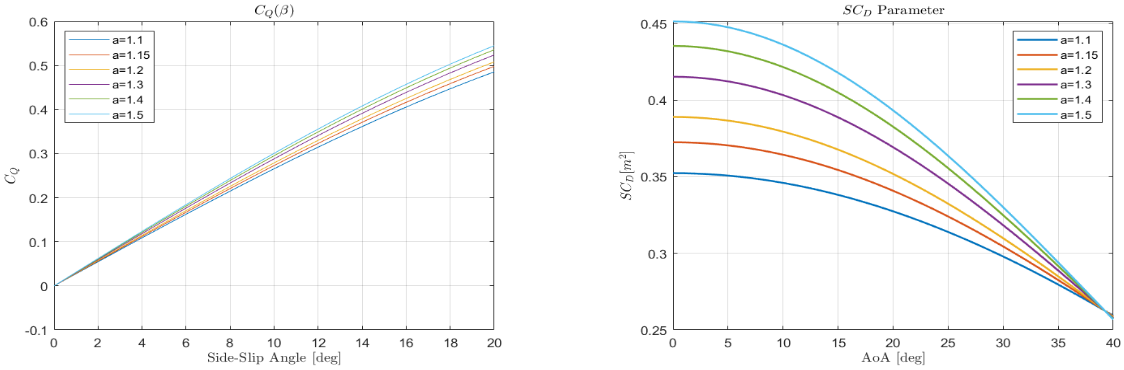

(c) Lateral Coefficient. (d) $S_{Ref}C_D(\alpha)$

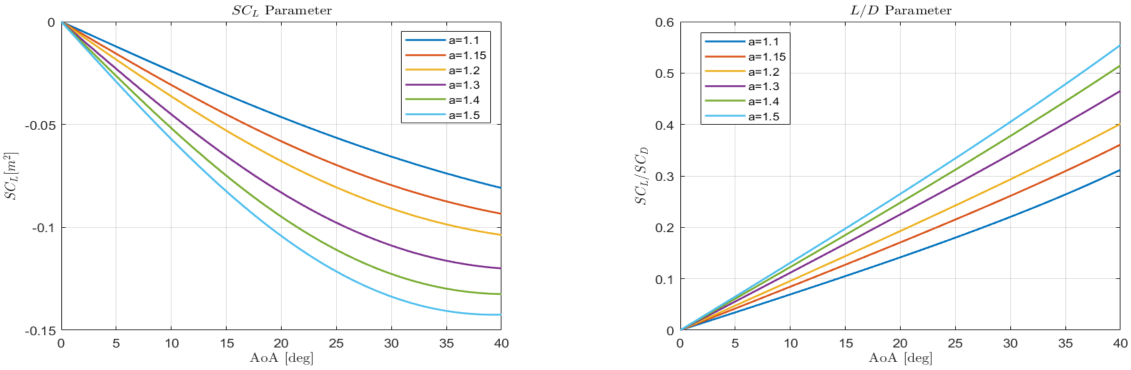

(e) $S_{Ref}C_L(\alpha)$ (f) $L/D(\alpha)$

Figure 3.5: Aerodynamic Coefficients vs Hyperbolic Parameter

The error introduced on the problem from this assumption shall be small; otherwise, problems related to guidance robustness may arise since too much error would be introduced on the guidance model. To represent the difference between the coefficients reported on

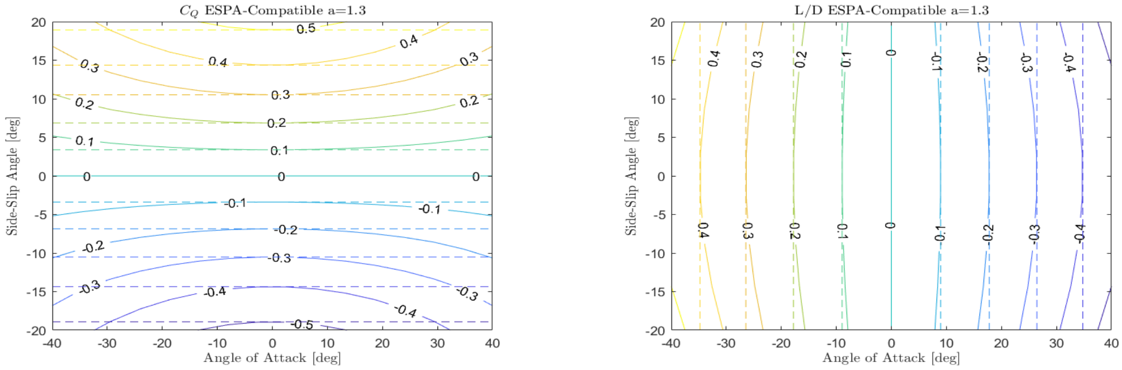

(a) Lateral Coefficient Difference. (b) Aerodynamic Efficiency Difference.

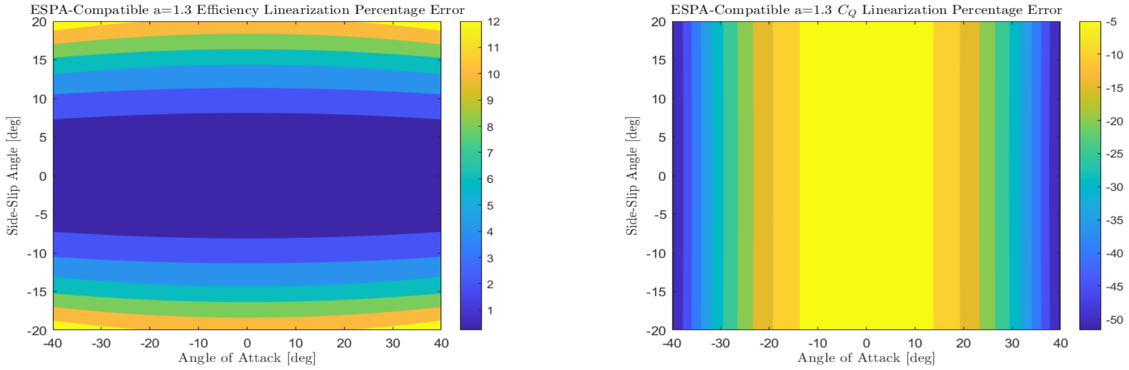

(c) Lateral Coefficient Error. (d) Aerodynamic Efficiency Error.

Figure 3.6: Coefficient Error for ESPA Compatible a=1.3 Capsule

Figure 3.5 and the 2-D coefficients obtained from the aerodynamic study, the Figure 3.6 is reported. In the figure, the values containing a=1.3 for ESPA compatible capsule can be found, similar results are obtained for the rest of the capsules, and the plots are given in Appendix B. It can be appreciated how for increasing the value of the side-slip, the error over the L/D variable increases. While for increasing values of the angle of attack, an increase in the error of the lateral coefficient arises. Similar results are obtained for the 12 designed capsules, and within an approximate 10% error, an aerodynamic angle limitation of 20 degrees has been selected.

It shall be clarified that this is a preliminary aerodynamic study where low-fidelity aerodynamic modelling has been performed. No viscosity-related correlations have been added to improve the expected overestimation of the Newtonian method as they introduce complexity to the problem, and the change introduced on the parameters is small. Hence, small dependencies with Reynolds and flight Mach number have been discarded. The slight variation of the coefficients in hypersonic regime property has been exploited and assumed constant.

3.3.3. Conclusions

The feasibility study shall introduce the L/D parametric aerodynamic design improvement to understand the overall result for aerocapture when DFC is applied. As an overall trend on the 12 designed capsules, a 10% error on 1-D coefficients is obtained for $\alpha = \beta \approx \pm 20$ degrees and has been selected for the maximum and minimum values for the aerodynamic angles.

3.4. Nominal Corridors

The nominal corridors are defined as the set of FPA that fall between the saturated trajectories given a target radius of apoapsis and the atmospheric interface entry conditions. They are tightly related to the control authority of the spacecraft during the trajectory. It can be used to understand the trends provoked by the problem's parameter variation and address the trajectory's feasibility.

3.4.1. Concept

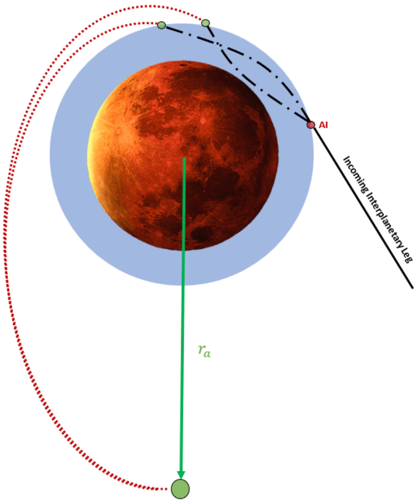

Figure 3.7: Corridor Concept

In the case of the direct force method, the saturated trajectories would correspond to the maximum and minimum angle of attack constantly trimmed trajectories. To better illustrate the corridor concept, Figure 3.7 is reported. In this work, the trajectories will be distinguished as deep and shallow sides of the corridor. The shallow trajectory will dive higher altitudes into the atmosphere, which leads to a longer trajectory to deplete excess orbital energy. Conversely, the deep trajectory will get lower into the atmosphere, producing higher aerodynamic forces and a harsher environment for a lower duration manoeuvre. These trajectories occur for the different pointing sides of the lift vector, which in one case, will add to the centrifugal force and the other, which will compensate for it. As a result, the former case would need to have a steeper trajectory, as it will tend to go out.

The angle that relates to the steepness of the trajectory at the atmospheric entry interface is the flight path angle. The flight path angle is defined as the angle formed by the velocity vector of the spacecraft and the local horizontal plane. This angle is considered negative when it is found to be lower than the horizontal plane, pointing towards the planet. In aerocapture, negative flight path angles at the atmospheric interface are necessary for the vehicle to enter the planet's atmosphere.

The idea of depicting the corridor of the aerocapture trajectory lies within the aim of addressing the problem's feasibility. Considering a given entry state, it shall lay within the range of flight path angles given by the corridor to target the aimed radius of apoapsis by manoeuvring inside the atmosphere. To simplify this idea, let's assume a deterministic atmosphere case. In a given entry state that falls within the corridor of the trajectory, a constant angle of attack could be computed from the initial point till the atmospheric exit that would lead to the target apoapsis. That angle of attack would be within α_{Max} and α_{Min}, as defined by the corridor's limits. Hence, it could be used to address the viability of the different trajectories given an initial state at the atmospheric interface.

The nominal corridors are firstly computed to have a first perspective of the aerocapture feasibility. The main concern on the feasibility aspect of the nominal corridor is whether the deep side of the corridor does not imply a crush on the planet. Vehicle and trajectory constraints will be applied to the selected corridors in the later phase of the study subsection 3.5.2. Also, the nominal corridor's trends will be looked at to understand how the different problem parameters affect the trajectory. From this knowledge, better aerocapture-suited missions could be developed. In the present thesis, these are later used for the test mission definition.

The computations have been conducted by fixing the target radius of apoapsis and giving the same atmospheric entry interface state as introduced on subsection 3.1.2, a 1-D atmosphere has been used. The atmospheric interface entry point has been set at $h = 130[km]$, and the longitude, latitude and heading angles have been initialised to zero. When no special mention is made about the spacecraft's mass, this is assumed to be the maximum reported on Table 3.1. Then, the velocity magnitudes are varied within the expected range of values to be encountered at Mars entry interface Figure 3.8, and the shallow and deep flight path angles are computed through a zero finding problem Equation 3.5, where Keplerian motion was assumed at the atmospheric exit for the radius of apoapsis computation Equation 3.7. As difficulties are caused by the discontinuities produced by the negative radius of apoapsis of hyperbolic trajectories, penalty terms have been introduced to ensure the mathematical resolution's convergence and prevent trajectories that cross through the planet in both cases bounding the solution space.

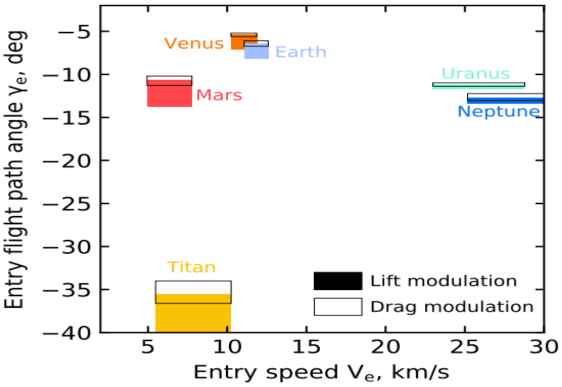

Figure 3.8: Atmospheric Expected Interface Velocities [26]

$$J = r_a - r_a^* \tag{3.5}$$

$$a = \frac{\mu}{\dfrac{2\mu}{r} - V_I^2} \tag{3.6}$$

$$r_a = a\left(1 + \sqrt{1 - \frac{(V_I rcos(\gamma_I))^2}{\mu a}}\right) \tag{3.7}$$

The inertial components can be computed from Equation 3.8 reported on [50]. This equation has been slightly modified to adapt to this thesis's selected heading angle definition. It differs from the one used in their original formulation, where the complementary angle is used instead. Then, it shall be mentioned that the ψ_I will not correspond to the angle used on the equations of motion, and the required transformation shall be applied for inertial to rotational reference frames.

$$\begin{cases} V_I = \sqrt{v^2 + 2\omega r v \cos\gamma \sin\psi \cos\phi + (\omega r \cos\phi)^2}, \\ \tan\gamma_I = \dfrac{v \sin\gamma}{\sqrt{(v\cos\gamma)^2 + 2\omega r v \cos\gamma \sin\psi \cos\phi + (\omega r \cos\phi)^2}}, \\ \tan\psi_I = \dfrac{-v\cos\gamma\cos\psi}{v\cos\gamma\sin\psi + \omega r\cos\phi} \end{cases} \tag{3.8}$$

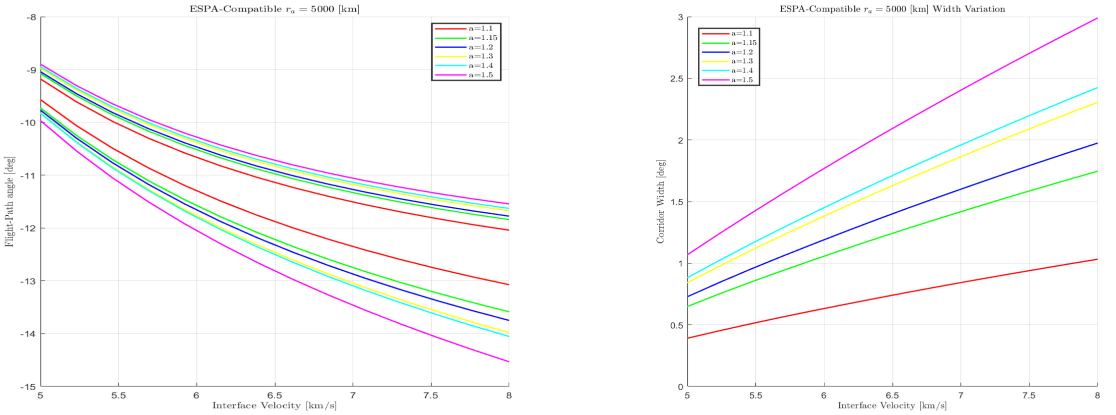

(a) ESPA-Compatible ‘a’ Corridor Variation.

(b) ESPA-Compatible ‘a’ Corridor Width.

Figure 3.9: Nominal Corridor Variation for ESPA Hyperbolic Coefficient Variation

3.4.2. Hyperbolic Parameter Variation Effect

The nominal corridor of the different capsule’s designs presented on section 3.3 has been computed. First, no knowledge of the trajectory feasibility is known; this variation has been performed with the expected worst-case scenario, ESPA-compatible capsules with maximum allowable spacecraft mass (maximum inertia case). Results reported on Figure 3.9 provide first valuable information about the problem.

Firstly, it can be guaranteed that the targeted aerocapture is feasible and can be accomplished without crashing against the planet. The other fact that can be noted is that the corridors’ shallow sides are displaced vertically upwards for increasing value of the vehicle’s hyperbolic parameter, shifting from $\gamma = -9.2[deg]$ at 5 [km/s] for a=1.1, to $\gamma = -8.8[deg]$ at a=1.5. This difference keeps increasing for increasing incoming velocity. This is an advantage, as higher loads are encountered for lower values of FPA, and when constraints are applied, deeper FPA angles will be prevented. Therefore, this will help to have wider corridors for constrained cases. Also, the overall corridor width is increased for the increasing ‘a’ value, which means a greater control authority that translates into a higher relaxation for the aerocapture’s guidance.

From these results, it can be concluded that the capsule’s hyperbolic contour increase proves to be advantageous on aerocapture by introducing two effects into the nominal corridor:

- Upward shift of the shallow side of the corridor.
- Increase on the nominals corridor width, by shifting downwards the deep side of the

corridor.

The main parameter varied on the capsule is the L/D ratio, proving to be advantageous on direct force method aerocapture having an increase on this figure of merit. As reported on Figure 3.9, the width is increased for greater values of velocity, differently from what happens on ballistic trajectories where the corridor remains almost constant. This effect is produced because of the increased aerodynamic power on the lift force with the value of the velocity squared.

3.4.3. ESPA-Grande and ESPA-Compatible Radius of Apoapsis Variation

As the hyperbolic contour parameter increment has been proven advantageous for aerocapture trajectory, ESPA-compatible capsules could potentially perform the manoeuvre (if the vehicle and trajectory constraints allow so). It is time to understand whether an increase in the size of the capsule supposes, if any, an advantage for the mission. By fixing in both cases the hyperbolic contour parameter *'a'* to 1.5, assuming maximum allowable masses respectively, and varying the mission scenario from high to lower values of target apoapsis, thi effect can be reproduced. The obtained results are reported on Figure 3.10.

The shallow side of the corridor is not much affected by the change in the target of apoapsis. On the contrary, the deep side of the corridor is heavily affected. For lower values of the targeted radius of apoapsis, the values of the flight path angle become more negative. This positively affects the corridor width when non-accounting restrictions on the trajectory. It shall be noted that for the high radius of apoapsis $r_a > 15000[km]$, and low interface velocities $v_{EI} < 6$, the width of the nominal corridor is lower than 1 degree, making the corridor too tight to be able to be used in the presence of uncertainty, and later will be shown with operational corridors that the feasible region for highly elliptical orbits is greatly squeezed when compared to lower ones.

The same trend is observed for ESPA-Grande compatible capsule designs, with the sole difference of having higher entry flight path angles. Hence, the increase obtained in the reference surface is capable of counteracting the effect of mass gain. Proving to be advantageous when compared to ESPA-Compatible capsules, as the expected loads to be encountered during the trajectory will be lower. It will potentially en-wider its feasible region Figure 3.11.

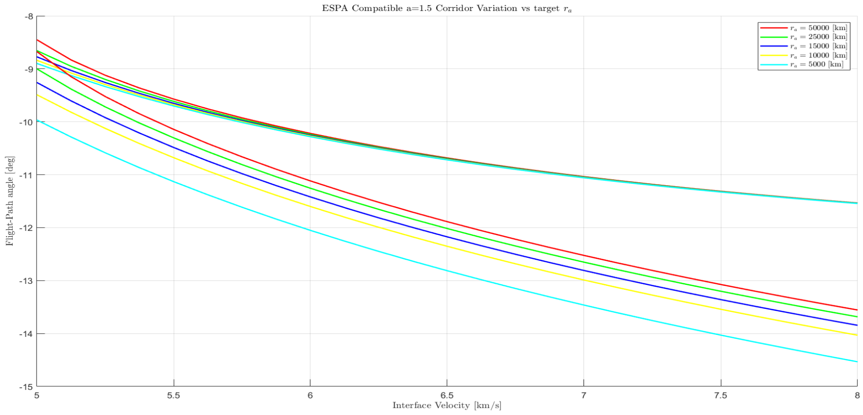

(a) ESPA-Compatible Corridor r_a variation.

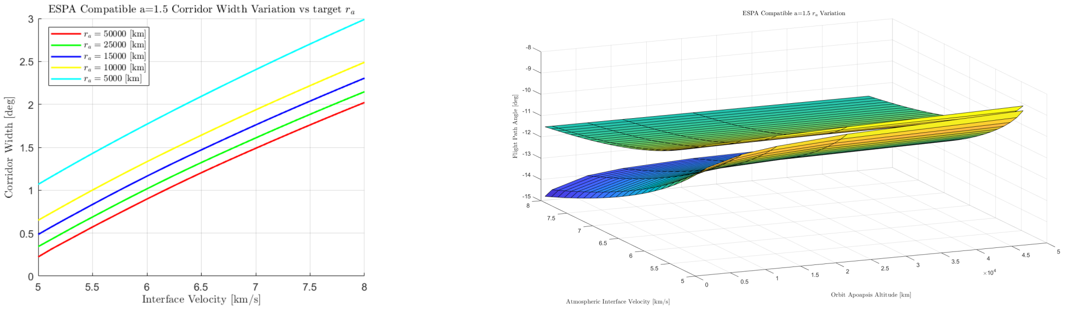

(b) ESPA-Compatible Corridor Width r_a variation.

(c) ESPA-Compatible r_a Corridor Variation Surface

Figure 3.10: Nominal Corridor Variation for ESPA and ESPA-Grande r_a Variation

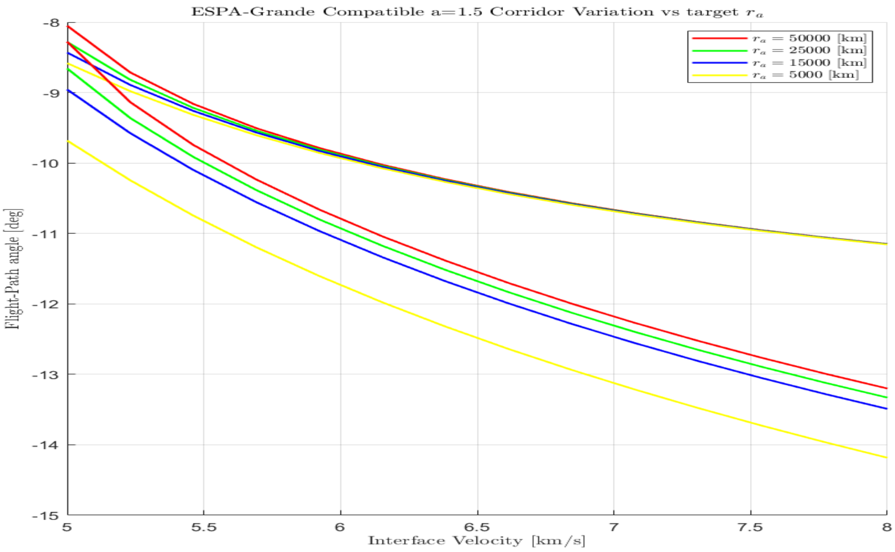

Figure 3.11: ESPA-Grande Corridor r_a variation

3.4.4. Mass Variation Effect

The mass variation effect has been studied for the ESPA-Compatible capsule with a hyperbolic contour parameter *'a'* of 1.5 and a fixed value of the radius of apoapsis equal to 5000 km. Obtained results are reported on Figure 3.12. The mass-increasing dominating effect pushes the corridor toward deeper trajectories, with a small reduction effect on the corridor's width 3.12b of about 0.2 [deg] across the whole range of trajectories. Hence, it can be stated that lower masses are preferred for aerocapture manoeuvre, following a similar argumentation as provided on the subsection 3.4.3.

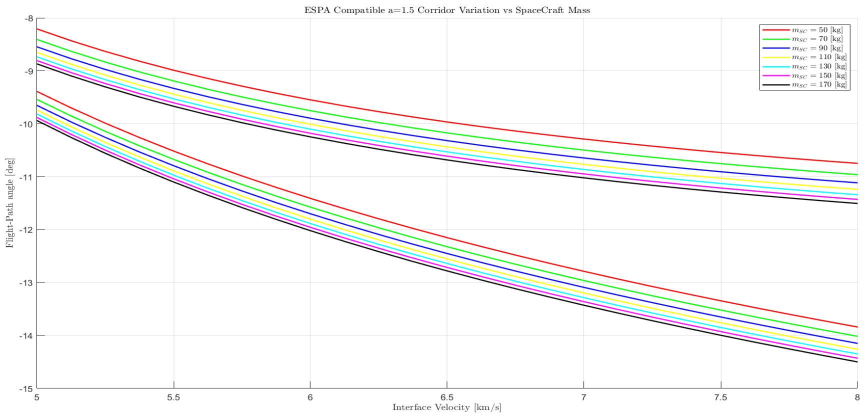

(a) ESPA-Compatible Corridor Mass variation.

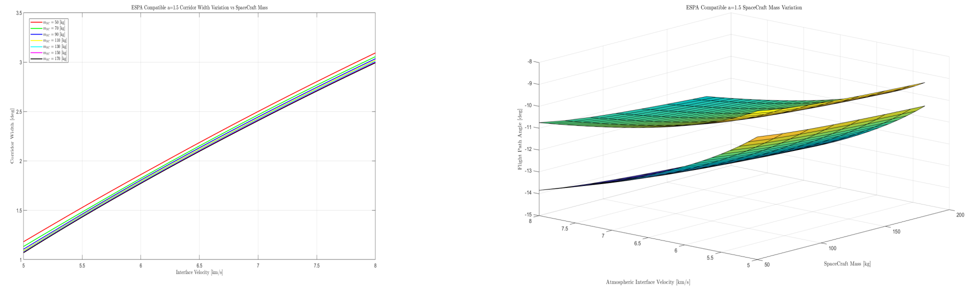

(b) ESPA-Compatible Corridor Width Mass variation.

(c) ESPA-Grande Corridor r_a variation.

Figure 3.12: Nominal Corridor for ESPA-Compatible Mass Variation

3.4.5. Entry Conditions Effect

The atmospheric entry states highly affect the shape of the corridor. In previous charts, only velocity has been modified, while the rest of the state variables have been maintained constant.

For example, considering a different entry interface radius would suppose a different energetic state of the spacecraft, implying a variation in its potential energy. Also, the variation of the heading angle would vary the behaviour of the corridor, as it is the angle formed by the projection of the velocity vector into the local-horizontal frame and the local north. It is determined by the kind of orbit aimed at a target (as $\psi = \frac{\pi}{2}$ means a parallel flight along the equator, and $\psi = 0$ would mean a polar orbit).

Hence, the corridor is not only influenced by the vehicle parameters but also by the atmospheric entry state and the point at which this is defined. For that reason, the most convenient approach is explicitly computing the corridor for the planned mission case while taking some of the previous design considerations for the mission design phase.

3.4.6. Summary of Nominal Corridor Conclusions

As already commented, some conclusions can already be drawn from the outcomes obtained on the nominal corridors. All in all, the following criteria can be extracted in a general trend. A lower ballistic coefficient provides shallower trajectories, displacing the corridor upwards. Three factors can decrease the ballistic coefficient:

1. Reduce the Vehicle's mass.
2. Increase the vehicle's Reference Surface.
3. Increase the vehicle's drag coefficient. (limited by aerodynamics).

The other main parameter related to the mission feasibility and the capability of the spacecraft to deal with trajectory uncertainty is the corridor width. The corridor width is more influenced by the L/D ratio of the vehicle, as shown from the capsule's parameter study. This fact goes against item 3. Because of the tight encountered corridors on Smallsat aeroshells at Mars, it would be preferable to opt for a greater L/D ratio while punishing trajectory loads, for which this kind of vehicle is better suited. The only free variable remaining for the mission designer would be making the spacecraft as lightweight as possible, to encounter milder heat and structural loads.

3.5. Test Mission Selections

From the gained knowledge on aerocapture's trends, and as it has feasible manoeuvre performance, some selections shall be made on spacecraft, entry state and target trajectories. This mission definition will address the feasible regions of the trajectories by applying safety factors to account for the uncertainty and trajectory's and vehicle's constraints.

3.5.1. Capsule Selection

ESPA-Compatible capsules are nearer to the Smallsat concept and are thus preferred, even if expected loads during aerocapture will be higher, leading to a more constrained feasible solution. Because no proper system design is performed, and the concept's flexibility wants to be tested, the maximum allowable mass by ESPA rings will be used.

Uncertainty-dealing measures and constraints will reduce the nominal corridor width. Suppose highly elliptical orbits, with high apoapsis radius, want to be targeted while maintaining enough corridor width. In that case, greater L/D ratio capsules are needed, and from reported on Figure 3.10, the only capsule obtaining a width corridor greater than 1 [deg] is *'a'* equal to 1.5, and thus selected, even if available volume inside is decreased. The selected capsule properties are summarised on Table 3.3.

Table 3.3: Test Mission Capsule's Properties

Property	Value
Compatibility	ESPA-Compatible
Hyperbolic Parameter	1.5
Mass	180 [kg]
S_{Ref}	0.31 [m^2]
$\alpha_{Max/Min}$-$\beta_{Max/Min}$	$\pm 20[deg]$

3.5.2. Operational Corridor and Feasible Region

The Operational Corridor follows the same conceptual approach as the Nominal Corridor. However, in this case, for the atmospheric density, the lower value for the shallow side and the higher value for the deep side coming from *'MarsGram 2010'* are considered. On top of these values, a level of safety margin is added to account for all the aerocapture's uncertainties, such as the day-of-flight variations, aerodynamic miss-modelling, winds, etc. This provides a more restricted corridor, with reduced corridor widths.

When the trajectory presented constraints subsection 3.2.4, the vehicle constraints, and the condition of minimum corridor width is applied to it, the aerocapture's feasible region is obtained.

As already commented, the corridor depends on the mission parameters, such as the target orbit, and on the atmospheric entry interface state. Hence, it has been decided to develop an engineering tool called *'Aerocapture-Designer'*. This tool will provide fast aerocapture design iteration and extraction of the aerocapture's feasible region, providing the active and most restrictive constraints from the designer introduced data. The developed engineering tool accounts for the following already implemented characteristics:

- Maximum Dynamic Pressure Constraint.
- Maximum Stagnation Point Heat Rate Constraint.
- Maximum Load Factor Constraint.
- Minimum Flight Altitude Constraint.
- Minimum Corridor Width Constraint.
- Variable Safety Factor to Account for Uncertainty.
- Feasibility Flag.
- Most Restrictive Constraint on the region indicator.
- Out-of-Plane manoeuvrability.

Mission-Designer Selections and Test

The vehicle constraints given in Table 3.2 are enforced along with the trajectory constraints subsection 3.2.4 on the *Aerocapture-Designer* tool. A minimum corridor width of 1 degree has been introduced to relax the guidance, and a 25% uncertainty margin has been introduced. The trajectory conditions are summarised on Table 3.4.

Table 3.4: Feasibility Test

Property	Value
Minimum Corridor Width	1[deg]
Minimum Altitude	26.6 [km]
$\dot{Q}_{Max}$	1 [kW/cm^2]
q_{∞}^{Max}	16 [kPa]
n_{Max}	13 [g]
Uncertainty Safety Factor (SF)	25%
Initial State (R)	$[r_0; 0; 0; V_{range}; \gamma; 0]$
r_0	$130 + R_m$ [km]
V_{range}	5-8 [km/s]

Two different apoapsis radii will be targeted, representing the two kinds of trajectories to be performed utilising aerocapture: a low circular orbit and a highly elliptical orbit for a later aerobraking manoeuvre. The selected radius of apoapsis to compute its feasible region from the previously presented definition are R_m+400 [km] and 33000[km], respectively.

On 3.13a, the low circular orbit's feasible region is reported. Low circular orbits are nicely suited to perform the aerocapture manoeuvre with aeroshell Smallsats, covering a wide range from 5 to 7.8 km/s. The most restrictive constraint corresponds to the maximum dynamic pressure and is active at 6.3 [km/s]. From 7.8 [km/s] and produced by the effect of the maximum dynamic pressure constraint, the trajectory is unfeasible due to the lack of enough corridor width.

For the case in which highly elliptical orbits are targeted, the feasible region is squeezed as reported on 3.13c. Not enough corridor width is obtained up to 6.74[km/s]. Then, as in the circular case, the dynamic pressure constraint is active and it is the most restrictive one. The corridor width is decreased up till turning unfeasible for 7.82 [km/s].

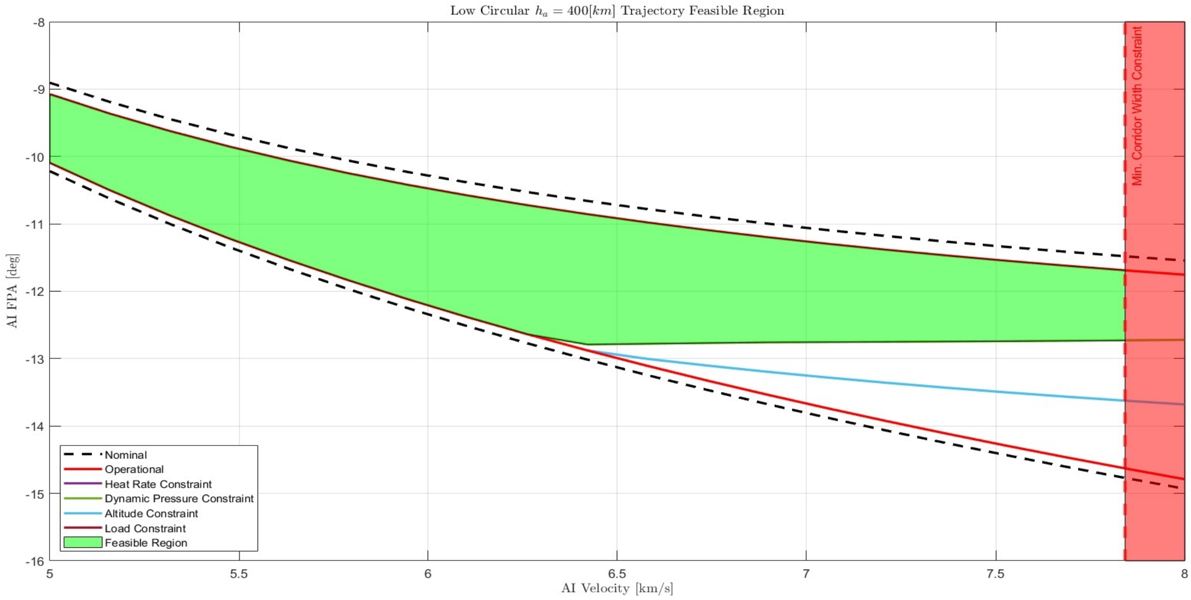

(a) In Plane Feasibility.

The out-of-plane capabilities have been analysed, looking for the worst cases of the deep and shallow corridors, with constant trimmed to the maximum capability of the side-slip angle reported on Table 3.4. The labelled *'Available'* region on 3.12d and 3.12b, would be the secure region to address during the mission design, as in any case could be achieved without any regard of the manoeuvres performed throughout the trajectory. The out-of-plane capabilities on the *'Available'* region are pretty limited and seem to be related because of the low reference surface issue commented on subsection 3.1.1.

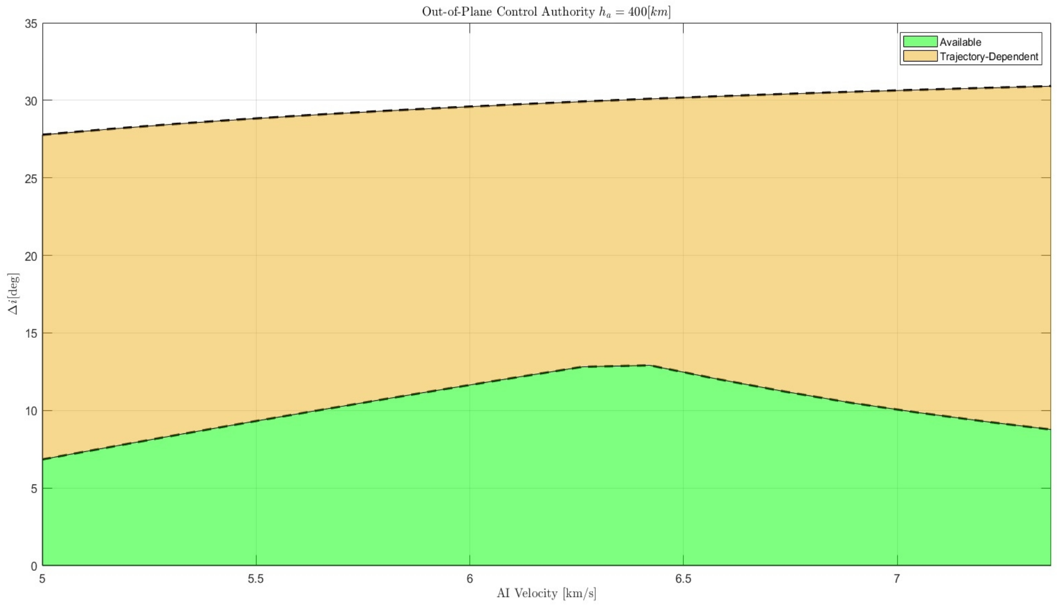

(b) Out-of-plane Feasibility.

Figure 3.12: Circular Target Orbit Feasibility $h_a = 400[km]$

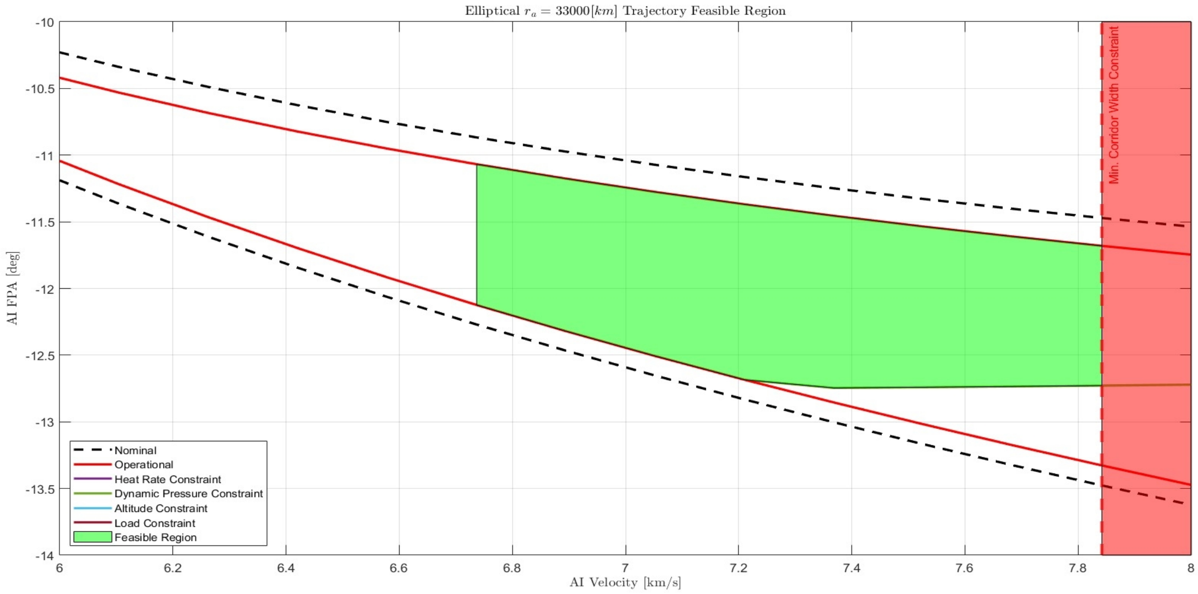

(c) In Plane Feasibility.

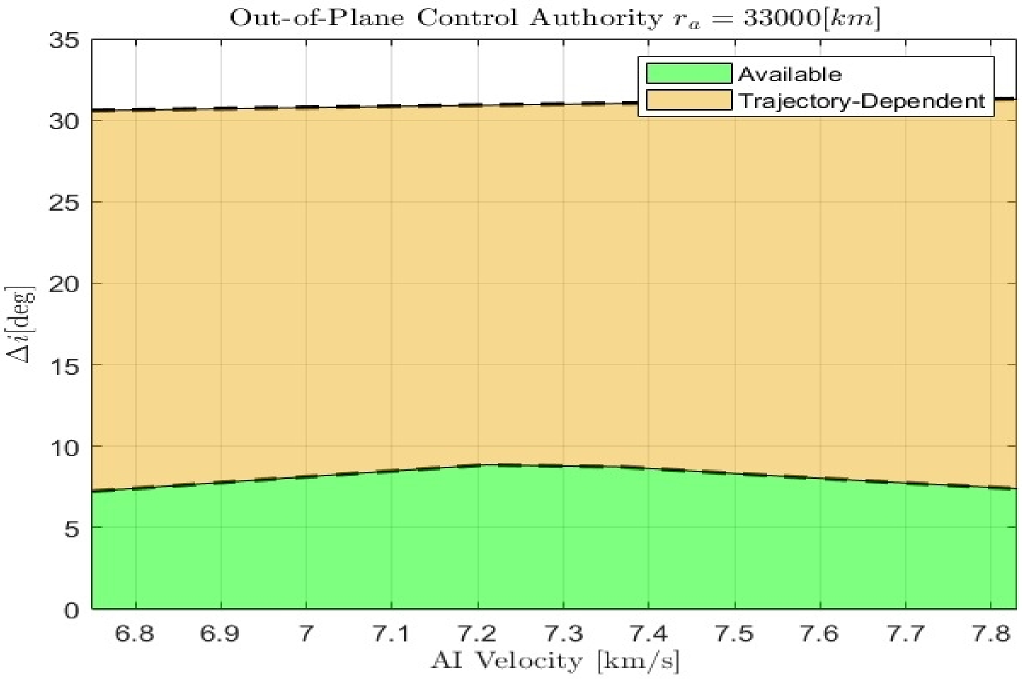

(d) Out-of-plane Feasibility.

Figure 3.12: Elliptical Target Orbit Feasibility $r_a = 33000[km]$

Conclusions

From obtained results, it can be concluded that aerocapture can be accomplished on Mars with aeroshell-kind vehicles of the small-sat class that could fit within secondary mission spots. The low circular orbits exhibit a broad feasible region, covering almost the whole entry velocity space, except for velocities higher than 7.8 [km/s]. The relaxation in the capsule's constraints compensates for the loss on the reference surface compared to HIADS and ADEPTS concepts.

On the other side, for elliptical target orbits, the feasible region is highly reduced. Elliptical orbits would only be feasible on the medium range of entry interface velocities, lower and higher ranges would be prevented. On this kind of target orbit, devices presenting reference surface incrementation devices, where ballistic trajectories are exploited, would present a better suit, as the only parameter determining the corridor width would be the ballistic coefficient ratio [22]. However, targeting elliptical orbit with aeroshell technology could result in comparative advantage. As for the post-atmospheric aerobraking manoeuvres, the spacecraft could dive deeper into the atmosphere to achieve in a shorter period the desired orbit. This effect could mitigate one of the main risks the aerobraking manoeuvre implies (long time duration and operation intensive manoeuvre), and allow its use even when the high time delays make the mission application unfeasible. This could be done, as in DFC, the heat-shield is not jettisoned during aerocapture, and could be later re-used on the aerobraking manoeuvre.

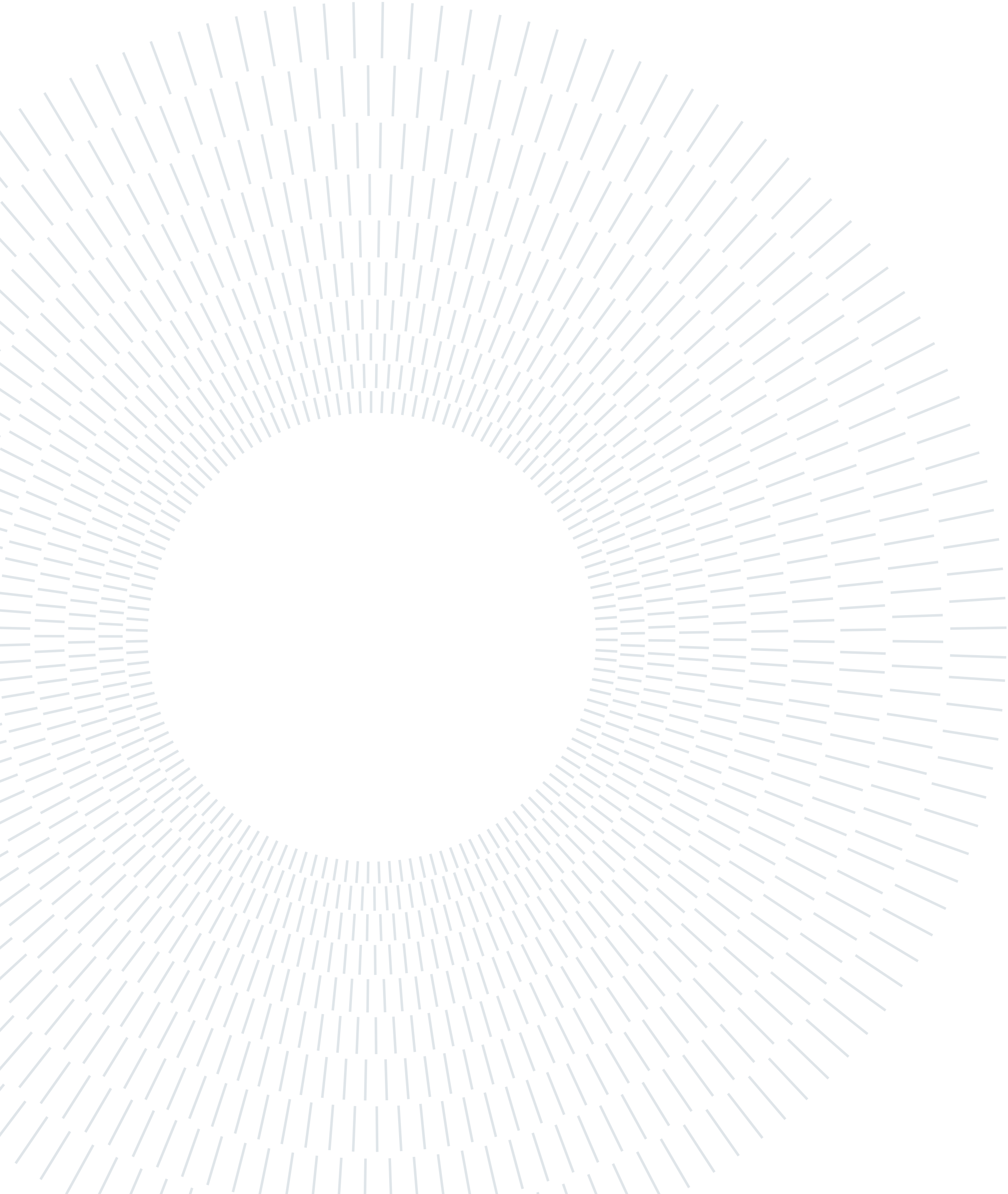

4 | Guidance

In this chapter, two main things will be addressed. The optimal control problem will be presented and solved for different objective functionals. Then, optimal control is implemented in the online guidance to mimic the optimal control structure while seeking robustness when exposed to a stochastic environment.

4.1. Optimal Control Problem

An optimality-based guidance design is developed in this thesis. The optimal control structure must be known to solve the optimisation on the appropriate control search space. In a deterministic setting, the open-loop optimal control problem is therefore solved. Two main figures of merit will be essential to account for in the aerocapture optimisation problem and are related to the volume and mass occupied on the spacecraft required for the manoeuvre. Aerocapture looks to increase the usable mass fraction by eliminating the capture propulsive burn. However, aerocapture introduces other requirements into the spacecraft: implementing a heat shield and exo-atmospheric manoeuvre to raise periapsis and orbit correction.

On the one hand, [39] demonstrated that apoapsis targeting and ΔV minimisation were not always linked and are conditional to the target orbit. Looking in the optimal search space after solving the optimal control problem was proved [44] to improve the guidance results significantly. On the other hand, reducing the exo-atmospheric cost manoeuvre at the expense of introducing a total heat penalty, which implies the increment of the heat shield's mass and volume, can be argued not to be the best strategy to be chosen. Both terms should be considered and sized to select the strategy that minimises the overall result—providing the most advantageous one for the aerocapture design, where most of the volume and mass fraction can be retrieved to the mission's payload.

4.1.1. Problem Statement

The general optimal aerocapture problem can be stated as follows:

$$\min J = \Phi(\boldsymbol{x}(t_f)) + \frac{1}{w}\int_{t_0}^{t_f} L(\boldsymbol{x}(t))dt \tag{4.1}$$

$$s.t. \quad \dot{\boldsymbol{x}} = \boldsymbol{f}(\boldsymbol{x}(t), \boldsymbol{u}(t), t) \tag{4.2}$$

$$\boldsymbol{x}(t_0) = \boldsymbol{x_0} \tag{4.3}$$

$$\boldsymbol{u} \in \{\boldsymbol{u_{min}}, \boldsymbol{u_{max}}\} \tag{4.4}$$

$$t_f \vee free \tag{4.5}$$

The manoeuvring cost can be calculated using Equation 4.6-Equation 4.9 [25][12], where the out-of-plane is only valid for circular orbits and assuming Keplerian motion following the atmospheric pass. With Equation 3.7, the apoapsis radius is computed. For the computation of the inclination Equation 4.10 [12] is provided, where ψ_I is computed using Equation 3.8.

$$\Phi(\boldsymbol{x}(t_f)) = |\Delta V_1| + |\Delta V_2| + |\Delta V_3| \tag{4.6}$$

$$|\Delta V_1| = \sqrt{2\mu}\left(\left|\sqrt{\frac{1}{r_a} - \frac{1}{r_a + r_p^*}} - \sqrt{\frac{1}{r_a} - \frac{1}{2a}}\right|\right) \tag{4.7}$$

$$|\Delta V_2| = \sqrt{2\mu}\left(\left|\sqrt{\frac{1}{r_p^*} - \frac{1}{r_a^* + r_p^*}} - \sqrt{\frac{1}{r_p^*} - \frac{1}{r_a + r_p^*}}\right|\right) \tag{4.8}$$

$$|\Delta V_3| = 2\sqrt{\frac{\mu}{r_a^*}}\left(\frac{|i - i^*|}{2}\right) \tag{4.9}$$

$$\cos i = \cos\phi \cos\psi_I \tag{4.10}$$

For the term inside the path cost, it is expected that the radiative heat during the aerocapture on Mars is small when compared to the convective heat load. Consequently, on [84], only convective heating was used *'because no strong radiators appear in the chemical makeup of the dissociated Mars gases'*. The aeroheating model is reported in section 2.4, and the relation for the convective heat rate is reported on Equation 2.22, leading to the lagrangian provided in Equation 4.11, where the density has considered only to be a function of the radius by the use of the exponential model presented in subsection 2.3.1.

$$L(\boldsymbol{x}(t)) = \dot{Q}_{Conv.}(r(t), V(t), R_N) \tag{4.11}$$

The control variables when DFC is applied in aerocapture are given in Equation 4.12. The α will take charge of controlling the longitudinal channel, while the β, the lateral one.

$$\boldsymbol{u} = \begin{bmatrix} \alpha(t) \\ \beta(t) \end{bmatrix} \tag{4.12}$$

Assumptions The following simplifications have accounted for the optimal control resolution. Firstly, the planet's rotation has been discarded, and the spherical gravity model is employed, leading to $\boldsymbol{x}_R \approx \boldsymbol{x}_I$, and simpler equations of motion. If $\sigma = 0$, $c_L(\alpha)$, $c_D(\alpha)$, and $c_Q(\beta)$ are assumed, the lateral and longitudinal channel can be considered to be completely decoupled. Consequently, the optimal control problem could be decoupled into two smaller sub-problems and solved separately. This strategy has been followed in the present work.

The resolution of the longitudinal channel will drive the flight altitude and velocity and, as a result, will be mainly related to the heat rate. Hence, the corresponding objective function will be ΔV_1, ΔV_2 and $\dot{Q}_{conv.}$. Conversely, the lateral channel will focus on the out-of-plane ΔV_3 minimisation with β as the unique control variable and assuming the α^* is already obtained from the longitudinal channel resolution.

4.1.2. Longitudinal Channel Resolution

The objective function of the longitudinal sub-problem is given from Equation 4.13 to Equation 4.18. As a bounded control problem exists, the *Pontryagin's Minimum Principle* is applied to obtain the optimal control strategy. The Hamiltonian of the problem is reported on Equation 4.19, and Pontryagin's Minimum Principle application is provided in Equation 4.20. As stated in [48]:

"For example, let's consider when λ_v^*<0 and $\lambda_\gamma^* > 0$. In this case, the two terms have the same sign. Therefore, we desire a configuration that minimises the drag force while producing the most negative vertical lift force. Intuitively, this leads us to choose α_{Max}. Now consider when λ_v^*>0 and $\lambda_\gamma^* > 0$. The two terms now have opposite signs, and there is no way to apply intuition to select a value of α. So, in general, the optimal angle of attack profile is not a bang-bang solution like we found for bank angle. Because both the lift and drag are functions of angle of attack, the optimal profile will at times require

intermediate values of angle of attack."

$$
\begin{aligned}
\min J_1 = |\Delta V_1| + |\Delta V_2| + \frac{1}{w}\int_{t_0}^{t_f} \dot{Q}_{Conv.} dt && (4.13)\\
s.t. \quad \dot{r} = v\sin\gamma, \quad r(t_0) = r_0 && (4.14)\\
\dot{v} = -\frac{D(\alpha)}{m} - \frac{\mu\sin\gamma}{r^2}, \quad v(t_0) = v_0 && (4.15)\\
\dot{\gamma} = \frac{1}{v}\left(\frac{L(\alpha)}{m} + \left(v^2 - \frac{\mu}{r}\right)\frac{\gamma}{r}\right), \quad \gamma(t_0) = \gamma_0 && (4.16)\\
\alpha_{Min} \leq \alpha \leq \alpha_{Max} && (4.17)\\
tf \vee free && (4.18)
\end{aligned}
$$

$$
H = \dot{Q}_{Conv.} + \lambda_r v\sin\gamma + \lambda_v\left(-\frac{D(\alpha)}{m} - \frac{\mu\sin\gamma}{r^2}\right) + \lambda_v\left(\frac{1}{v}\left(\frac{L(\alpha)}{m} + \left(v^2 - \frac{\mu}{r}\right)\frac{\gamma}{r}\right)\right) \tag{4.19}
$$

$$
\begin{aligned}
H(\boldsymbol{x}^*, \alpha^*, \boldsymbol{\lambda}^*, t) \leq H(\boldsymbol{x}^*, \alpha, \boldsymbol{\lambda}^*, t)\\
\therefore \lambda_v^* D(\alpha^*) + \lambda_\gamma^* \frac{L(\alpha^*)}{v^*} \leq \lambda_v^* D(\alpha) + \lambda_\gamma^* \frac{L(\alpha)}{v^*}
\end{aligned} \tag{4.20}
$$

Hence, the problem must be solved numerically. Two types of resolutions can be applied, indirect and direct methods. The former would apply the *Euler-Lagrange* necessary and sufficient conditions for the optimality, mainly by introducing a regularisation function and solving the corresponding boundary value problem through numerical methods, such as collocation like, suggested in UTM [46]. Their main advantage is that it will provide a more accurate solution while reducing the region of convergence, requiring a better initialisation when compared to direct methods, and also requiring the initialisation of the co-states.

The latter would transform the OCP into an NLP by discretising the trajectory. Within the direct methods, different resolution kinds do exist, such as direct shooting and collocation (transcription) methods. According to the approach selected, different trade-offs are faced. For example, in direct shooting, the implementation of path constraints is complex since the intermediate state variables are not inside the decision variables, with the advantage of reducing the number of them for the solver. A good approach would be exploiting the increased convergence space of the direct methods to initialise the resolution of the indirect method, which would provide a more accurate solution.

In this research, the collocation method has been used to solve the longitudinal optimal control problem. This selection has been performed as some constraints will be added to the problem to ease the solver's convergence, which was not present in the general formulation. Introduced constraints are reported on Equation 4.21.

$$\begin{cases} r(t_f) = 150 + R_m[km] \\ r(t) \geq R_m \end{cases} \tag{4.21}$$

From Equation 4.7 and Equation 4.8, absolute values are present within the objective function. The absolute value presents a discontinuity on its first derivative, introducing numerical issues for the gradient-based solvers. Therefore, the *abs()* functions in the objective functions have been replaced by a smooth approximation given in Equation 4.22, and graphically reported on Figure 4.1.

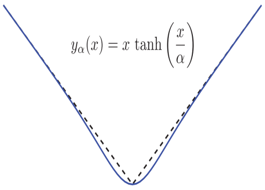

Figure 4.1: Smoothing [37]

$$y_{\alpha_s}(x) = x \tanh\left(\frac{x}{\alpha_s}\right) \approx |x| \tag{4.22}$$

The smooth parameter α_s is adjusted, as the lower its value, the closer the smoothened function will be to the real function, at the cost of an increase in the resolution difficulty of the NLP. The main drawback of this approach is modifying the optimisation problem in sometimes non-obvious ways. Hence, convergence tests are required, where this value is decreased until the solution is not further improved [72]. Adjusting the smoothing function and normalising the objective functions for the weighted problem to understand and prevent the ΔV and Heat-rate dominated regions.

For the transcription problem to pass from a continuous-time problem statement into a nonlinear program, the open-source trajectory optimisation software *'TrajOpt'*[37] has been used. Direct collocation has been exploited using the *Trapezoid Method*, as from [25], a near bang-bang structure was obtained for a different scenario case. So, the linear spline for interpolating the control, reported on Figure 4.2 was expected to provide a good representation of the angle of attack profile.

The problem initialisation was performed by solving the *'zero finding'* problem that would lead to the aimed radius of apoapsis targeting and providing the trajectory as the initial guess. Then a two-phase sequential resolution was made. A first rougher direct collocation

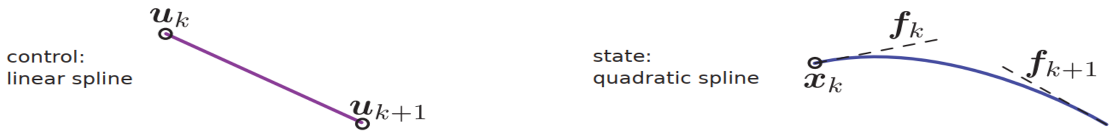

Figure 4.2: Splines used in Trapezoidal Method for Control and State approximation [37]

Table 4.1: Initial Conditions and Target for Longitudinal Optimization

Property	Value
h_0	130 [km]
v_0	6.1 [km/s]
γ_0	-12 [deg]
r_a^*	400 + R_m [km]
r_p^*	400 + R_m [km]

problem, consisting of 25 collocation points, is solved. Then, the obtained result is used to initialise a finer collocation problem consisting of 60 collocation points. The nonlinear programming software used is the built-in Matlab's *'fmincon'* function, a gradient-based optimisation tool, using the *'Interior Point'* algorithm.

The error analysis of the transcription process is quantified employing the correctness of how well the provided interpolation trajectory satisfies the dynamics Equation 4.23. To compute the state error, the integral along the spline can be computed as reported on Equation 4.24. The initial conditions and the target orbit are reported on Table 4.1.

$$\epsilon(t) = \dot{\boldsymbol{x}}(t) - \boldsymbol{f}(t, \boldsymbol{x}(t), \boldsymbol{u}(t)) \tag{4.23}$$

$$\eta_k = \int_{t_k}^{t_{k+1}} |\epsilon(\tau)| \, d\tau \tag{4.24}$$

ΔV Optimal

Firstly, the ΔV optimisation problem has been solved for two main reasons. The resolution has been conducted to perform the convergence analysis on the smoothening factor. The factor has been consecutively decreased up till the point where its reduction did not imply a change in the optimisation result. The value to be introduced on the hyperbolic tangent smoothening has been found to be $\alpha_s = 1e - 7$.

The obtained result is essential to perform normalisation on the weighted problem to

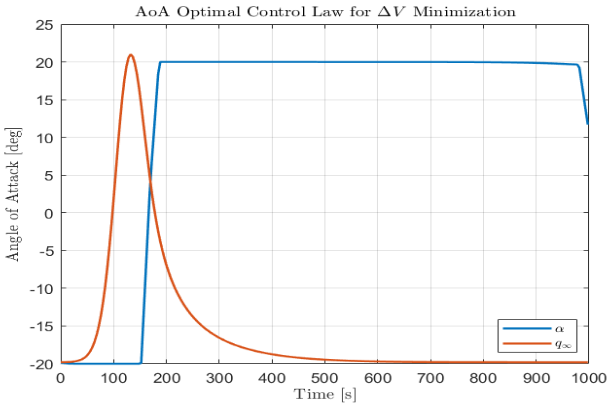

(a) ΔV Optimal Control.

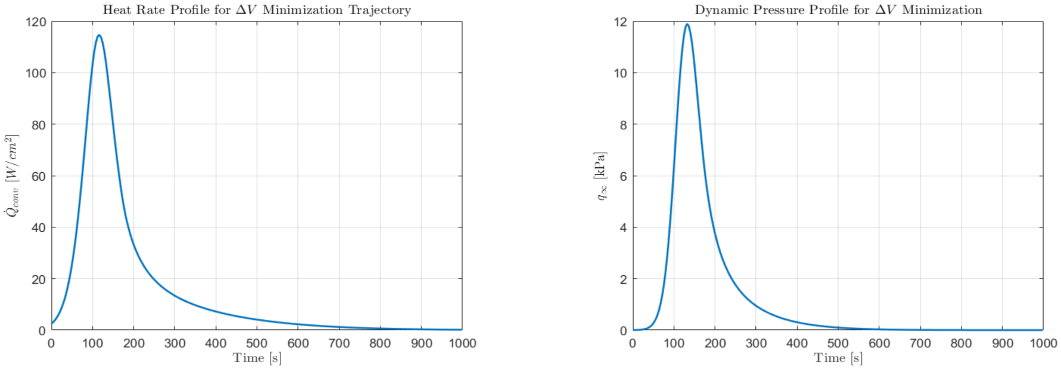

(b) ΔV Convective Heat Rate.

(c) ΔV Dynamic Pressure.

Figure 4.3: Results of ΔV Optimization

get the value close to unity near the optimal range. Obtained results are provided on Figure 4.3. From 4.3a, a near bang-bang full lift-up to full lift-down is obtained. These results are almost identical to the control strategy found by [25] for direct force control applied to Mars in a different mission set. Obtained results confirm this to be the same strategy for ΔV optimisation in this study's mission case. A scaled plot of the dynamic pressure is reported to understand the control authority region. Hence, the values of the control for values greater than 600 seconds would not influence the trajectory. On 4.3b and 4.3c, the heat rate and dynamic pressure are reported, and both demonstrate to be well within the vehicle constraints presented on chapter 3. Trajectory results are listed on Table 4.2, sorting the maximum values of the main figures of merit for aerocapture manoeuvre.

To estimate the error on the transcription problem used for the resolution, Equation 4.23 and Equation 4.24 are employed to compute the errors in the dynamics and on the state variables, respectively. The results are reported on Figure 4.4. Obtained values are small, within some meters on the radius. The resolution could be improved by reducing the

Table 4.2: ΔV Optimal Trajectory Results

Parameter	Value
ΔV_{Tot}	88.3 [m/s]
ΔV_1	$5.14 \cdot 10^{-7}$ [m/s]
ΔV_2	88.3 [m/s]
q_∞^{Max}	11.8 [kPa]
$Q_{Conv.}$	15.67 [kJ/cm^2]
$\dot{Q}_{Conv.}$	114.68 [W/cm^2]

mesh in direct methods or increasing the polynomial order, as in orthogonal collocation. Another good strategy would be to employ indirect methods, using as initialisation here obtained solution. However, these results could be considered already to be accurate, and the control strategy is well-defined. So, no further investigations are needed for this research. Higher fidelity resolutions would be suggested if results were required to train an artificial intelligence algorithm guidance.

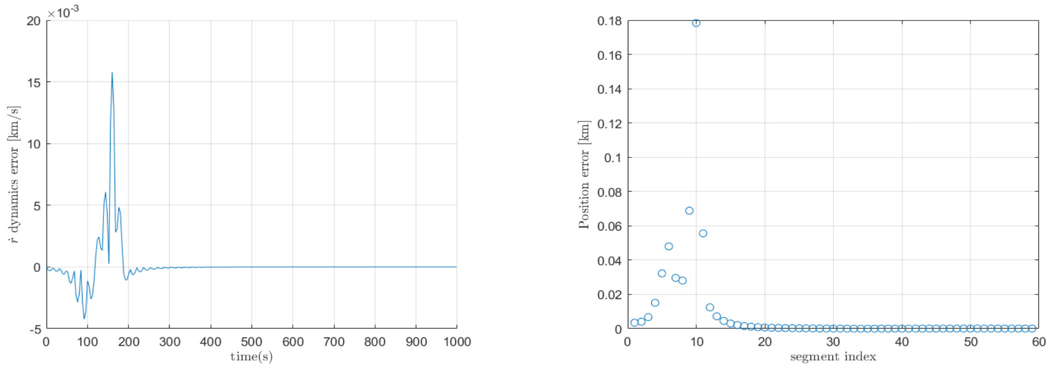

(a) ΔV position dynamics' error.

(b) ΔV position error.

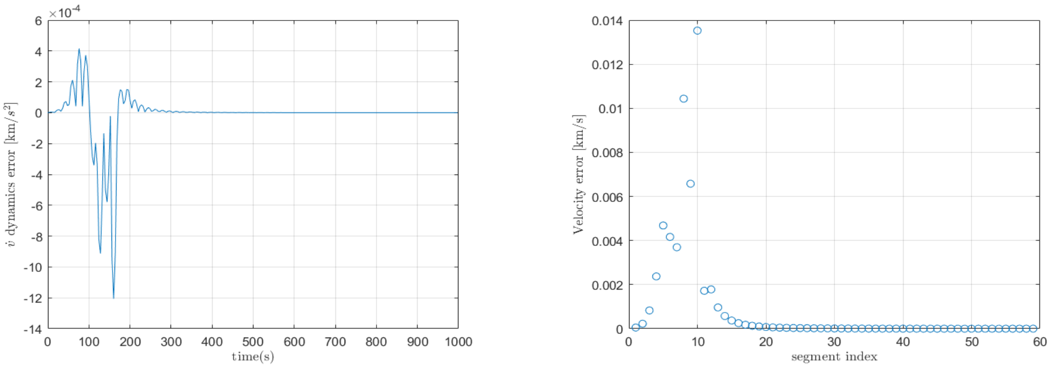

(c) ΔV velocity dynamics' error.

(d) ΔV velocity error.

Figure 4.4: ΔV Optimization Error Estimation

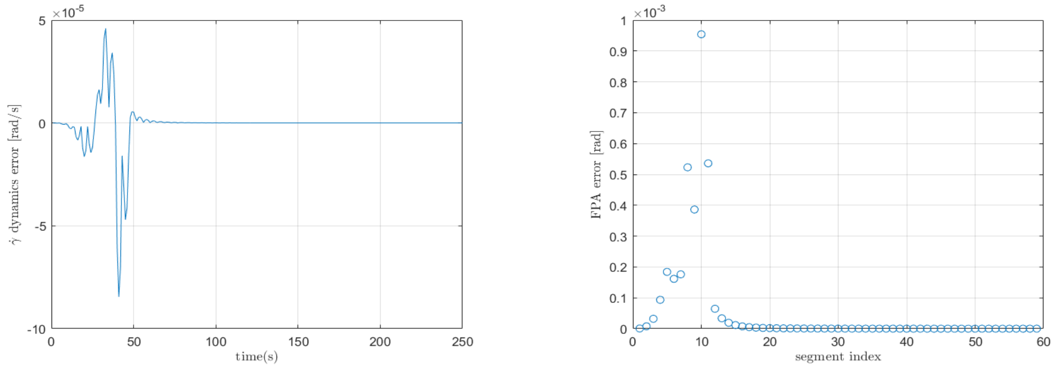

(e) ΔV FPA dynamics' error.

(f) ΔV FPA error.

Figure 4.4: ΔV Optimization Error Estimation

Total Heat Optimal

Secondly, the total heat optimal trajectory is solved. To the best of the writer's knowledge, no other studies have been conducted in this regard for the direct force control on aerocapture trajectory, but only for bank angle modulation. An analogous scheme to the resolution of the subsubsection 4.1.2 has been employed. The result will also be used for the normalisation of the weighted problem.

Obtained optimal control strategy is reported on 4.5g, and follows an almost inverse law compared to fuel optimal trajectory. It can be noted from 4.5h that the maximum heat rate is slightly increased compared to the past case. The overall integral minimisation is obtained by reducing the trajectory's time of flight and reducing the total heat at an increase in the maximum heat rate and dynamic pressure. The Table 4.3 resumed the central figures of merit of the trajectory, where a significant reduction of about 3 kJ/cm^2 on the total heat is obtained. Similar results from the error analysis to the ΔV optimal trajectory are obtained and are reported on Figure 4.6.

Table 4.3: Q_{Conv} Optimal Trajectory Results

Parameter	Value
ΔV_{Tot}	358.10 [m/s]
ΔV_1	51.30 [m/s]
ΔV_2	306.80 [m/s]
q_∞^{Max}	16.40 [kPa]
$Q_{Conv.}$	12.61 [kJ/cm^2]
$\dot{Q}_{Conv.}$	119.60 [W/cm^2]

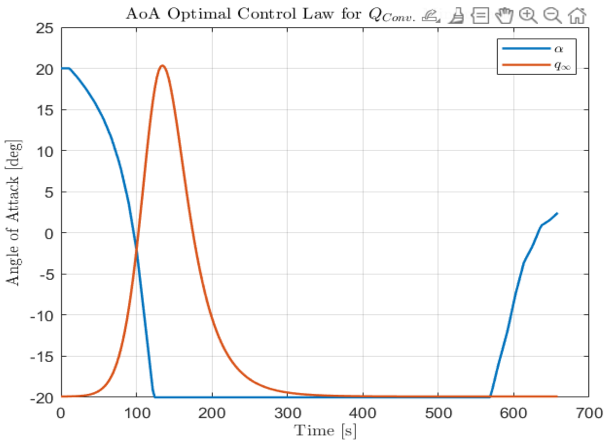

(g) Total Heat Optimal Control.

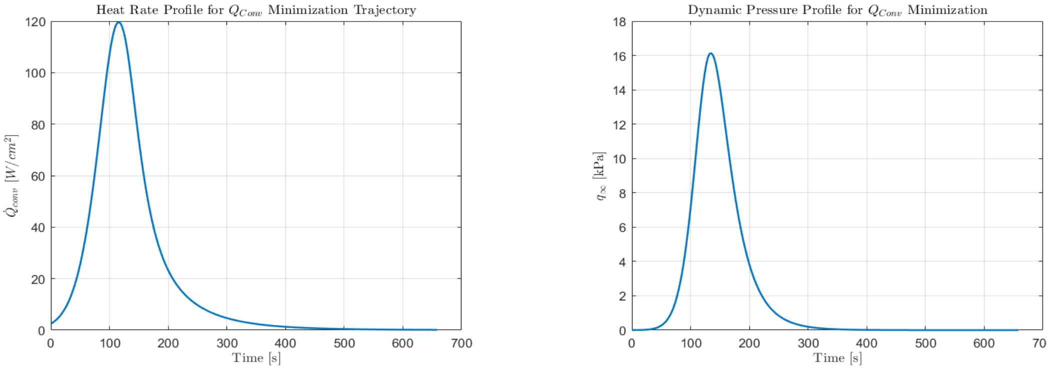

(h) Total Heat Convective Heat Rate.

(i) Total Heat Dynamic Pressure.

Figure 4.5: Results of Total Convective Heat Optimization

4.1.3. Weighted Optimal

The weighted optimal control is computed from the objective function reported on Equation 4.25. The optimal values are used to eliminate the dimensions and come to the unity of the values on both terms. Hence, none of the objectives will be privileged for the weight equal to unity. The weight value has been studied, ranging from 0.5, where optimisation is privileging the total heat figure, to 1.5, where manoeuvring cost is privileged. The results are depicted on Figure 4.7, and it can be appreciated how the higher the weight values, the nearer the solution to the ΔV optimal. The error estimation of the collocation is reported on Figure 4.7, and no significant differences concerning previous cases are obtained.

To correctly address the most promising trajectory strategy on the aerocapture manoeuvre, the volume and mass sizing corresponding to the implied subsystems shall be looked at. Since the propulsive subsystem and the heat shield, mass and volume are the main

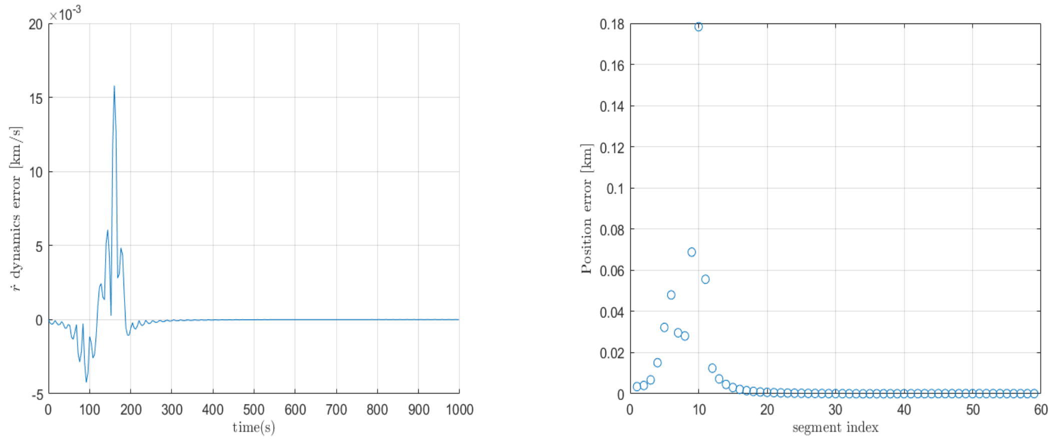

(a) Total Heat position dynamics' error. (b) Total Heat position error.

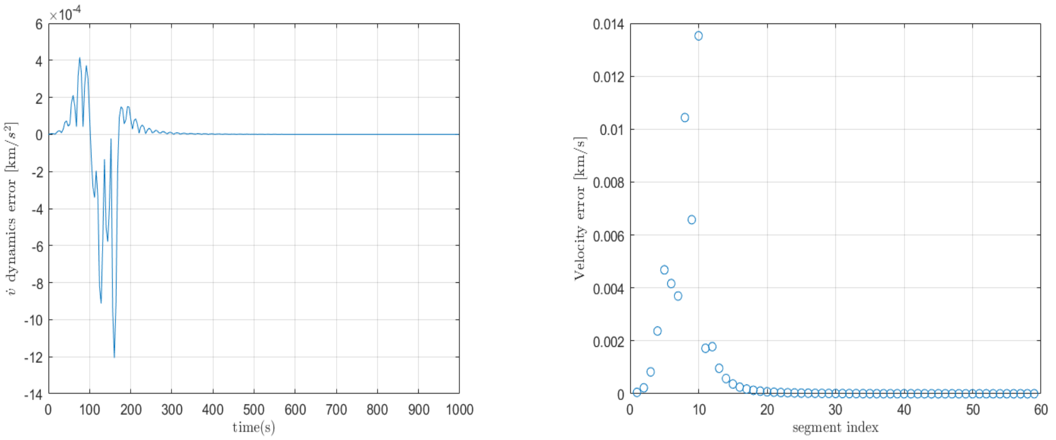

(c) Total Heat velocity dynamics' error. (d) Total Heat velocity error.

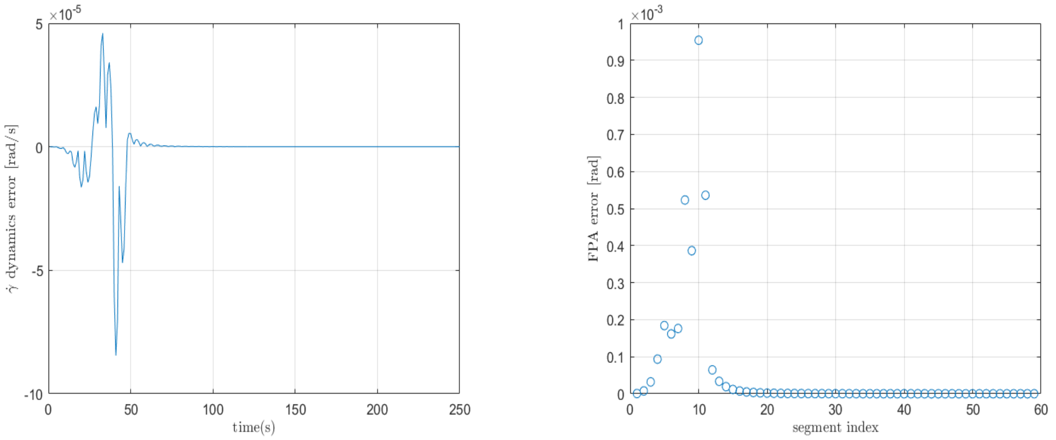

(e) Total Heat FPA dynamics' error. (f) Total Heat FPA error.

Figure 4.6: Total Convective Heat Optimization Error Estimation

penalties of the trajectory.

$$J_w = \left(\frac{\Delta V(\boldsymbol{x}(t_f))}{\Delta V_{opt.}}\right) + \frac{1}{w}\left(\frac{\int_{t_0}^{t_f} \dot{Q}_{Conv.}(\boldsymbol{x}(t))dt}{Q_{opt.}}\right) \tag{4.25}$$

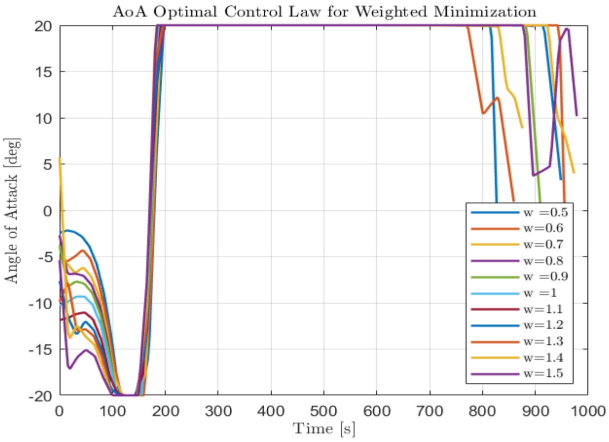

(a) Weighted Optimal Control.

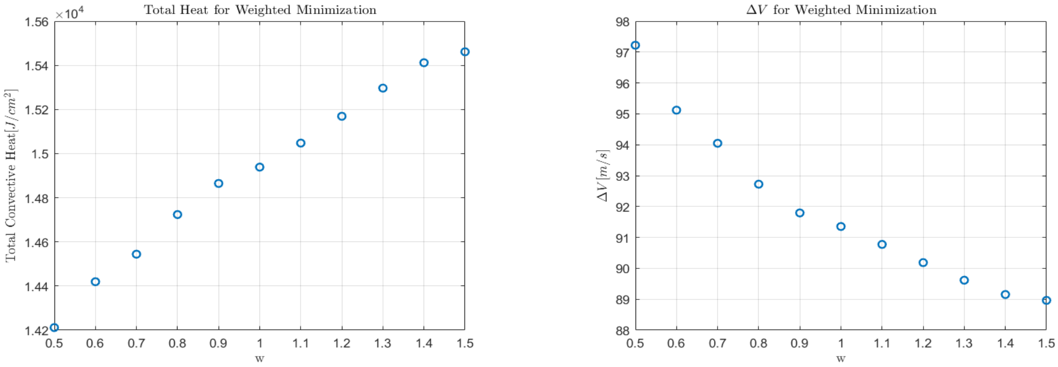

(b) Weighted Total Heat. (c) Weighted Total ΔV.

Figure 4.7: Results of Weighted Optimization

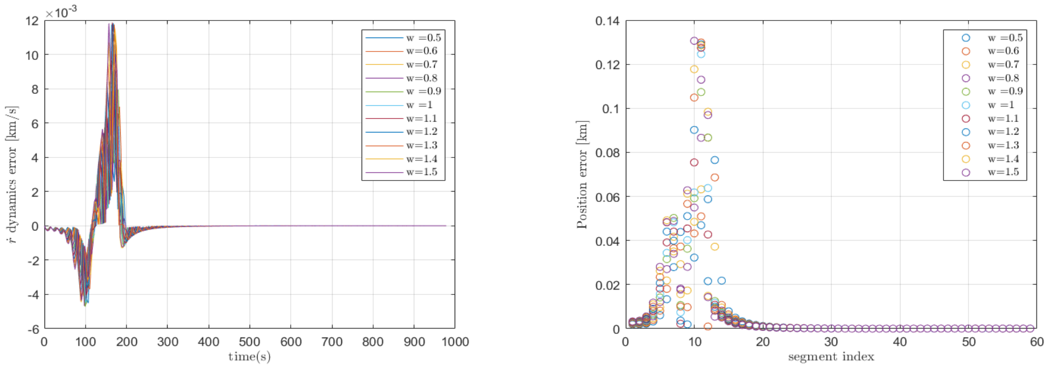

(a) Weighted position dynamics' error. (b) Weighted position error.

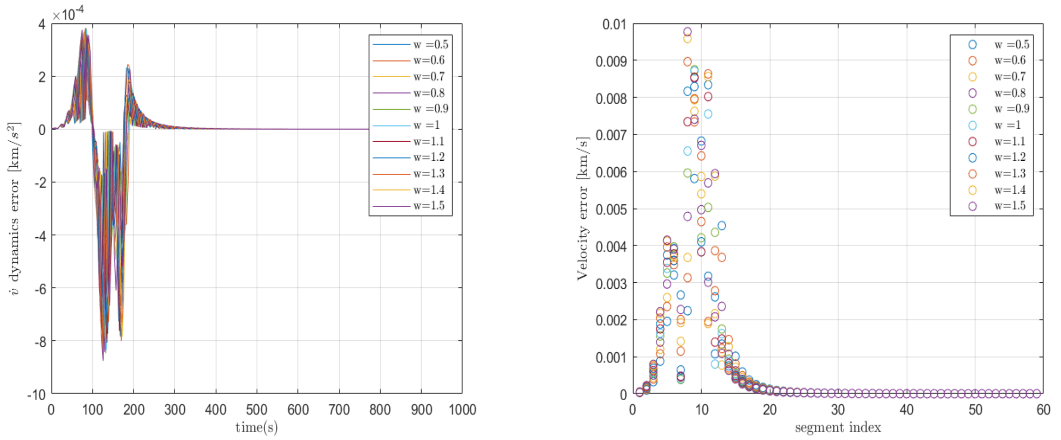

(c) Weighted velocity dynamics' error.

(d) Weighted velocity error.

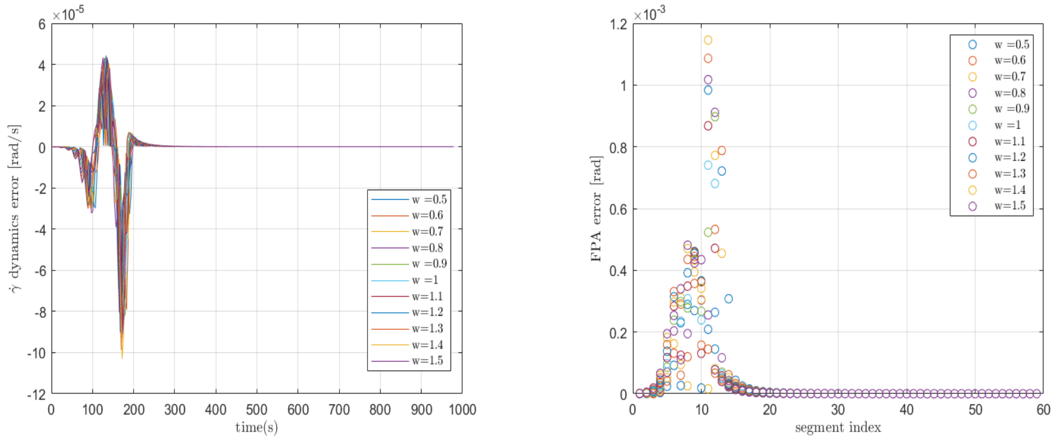

(e) Weighted FPA dynamics' error.

(f) Weighted FPA error.

Figure 4.7: Weighted Optimization Error Estimation

For the sizing of the TPS, a simplified correlation given in Equation 4.26[66] is used for the *'Pica'* aeroshell thickness computation. This correlation is based on Earth's re-entry trajectories. Since the Earth has a denser atmosphere, higher heat loads are encountered, so a conservative value can be assumed sufficient for a preliminary estimate, this thickness is later multiplied by the capsule's reference surface to get an estimation of the aeroshell volume. Then considering a density for the ablative thermal protection of 0.27 $[g/cm^3]$ [75], the mass is obtained.

$$t_{TPS} = 1.868 \left(\frac{Q_{Conv.}}{v_{EI}^2} \right)^{0.1879} \tag{4.26}$$

For the sizing of the propulsion subsystem, the rocket equation has been used to compute

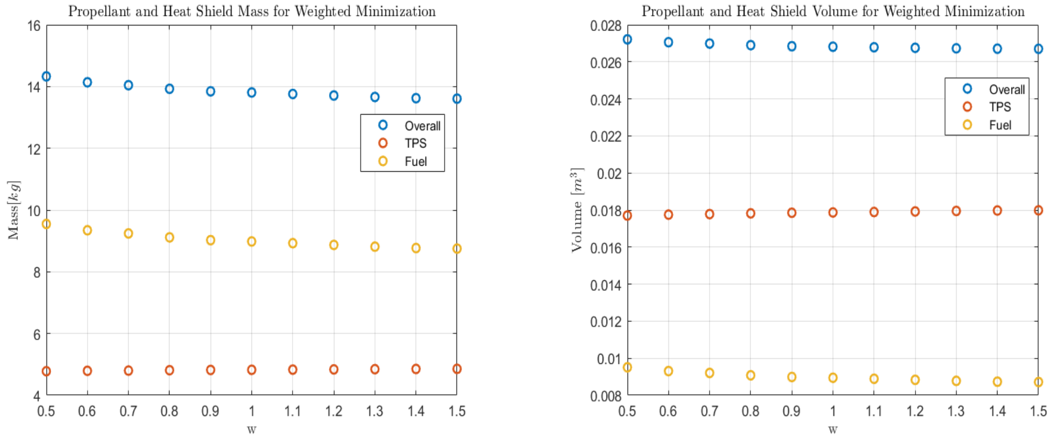

(g) Overall Mass Sizing.

(h) Volume Sizing.

Figure 4.8: Propulsion and TPS Sizing for trajectory selection

the mass of the propellant necessary to produce the required ΔV of each trajectory, reported on section 2.7. The propellant considered has been hydrazine, with a specific impulse of 230 seconds [52]. Only the variation in the propellant mass has been considered, as no change in the thruster is expected for the different trajectories. However, the presence of the tank shall be accounted for and will depend on the amount of propellant to be used. Therefore, a safety factor of 25 % has been applied to the propulsion mass to get a conservative estimate.

The sizing results for the mass and volume are reported on Figure 4.8. There is no significant difference in the mass or volume for the different strategies. In extreme cases, it leads to variations of around some hundred grams in mass. As a result, it can be concluded that the selection of the optimal control strategy is not mainly driven by none of the objective functions but by the ease of implementation of the online guidance. The ΔV strategy has been selected for its implementation in this work. It would provide some advantages on the online guidance implementation, which will be introduced later in the chapter.

4.1.4. Lateral Channel Resolution

For the resolution of the out-of-plane, and considering Equation 4.9, it can be established that minimizing the out-of-plane ΔV in the case of circular orbits, is equivalent to reducing the error in inclination between the target and the actual trajectory Equation 4.27.

$$\min J_2 = c\,|i^* - i(t_f)| \Leftrightarrow \min J_3 = |i^* - i(t_f)| \tag{4.27}$$

Therefore, the out-of-plane optimal control problem can be rewritten Equation 4.28-Equation 4.36. As the optimal control is obtained from subsection 4.1.2, and it is assumed decoupled from the lateral channel, the resolution accounts for α^* as a parameter of the problem and not as a decision variable. Hence, only β^* will be looked for during this resolution. A linear control model will be used on the side-slip angle during this resolution, using the 1-D model provided in subsection 2.1.5. Remember that these sets of equations present singularities on $\phi = \gamma = \pi/2$, as this fact will be exploited during the demonstration.

$$\min J_3 = |i^* - i(t_f)| \tag{4.28}$$

$$s.t. \quad \dot{r} = v \sin\gamma, \quad r(t_0) = r_0 \tag{4.29}$$

$$\dot{\theta} = \frac{v \cos\gamma \sin\psi}{r \cos\phi}, \quad \theta(t_0) = \theta_0 \tag{4.30}$$

$$\dot{\phi} = \frac{v \cos\gamma \cos\psi}{r}, \quad \phi(t_0) = \phi_0 \tag{4.31}$$

$$\dot{v} = -\frac{D(\alpha^*)}{m} - \frac{\mu \sin\gamma}{r^2}, \quad v(t_0) = v_0 \tag{4.32}$$

$$\dot{\gamma} = \frac{1}{v}\left(\frac{L(\alpha^*)}{m} + \left(v^2 - \frac{\mu}{r}\right)\frac{\gamma}{r}\right), \quad \gamma(t_0) = \gamma_0 \tag{4.33}$$

$$\dot{\psi} = \frac{1}{v}\left(\frac{Q(\beta)}{m\cos\gamma} + \frac{v^2}{r}\cos\gamma \sin\psi \tan\psi\right) \tag{4.34}$$

$$\beta_{Min} \leq \beta \leq \beta_{Max} \tag{4.35}$$

$$tf \vee free \tag{4.36}$$

Since the planet's rotation has been discarded, the $\psi_I \approx \psi$ and the final inclination of the orbit are computed from Equation 4.37. This equation accounts for the heading angle definition in the used set of equations of motion when compared to Equation 3.8. Then $\Phi(\boldsymbol{x}(t_f))$ will only have dependence on $\phi(t_f)$ and on $\psi(t_f)$.

$$\cos(i(t_f)) = \cos(\phi(t_f)) \sin(\psi(t_f)) \tag{4.37}$$

The problem's Hamiltonian is reported on Equation 4.38. Applying the *Pontryagin's Minimum Principle* to obtain the optimal control as bounded control exists yield to Equation 4.39.

$$H = \lambda_r \dot{r} + \lambda_\theta \dot{\theta} + \lambda_\phi \dot{\phi} + \lambda_v \dot{v} + \lambda_\gamma \dot{\gamma} + \lambda_\psi \dot{\psi} \tag{4.38}$$

$$\begin{aligned} H(\boldsymbol{x}^*, \beta^*, \boldsymbol{\lambda}^*, t) &\leq H(\boldsymbol{x}^*, \beta, \boldsymbol{\lambda}^*, t) \\ \therefore -\frac{\lambda_\psi^*}{v^*}\frac{\frac{1}{2}\rho^*(v^*)^2 S C_Q \beta^*}{m\cos\gamma^*} &\leq -\frac{\lambda_\psi^*}{v^*}\frac{\frac{1}{2}\rho^*(v^*)^2 S C_Q \beta}{m\cos\gamma^*} \end{aligned} \tag{4.39}$$

From the physical meaning of the variables involved, it can be stated that $S, C_Q, v^*, m, \rho^* > 0$. For γ, in the set of equations of motion used $\gamma \ni \left(-\frac{\pi}{2}, \frac{\pi}{2}\right)$, since for $\gamma = \pm\frac{\pi}{2}$ singularity exists. On the range $\left(-\frac{\pi}{2}, \frac{\pi}{2}\right)$ the $\cos(\gamma^*) > 0$. Consequently, the expression can be reduced to Equation 4.40.

$$-\lambda_\psi \beta^* \leq -\lambda_\psi \beta \tag{4.40}$$

After considering the different possible values, the heading co-state could take, the side-slip optimal control strategy yields Equation 4.41. The singular-arc case show-up, which could be proven to not exist through a proof by contradiction with the maximum's principle, and will be shown on subsubsection 4.1.4. Hence, when a linear control function is applied for the lateral channel, the optimal control follows a *'Bang-Bang'* structure, with λ_ψ as switching function.

$$\beta^* = \begin{cases} \beta_{Max} & if \quad \lambda_\psi > 0 \\ \beta_{Min} & if \quad \lambda_\psi < 0 \\ \in [\beta_{Min}, \beta_{Max}] & if \quad \lambda_\psi = 0 \end{cases} \tag{4.41}$$

Proof of Singular Arc Non-Existence

The proof is built by contradiction. Suppose the singular arc optimal control exists in $[t_1, t_2] \subset [t_0, t_f]$. From the singular-arc condition, we impose $\lambda_\psi = \dot{\lambda}_\psi = 0$, and it has to satisfy the co-state dynamics given in Equation 4.42.

$$\begin{aligned} \dot{\lambda}_\psi = -\frac{\delta H}{\delta \psi} &= 0 \\ \therefore -\lambda_\theta \frac{v\cos\gamma\cos\psi}{r\cos\phi} + \lambda_\phi \frac{v\cos\gamma\sin\psi}{r} &= 0 \end{aligned} \tag{4.42}$$

Computing the longitude's co-state dynamics yields that the longitude's Lagrange variable is constant Equation 4.43.

$$\dot{\lambda}_\theta = -\frac{\delta H}{\delta \theta} = 0 \rightarrow \lambda_\theta = constant \tag{4.43}$$

As a free time problem is posed, the transversality condition in differential form can be applied [43]. Where $dt_f \neq 0$ and $d\boldsymbol{x}_{t_f} \neq 0$, the equation between parenthesis Equation 4.44 shall be equal zero.

$$\left(H(t_f) + \frac{\partial \Phi}{\partial t_f} + \boldsymbol{\nu}^T \frac{\partial \Psi}{\partial t_f}\right) dt_f - \left(\frac{\partial \Phi}{\partial \boldsymbol{x}_{t_f}} + \boldsymbol{\nu}^T \frac{\partial \Psi}{\partial \boldsymbol{x}_{t_f}} - \boldsymbol{\lambda}^T(t_f)\right) d\boldsymbol{x}_{t_f} = \mathbf{0} \tag{4.44}$$

From the transversality condition Equation 4.45 yields. Recovering Equation 4.43 gives that the Lagrange multiplier for the longitude is zero for any time $\lambda_\theta(t) = 0$.

$$\left.\frac{\partial \Phi}{\partial \theta}\right|_{t_f} - \lambda_\theta(t_f) = 0 \rightarrow \lambda_\theta(t_f) = 0 \tag{4.45}$$

From Equation 4.43, introducing the results from Equation 4.43, assuming $r, v > 0$ and because of singularities $\gamma \in \left(\frac{-\pi}{2}, \frac{\pi}{2}\right) \rightarrow \cos\gamma > 0$ and $\phi \in \left(\frac{-\pi}{2}, \frac{\pi}{2}\right) \rightarrow \cos\phi > 0$, yields Equation 4.46.

$$\lambda_\phi \sin\psi = 0 \tag{4.46}$$

Applying Equation 4.44 to the set of variables that do not present a dependency with the objective function, Equation 4.47 are obtained.

$$\begin{cases} \left.\frac{\partial \Phi}{\partial r}\right|_{t_f} - \lambda_r(t_f) = 0 \rightarrow \lambda_r(t_f) = 0 \\ \left.\frac{\partial \Phi}{\partial v}\right|_{t_f} - \lambda_v(t_f) = 0 \rightarrow \lambda_v(t_f) = 0 \\ \left.\frac{\partial \Phi}{\partial \gamma}\right|_{t_f} - \lambda_\gamma(t_f) = 0 \rightarrow \lambda_\gamma(t_f) = 0 \end{cases} \tag{4.47}$$

From Equation 4.44 with $d\boldsymbol{x}_{t_f} \neq 0$, and no final constraints and an autonomous objective function, $H(t_f) = 0$. Considering the already proven $\lambda_r(t_f) = \lambda_\theta(t_f) = \lambda_v(t_f) = \lambda_\gamma(t_f) = \lambda_\psi(t_f) = 0$, the Hamiltonian at final time $H(t_f) = \lambda_\phi \dot{\phi}$, and assuming $r, v > 0$ and because of singularities $\cos\gamma > 0$, Equation 4.48.

$$H(t_f) = 0 \rightarrow \lambda_\phi(t_f)\cos\phi(t_f) = 0 \tag{4.48}$$

Equation 4.46 can be evaluated at final time, and combining with Equation 4.48, the system Equation 4.49 is obtained, which presents a solution for $\lambda_\phi(t_f) = 0$. Moreover, from the co-state dynamics, it can be demonstrated that the value is constant. Hence, the value for any time is zero Equation 4.50.

$$\begin{cases} \lambda_\phi(t_f)\sin\psi(t_f) = 0 \\ \lambda_\phi(t_f)\cos\psi(t_f) = 0 \end{cases} \rightarrow \lambda_\phi(t_f) = 0 \tag{4.49}$$

$$\dot{\lambda}_\phi = -\frac{\partial H}{\partial \phi} = 0 \rightarrow \dot{\lambda}_\phi = 0 \rightarrow \lambda_\phi = \textit{constant} \rightarrow \lambda_\phi(t) = 0 \tag{4.50}$$

From [30] and [21], there exist a continuous co-state function $\boldsymbol{\lambda}(t) \neq \mathbf{0}$ for $t \in [t_0, t_f]$. Hence, as here found, $\boldsymbol{\lambda}(t_f) = \mathbf{0}$ would suppose a contradiction with the multiplier rule, and hence, against the *Minimum Principle*. Therefore, it can be concluded that no-singular arc exists.

4.2. Online Guidance

The optimal control structures obtained from the trajectory optimisation shall be implemented on an algorithm to be set onboard the spacecraft. It must be robust against the different uncertainties to be encountered during the real trajectory. Computational burden is another critical factor to be considered since the trajectory shall be computed autonomously in real-time within the spacecraft's computational capabilities.

NPC has been selected for the online guidance scheme realisation. From existing aerocapture guidance schemes, NPC are the better-performing algorithms within reasonable computational requirements. As explained in subsection 4.2.1, the predictive model control can be skipped for computationally cheaper strategies on the prediction-correction phase. It shall also be mentioned that computational capabilities have undergone an important breakthrough during the last decades, mainly driven by Moore's law, leading to highly dense transistors in modern CPUs, substantially improving onboard computational capabilities and efficiency.

NPC provide further advantages, as based on an explicit scheme, the near-optimal trajectory is re-computed onboard without the need for further tuning on different mission cases. It confers the NPC with extraordinary flexibility, being capable of reducing the workload for its implementation on a mission design basis, considering different mission objectives. Its modularity allows for quick adjustment to the different target planets, requiring a single change in the atmospheric model values and planet parameters, and the correct address of the optimal trajectory if optimal guidance development is intended. Otherwise, setting the solver to use the guidance *Phase II* mode would lead to a nicely suited aerocapture guidance.

4.2.1. OCP Solution Implementation

As reported on section 4.1, the optimal control to be implemented on both channels would require to mimic a *'bang-bang'* control structure if for in-plane resolution ΔV is set as the objective functional. With a single switch, this kind of structure is proven to be numerically advantageous when implemented in an online guidance scheme.

This optimal control structure allows the resolution of a *'univariate parametric optimisation'*, where for the first phase, just the switch time of the control is used to obtain the minimum cost trajectory through the implementation of a numerical predictor-corrector. This guidance scheme is computationally cheaper when compared to model predictive control, where the optimal control of multiple variables is solved for a given control horizon.

Some actions, on the contrary, shall be taken to deal with day-of-flight uncertainty, such as density or wind variations. The first measure would come from preventing the control saturation after the switch. This would allow the spacecraft to act against unforeseen uncertainties arising after the control event.

The second measure to be introduced will come from introducing a second optimisation phase. This second phase will also be based on a univariate parametric optimisation that will compute the constant aerodynamic angle from the guidance call state till the prediction horizon to optimise the trajectory cost. This angle will be recomputed at each guidance call during the second phase of the guidance.

A bounded minimisation algorithm must be used to address the problem's discontinuities in order to solve the optimisation problem. *Golden Search* was employed by [39] for the optimal guidance; however, after some testing with an ad hoc developed algorithm, Matlab's *'fminbnd'* has shown comparatively faster convergence. This function implements a golden search algorithm, coupled with parabolic interpolation, and due to its computational advantage, has been selected for the online guidance logic.

Finally, the online guidance implementation can be summarised as a multiphase NPC guidance, where optimal ΔV trajectory is solved by mimicking the bang-bang control structure. Two different guidance logics are found corresponding to the lateral and the longitudinal channel. The prediction horizon is considered up till the atmospheric exit interface. The optimisation can be solved separately, allowing a parallel or asynchronous computation. The guidance phases are reported:

- **Phase 1:** Control switch time used as a decision variable.
- **Transition Phase:** Guidance Call is skipped, as the control switch is being performed.
- **Phase 2:** Constant Angle of Attack (AoA)/Side-slip angle is computed as the decision variable.

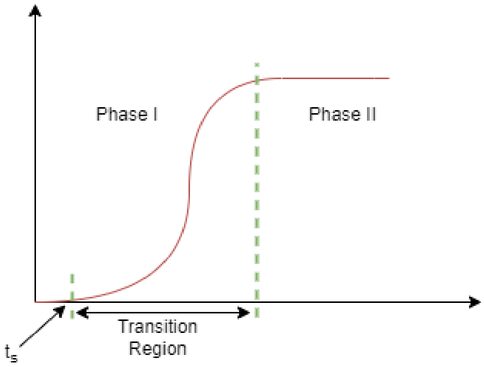

Figure 4.9: Phases Schematic

4.2.2. Overall Guidance Architecture

Here a global perspective of online guidance is provided, where all the main constituents of the guidance scheme and its logic will be introduced. The process flow diagram is provided in Figure 4.10. Each of the processes will be explained schematically as follow:

- **Initial State:** The initial state at the atmospheric Entry Interface (EI) is provided in rotational spherical variables. The initial conditions shall be within the aerocapture's feasible region for the aimed trajectory. For its computation, the *Aerocapture Designer* program developed during this thesis can be used.
- **NPC:** Takes the aerocapture's equations of motion and numerically propagates them till the trajectory's end. After each prediction, the optimisation problem is solved in the correction phase. The number of prediction-correction cycles will be limited, and it shall be guaranteed that the process is completed faster than the

guidance execution frequency rate. So, a trade-off between accuracy and computational time shall be performed for its adjustment on a real-time operating system and according to the CPU's computational capabilities. It will provide the optimal aerodynamic angles to be actuated.

- **Propagator:** Once the control strategy is obtained from the NPC, the spacecraft's state is propagated till the next guidance call. The obtained state will be cyclically used for the next guidance iteration.
- **Navigation Filter:** Day-of-flight variations and un-modelled phenomena, such as winds on the online-guidance model, will be encountered throughout the trajectory. The navigation filter is introduced to close the loop with the real system and act as an interface with the real system. It will make use of the onboard sensors to update the model-based states.

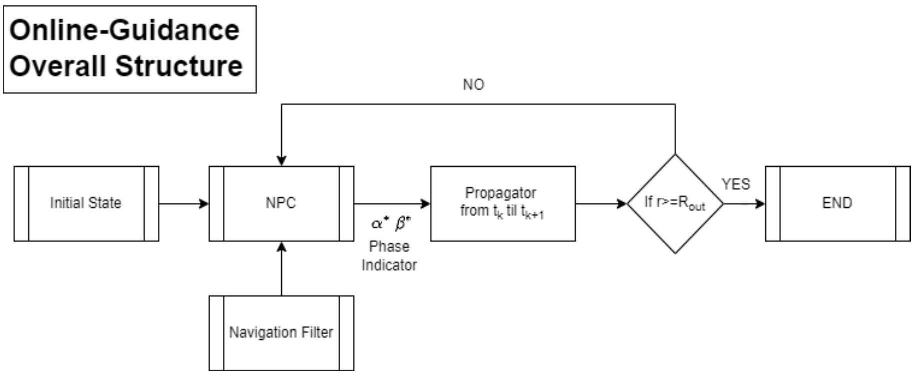

Figure 4.10: Online Guidance General Architecture

The whole online guidance iteration shall take a shorter time for its execution than the inverse of the frequency of the guidance call. The frequency of the guidance will affect its capability to withstand uncertainty, as higher inputs from the navigation filter could be introduced to the model, and faster reaction capacity will be obtained from the system. However, this frequency shall be low enough for the CPU to perform the whole sequence of computations before the next guidance call initialisation. To illustrate better the processes to be completed at each call in a timely disposed manner, Figure 4.11 is provided.

4.2.3. NPC

As an optimality-based guidance scheme is developed, a bounded optimisation algorithm is introduced for the real-time optimisation of the trajectory. In this case, Matlab's *'fminbnd'* function was employed, as it proved faster and computationally efficient when compared to the ad hoc *'Golden Search'* algorithm developed. The NPC will contain

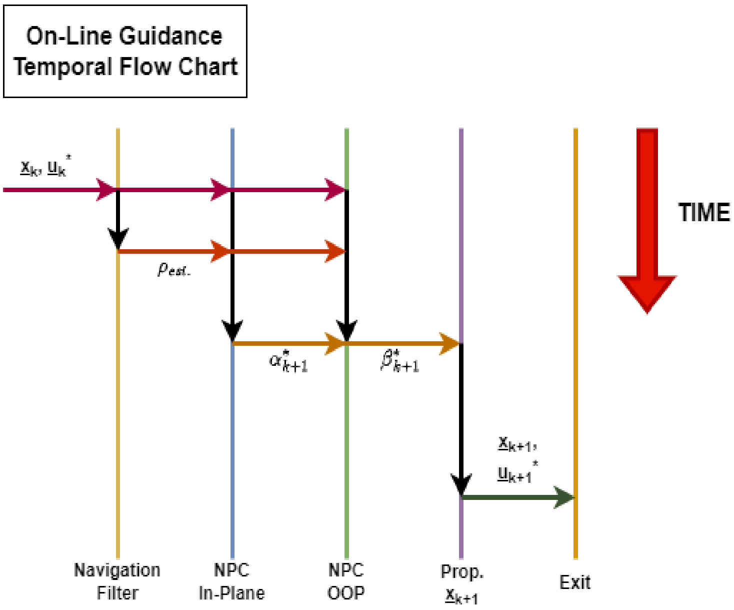

Figure 4.11: Temporal Flow-Chart

a phase identification algorithm that will autonomously identify the current phase of the guidance and optimise according to the corresponding decision variable. This phase identifier will be one of the NPC outputs for the rest of the system and will be used by the propagator on the aerodynamic angle computing phase. The following IDs identify the phases:

- **ID=0:** Corresponds to the Transition phase of the guidance.
- **ID=1:** Corresponds to Phase 1 of the guidance.
- **ID=2:** Corresponds to Phase 2 of the guidance.

During phase 2, the temporal aerodynamic angle state at the moment of the guidance call is reported to the NPC and considered by the optimiser. The best decision is made considering the spacecraft's temporal state and the angle change's manoeuvrer delay. Two output conditions exist for the NPC, relative tolerance achieved on the minimisation problem or the maximum number of function evaluations exceeded.

Phase Identifier

Identifying autonomously the phase the spacecraft is found in is of paramount importance for the NPC, as the decision variable will vary. Hence, a phase identifier shall be implemented. The flow chart reporting the phase identifier within the NPC is reported on Figure 4.13. The main question would be identifying whether we are on the *'Phase*

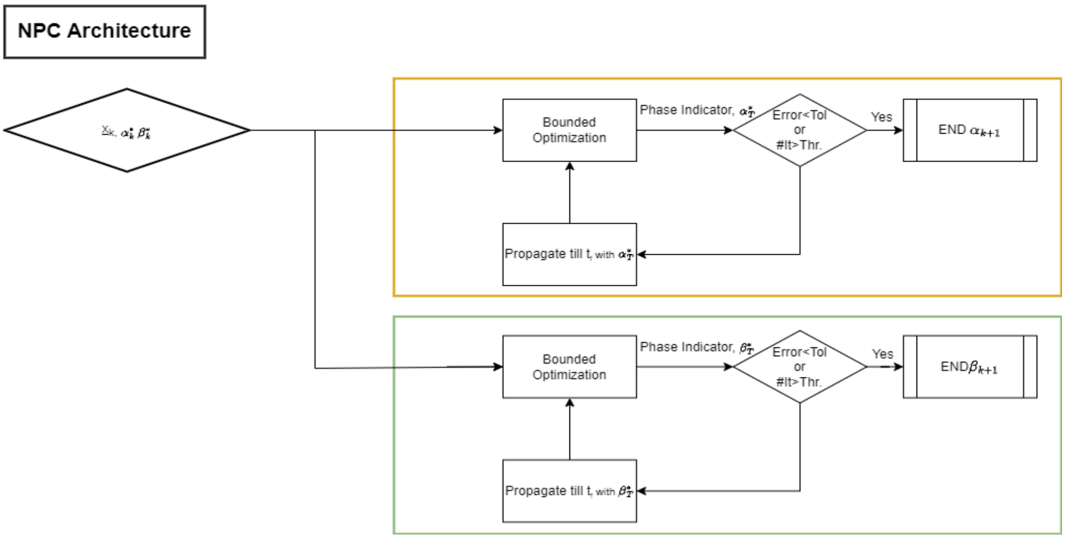
NPC Architecture
$\chi_k, \alpha_k^*, \beta_k^*$
Bounded Optimization
Phase Indicator, α_T^*
Error<Tol or #It>Thr.
Yes
END α_{k+1}
Propagate till t_s with α_T^*
Bounded Optimization
Phase Indicator, β_T^*
Error<Tol or #It>Thr.
Yes
ENDβ_{k+1}
Propagate till t_s with β_T^*

Figure 4.12: NPC Architecture

1' of the guidance. As time is being used as a solution for the optimisation, this can be easily identified through the algorithm presented, where t_s^{k-1} corresponds to the switch time computed on the last guidance call. Then, the algorithm shall be initiated with a large enough t_s (t_s^{init}> 1/f), and the guidance will enter from the beginning in phase 1 up till the switching manoeuvre is performed.

```
if $t_k \geq t_s^{k-1}$ then
    $ID = PHASE\ \ 1$
else if $t_k \geq t_s^{k-1} + \Delta t_{Man.}$ then
    $ID = PHASE\ \ 2$
else
    $ID = PHASE\ \ 0$
end if
```

A sensed acceleration activation system is suggested by [23] to activate the aerocapture guidance. In that case, for IMU-measured accelerations greater than 0.5 m/s^2, the aerocapture's online guidance would begin working. Another option, and here followed one, is to activate the guidance from a given threshold altitude concerning the target planet.

4.2.4. Pseudo Actuator

No rotational equations of motion have been considered, and only 3-DOF point mass actuations are used, a common practice in aerocapture's guidance schemes. However, on [86][12] have introduced a pseudo actuator to apply kinematic constraints into its rotational response, mimicking the actual controller's behaviour. Here a control command

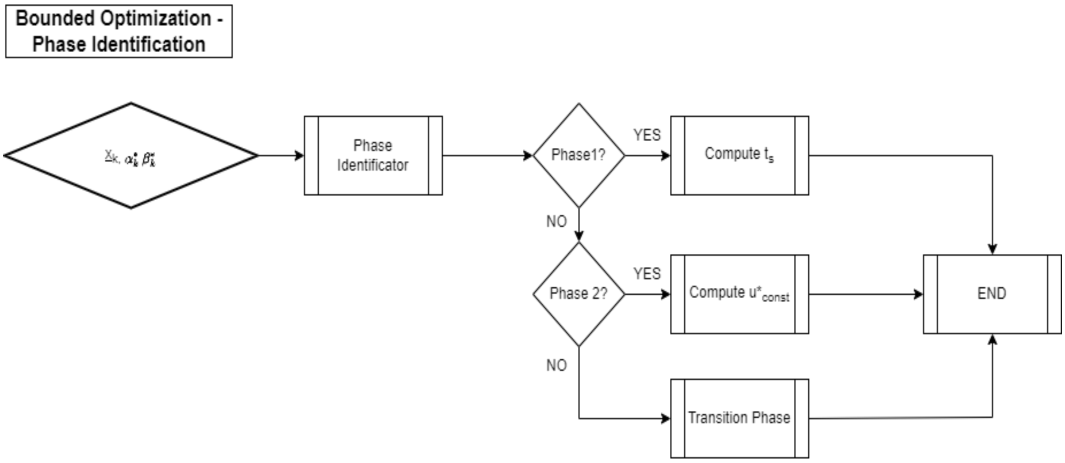
Bounded Optimization - Phase Identification
$\underline{x}_k, \alpha^*_k, \beta^*_k$
Phase Identificator
Phase1?
YES
Compute t_s
NO
Phase 2?
YES
Compute u^*_{const}
END
NO
Transition Phase

Figure 4.13: Phase Identifier

limiter considering the vehicle capabilities, such as the maximum rate, $\dot{u}_{Max}$, and acceleration, $\ddot{u}_{Max}$, is employed. This implementation is based on a second-order Taylor series approximation of the control time response Equation 4.51.

$$u(t) \approx u_0 + \dot{u}_{Max}\Delta t + \frac{1}{2}\ddot{u}_{Max}\Delta t^2 \tag{4.51}$$

Faster rate and acceleration limits are advantageous for the guidance, as a higher responsivity would be obtained, leading to lower manoeuvre cost and higher capability of trajectory error correction. Selected values have been taken from DFC literature. More precisely, [48] considers for a low L/D vehicle $\dot{u}_{Max} = 2.5[deg/s]$ and $\dot{u}_{Max} = 1.0[deg/s^2]$. In the present thesis, these values have been halved to produce a conservative result of the guidance and account for the possible control authority reduction on the small-satellite kind. Used results are found in Table 4.4.

Table 4.4: Control Limiter Values

Property	Value
Rate Limit	1.25 [deg/s]
Accel Limit	0.5 [deg/s^2]

4.2.5. Atmospheric Model

The employed atmospheric model for the online guidance is the one introduced in subsection 2.3.2. This is a 1-D piece-wise linearisation of *MarsGram 2010* 's nominal density. A nominal density value is used as it will provide a mid-point value between the higher and lower ranges of the possible outcome values. Lumping the values to a single-dimensional variable retrieves a high computational efficiency for the online guidance.

Other effects, such as winds or dust particles' presence in the atmosphere, have been discarded, mainly due to reducing the algorithm's computational burden. The navigation filter is introduced to the guidance scheme to account for these values. Better modelling would lead to better guidance results, but the limited computational capabilities shall be considered.

4.2.6. Navigation Filter

Aerocapture trajectory happens at a hypersonic flight regime, which is characterised by some fluid phenomena, mainly related to high temperatures that dissociate gas species on the vehicle's boundary layer. Therefore, the surrounding environment of the vehicle is ionised. This charged gas would prevent external communications with the spacecraft during the trajectory or even taking direct measurements.

Therefore, IMU's measurements would be the primary source of information for the onboard model update. Recent implementations introduce first-order fading memory filters [44] to account for all the uncertainty and un-modelled effects of the NPC. It accounts for older values of the estimate and introduces new estimates to the parameter. Recalls the working behaviour to the one of Kalman Filter but with a constant gain instead of a recursively updated one. The main point of doing so is reducing the navigation filter's computational requirements, which has proven to be sufficient for other aerocapture guidance schemes on bank-angle modulation. In the case of discretised event drag modulation, some studies such as [61] have been conducted, as control is saturated during the second phase of the aerocapture. However, these new navigation filters deserve higher research as substantial simplifications were assumed during the study and are stated to be presumptuous in conclusion.

The equation governing the implemented first-order fading memory filter is reported on Equation 4.52. The obtained $\tilde{\boldsymbol{\rho}}^k$ vector is used as a multiplier on the aerodynamic force computation during the k^{th} guidance call. The value of the gain is user-specified and deals with the filter's bandwidth. Higher values of G imply more reliance towards the onboard model, and lower values will imply more 'aggressive' updates from IMU measurement accelerations.

$$\begin{gathered}\tilde{\boldsymbol{\rho}}^k = \tilde{\boldsymbol{\rho}}^{k-1} + (1-G)\left(\boldsymbol{\rho} - \tilde{\boldsymbol{\rho}}^{k-1}\right) \\ with \quad 0 \leq G \leq 1 \quad and \quad \boldsymbol{\rho} = \frac{\boldsymbol{a}_{Aero}^{IMU}}{\boldsymbol{a}_{Aero}^{Model}}\end{gathered} \tag{4.52}$$

The filter's gain is one of the main parameters to be tuned by the guidance scheme designer. Its correct selection would imply better results and fewer failure cases. Given the mission case, a proper testing campaign would be required to address this value adequately, onboard used models and mission-specific parameters.

In the present research, some small testing has been conducted, but the best performance selection cannot be guaranteed due to time and computational capabilities limitations. In the current mission scenario, due to the high uncertainty, the presence of dust storms, the systematic aerodynamic error in the introduction of the 1-D coefficients, and the unmodelled presence of winds lead to the better performance obtained for more aggressive filters. However, G=0.1 led to several failed cases, and a good compromise between performance and robustness was found for G=0.2.

4.2.7. Aerodynamic Coefficients

The model used for the online guidance is the one presented in subsection 2.1.5. The functions added on top of the 1-D coefficient model, to which polynomial regression has been applied. The model has been developed to create a function that fits well in the region in which this coefficient exhibits validity. The lift and lateral coefficients were calculated using linear polynomials. In contrast, the drag coefficient was calculated using a second-order polynomial since polynomial regression offers a good fit and has fewer computational needs.

4.2.8. Relief Logic

Suppose an error on the Trajectory Correction Manoeuvre (TCM) is given, and the spacecraft is set into the wrong entry point. The guidance will optimise the trajectory to get the targeted one up to its capabilities. However, during that trajectory, some of the trajectory or vehicle constraints could be violated.

Even if the final target is not achieved, that may vary depending on the entry spot and the vehicle's capabilities. Maintaining the spacecraft alive is preferable, as later mission parameters could be adjusted and modified. Hence, it is essential to introduce some relief logic to prevent constraint violations up to the control authority capacity.

According to previously mentioned during the mission analysis, the two major destructive violations we could face on Mars' aerocapture are related to minimum flight altitude and maximum dynamic pressure, as found to be the most restrictive constraints on the mission analysis study. Therefore, a relief logic has been introduced for these two figures.

Both parameters relate to flight altitude, as the density depends exponentially on them. The relief logic cannot easily control other terms, such as velocity, so it cannot be used. The logic to reduce dynamic pressure would be related to increasing the minimum altitude at which the vehicle is expected to fly. The dynamic pressure will be lower at the same velocity but higher altitude. So it can be concluded that both parameters' relief logic is equivalent on the actuation side.

Where the minimum altitude that can be modified in the trajectory is during the descending leg, which is actuated mainly by Phase 1 of the guidance, not to get that deep into the atmosphere, a higher aerodynamic lift force must be actuated, as it is the force that would be depleting the vertical momentum. Hence, the angle α shall decrease to get a higher lift and increase the trajectory's minimum altitude.

However, due to the updated coefficient coming from the navigation filter, estimating the minimum altitude from a predictive logic does not seem robust, as it may affect the relief even in feasible trajectories when high-intensity but short-duration perturbations may occur during the guidance call, such as wind gusts or denser air packets, which can lead to penalising correct manoeuvres. As a result, it has been preferred, a relief logic that actuates when some current state margins are violated. Being a reactional logic, after a success happens, the response is given. The mission designer can establish these values for the constraints during the guidance set-up.

The angle of attack to be commanded shall maximise the lift, leading to selecting the maximum aerodynamic efficiency point, which the user shall also report during the set-up. Even if this relief logic is activated, the optimisation problem will be done by the guidance to target the objective. However, as higher aerodynamic angles are used, higher non-linearities will be introduced in the dynamics. A higher error with respect to the online model is performed, resulting in a performance decrease and a higher estimate drift.

Results of the relief logic are shown on Figure 4.14 and compared to a non-active scenario. Being a reactive logic, it is limited to the aerodynamic control authority. Engine activation could be included at a lower threshold to increase reactiveness. However, this logic has not been included in the present work and could be added in the future.

4.3. Guidance Failure Cases and Solutions

During the guidance testing phase, some not expected failure cases were found. These failures led to 14% failure cases under the considered uncertainty and real system modelling,

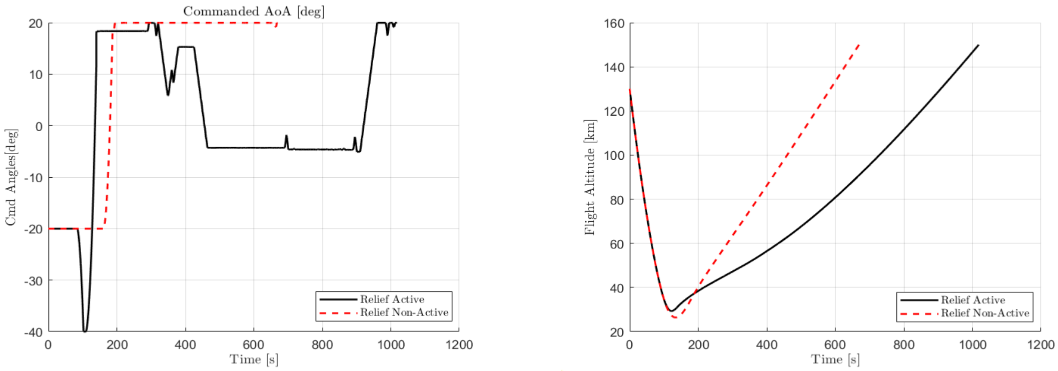

(a) Angle of Attack History (b) Effect on Flight Altitude

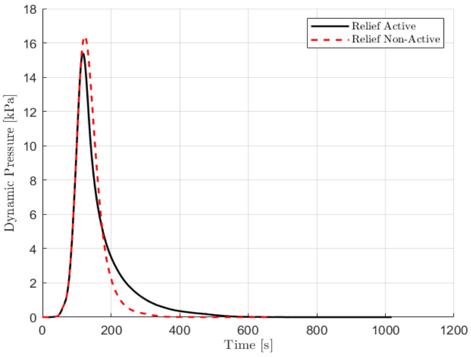

(c) Effect on Dynamic Pressure

Figure 4.14: Relief Logic Demonstration

which is far from acceptable. No strong correlation was found concerning atmospheric entry flight path angle variation or dust storm intensity Figure 4.15.

Consequently, a more detailed analysis of the failed cases was necessary to understand the underlying cause of the trajectory failure. After the investigation, two different cases were found to appear, with two different underlying logic.

4.3.1. Failure Case 1

ID Kamikaze

Reasoning Given the limitation on the number of iterations for the 1^{st} phase solver, it fails to obtain a convergence at the beginning. The first resolutions are harder since the solver has to cover a wider search space.

Autopsy Fail on the resolution during the first guidance call, obtained switch time is lower than the time of the following guidance call, so the actuation is performed, and

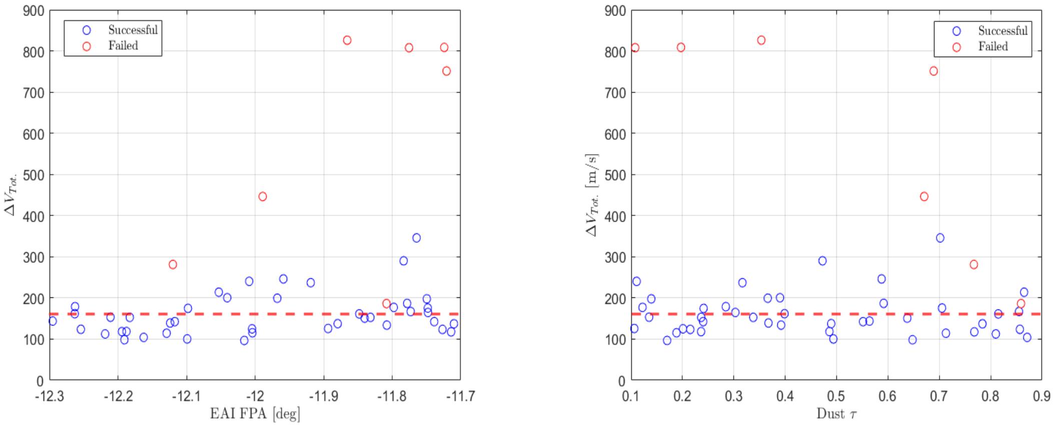

(a) Failure cases with respect to FPA

(b) Failure cases with respect to Dustτ

Figure 4.15: Failure Cases on 25 samples Monte Carlo Analysis

corrections cannot be accomplished during the transition region. Phase II is unable to deal with the correction.

Introduced Solution From the NPC solution during Phase I of the guidance, the minimum predictor's altitude will be reported. If the predictors' minimum altitude is lower than a certain threshold, the solution will not be used, and the first previous valid solution is maintained. This solution will allow shallow trajectory performance, and only prevent convergence failure cases.

4.3.2. Failure Case 2

ID Energy

Reasoning The Online Model fails on the correct trajectory estimation and deploys too much kinetic energy from the trajectory. It seems a failure in correctly estimating the trajectory's energy by the guidance.

Autopsy All obtained *Energy* cases presented the same common element. Because the mean for the online model was considered a medium point on the real dispersion, some samples accounted for a real radius lower than the one provided by the online model. When this difference was high enough, the overestimation of the energy led to excessive energy depletion by the guidance. It is found on r because it presents a higher dispersion.

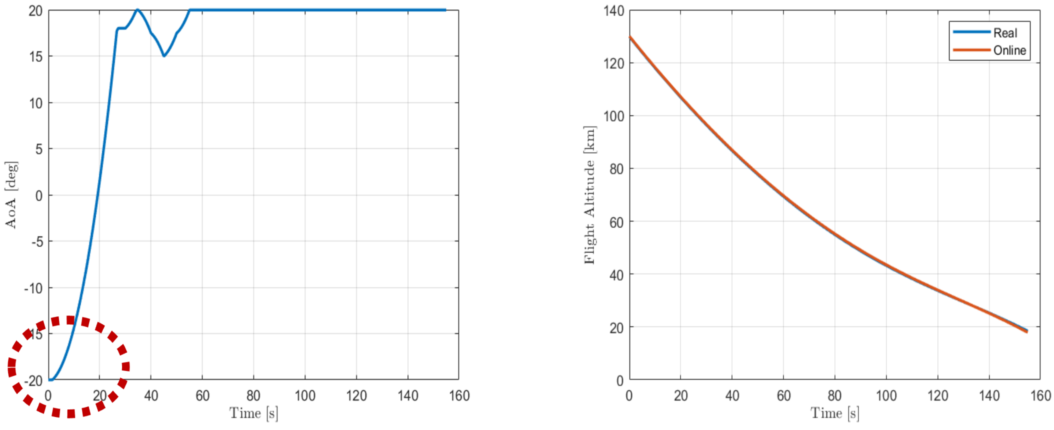

(a) Angle of Atack Profile.

(b) Flight Altitude Profile.

Figure 4.16: Failure Case 1 Profile

Introduced Solution The guidance fails to deal with sufficiently *'big'* energy overestimation. Hence, when considering high uncertainties, the floor of the uncertainty state is used. It is more robust since failure is prevented at the cost of worsening the outcome of the trajectory.

4.4. Algorithm Validation

Only a few direct force control guidance schemes with Mars applications can be found. [48] Re-implemented guidance based on NASA's FNPAG for DFC. The target orbit for the guidance scheme's behaviour demonstration is $r_a = 33793$ and $h_p = 250$ [km] from the paper's considered mission, and dispersion provided in Table 4.5 were used.

Table 4.5: Monte Carlo Dispersions of [48]

Variable	Dispersion
Initial Longitude	normal, σ=0.08333 [deg]
Initial Latitude	normal, σ=0.08333 [deg]
Initial Flight Path Angle	normal, σ=0.03333 [deg]
Initial Azimuth	normal,σ=0.08333 [deg]
Initial Velocity	normal, σ=3.333 [m/s]

From the study, for such an elliptical orbit, obtained results of ΔV for Bang-Bang mode lie within 10 and 40 m/s and the wedge angle between 0.2 degrees after the Monte Carlo analysis. A single guidance run with Table 4.5, targeting an $r_a = 33000$ km, $h_p = 250$ km, and $i^* = 80$ degrees, will be performed to understand the comparative guidance

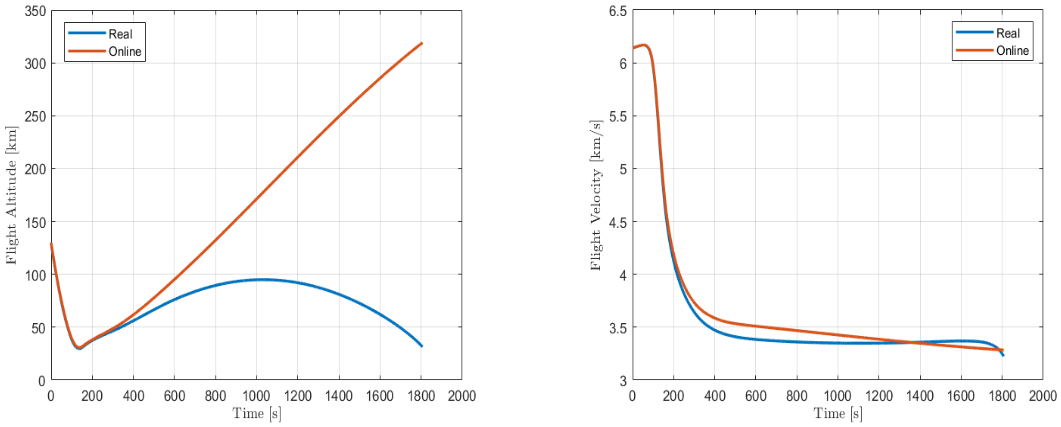

(a) Flight Altitude Profile.

(b) Flight Velocity Profile.

Figure 4.17: Failure Case 2 Profile

performance. In Figure 3.12, the feasible region is depicted. For this analysis, the initial velocity equals 7 [km/s], and an initial flight path angle of -12 [deg] has been introduced.

This analysis does not consider sensitivity or robustness but the algorithm's performance. Hence, if the single run results lay within [48] obtained results, the algorithm can be considered to be working in a comparable way. Obtained results are reported on Table 4.6. Results show the correct performance of the algorithm and lay within the average results reported, even in different mission scenarios, with different capsules, initial conditions and systematic errors considered.

Table 4.6: Algorithm Validation Results

Variable	Value
Planar ΔV	22.9 [m/s]
Wedge Angle	0.12 [deg]
r_a	31776 [km]

4.5. Navigation Dispersion Sensitivity Analysis

As the navigation filter during aerocapture trajectory is based on indirect IMU measurements, a drift on the trajectory is expected. Consequently, navigation uncertainty is expected to play a major role in guidance performance. Only a few studies of aerocapture for small satellites on Mars navigation are found, on [23] entry dispersion from [59] are considered. These are correlated from MSL [79]. These are reported on Table 4.7 and will be used as the baseline for the sensitivity analysis.

Table 4.7: Monte Carlo Baseline Dispersion [59][23]

Parameter	Dispersion Maximum/Minimum or 3σ
Atmospheric Interface (AI) Velocity	0.49 [m/s]
AI Flight Path	0.013 [deg]
AI Azimuth	0.0075 [deg]
AI Latitude	0.017 [deg]
AI Longitude	0.012 [deg]
AI Altitude	0.74 [km]

The sensitivity analysis has been performed setting the same MarsGram density, winds and dust storm conditions, leading to a deterministic study scenario, and taking the maximum values of Table 4.7 and applying a varying safety factor. The subsection 4.3.2 measurement has been applied to prevent atmospheric crashes. The target orbit is the one presented in Table 4.10, where the minimum is $\Delta V = 88.8[m/s]$ obtained from the optimal control problem resolution and will serve as the *'Carnot'* ideal value.

Obtained results are reported on Figure 4.17, and a strong correlation between the uncertainty level and the guidance scheme's precision is observed. The guidance shows robustness against the increment of uncertainty level, as the bias is introduced on the low energetic level. For the case in which no approach navigation uncertainty is found (SF=0), a total ΔV of 110 m/s is found. This implies that a 25% efficiency decrement is obtained with respect to the ideal case when adapting to the optimal logic and compared to the real system model case, where some higher fidelity values and effects are accounted for. On the contrary, little change is found in the final's orbit inclination.

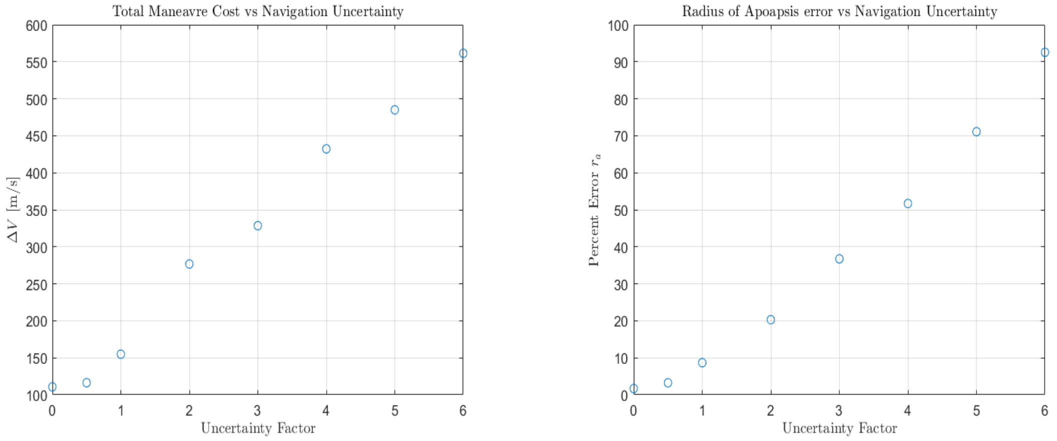

(a) ΔV vs Navigation Error.

(b) r_a vs Navigation Error.

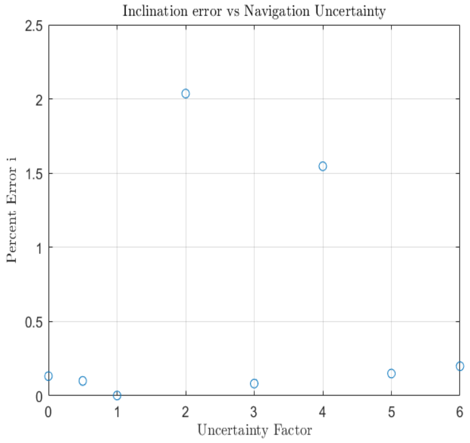

(c) i vs Navigation Error.

Figure 4.17: Approach Navigation Error vs Guidance Performance

However, for increasing uncertainty values, a rapid worsening of the aerocapture guidance performance is obtained, reducing the attractiveness of the aerocapture mission if posterior big propulsive manoeuvres are expected. Hence, two scenarios could be faced, greater uncertainty management with less sensitive atmospheric insertion for later atmospheric correction by aerobraking. Or more precise atmospheric entry target and navigation, propulsive orbit corrections. These selections shall be system based considered as different trade-offs are introduced on the mission.

4.6. Monte Carlo Analysis

4.6.1. Test Conditions

Approach Navigation

From gained experience on *LiciaCube* mission, for the navigation of small satellites in deep space, from the numerical analysis, a B-plane uncertainty with an almost 10 km circular ellipse was expected [2][16]. On the deep space operations phase, the 1σ covariance for the state after 48 hours of the last DSN tracking passage, using both ranging and doppler data Equation 4.53 on ECLIPJ200 reference frame.

$$\begin{bmatrix} \sigma_x \\ \sigma_y \\ \sigma_z \\ \sigma_{v_x} \\ \sigma_{v_y} \\ \sigma_{v_z} \end{bmatrix} = \begin{bmatrix} 8 \quad [km] \\ 8 \quad [km] \\ 3.5 \quad [km] \\ 2e-5 \quad [km/s] \\ 2e-5 \quad [km/s] \\ 1.3e-5 \quad [km/s] \end{bmatrix} \tag{4.53}$$

Of course, this mission set does present radical differences, even on the navigation side, as the uncertainty considered on aerocapture is with respect to a planet. Then the uncertainty factor could be decreased, accounting for the planet's ephemeris precision-wise. Another matter of fact is that covariance reduction campaigns are suggested some hours before the atmospheric insertion, so 48 hours spaced measurements account for an increase in the covariance due to the uncertainty propagation. However, even if this is accounted for, velocity terms with respect to Table 4.7 are not under-estimated, but position-related components present a much higher uncertainty. As a result, a 100% safety factor has been applied to Table 4.7 position-related components to consider conservative values of the spacecraft's uncertainty. For the Monte Carlo analysis, the trajectories have been simulated on the 26^{th} of December 2022, at 12:34:40 LST.

Table 4.8: Monte Carlo Dispersions of the Analysis

Variable	Maximum Dispersion
Initial Radius	uniform, σ=1.48 [km]
Initial Longitude	uniform, σ=0.024 [deg]
Initial Latitude	uniform, σ=0.034 [deg]
Initial Flight Path Angle	uniform, σ=0.013 [deg]
Initial Azimuth	uniform,σ=0.0075 [deg]
Initial Velocity	uniform, σ=0.49 [m/s]
Mass	linear in time, m = 3/1500 [kg/s]
Bank Angle	systematic, 1 [deg]
Gram Random Seed	uniform, 1-29999
Gram Dust τ	uniform, 0.1-0.9
Aero Coefficients	systematic, 10%
Atmospheric Winds	MarsGram
Atmospheric Density	MarsGram

Atmospheric Interface Entry Uncertainty

On [84], four approach manoeuvres were scheduled during the last two months of the cruise phase to obtain the insertion precision level required at the atmospheric interface.

They considered an FPA=±0.3[deg] (3σ) delivery inaccuracy. This uncertainty is argued to be high due to propulsive manoeuvres occurring within the measurement time and the atmospheric insertion. Thus, they maintain a high level of uncertainty. If those thrusting events are not present, the uncertainty could be highly reduced at the entry spot. The delivery state has been introduced in the Monte Carlo simulation through a uniform distribution.

Initial Conditions and Target Orbit

The initial conditions of the trajectory are reported on Table 4.9. Moreover, the target orbit parameters are given in Table 4.10. The target orbit is then a low-altitude circular high-inclination orbit.

Table 4.9: Monte Carlo Analysis Initial Conditions

Parameter	Value
h_{EI}	130 [km]
θ_{EI}	30 [deg]
ϕ_{EI}	0 [deg]
V_{EI}	6.1 [km/s]
$\overline{\gamma}_{EI}$	-12 [deg]
ψ_{EI}	10 [deg]

Table 4.10: Monte Carlo Analysis Target Orbit

Parameter	Value
h_a^*	400 [km]
h_p^*	400 [km]
i^*	80 [deg]

4.6.2. Obtained Results

One hundred samples of Monte Carlo analysis have been conducted. Obtained results are reported on Figure 4.18. Some of the already observed trends on section 4.1 are again appreciated. From 4.19c, higher maximum dynamic pressures are encountered for lower values of the entry flight path angle and lower values of the total stagnation point heat 4.19d. It is a direct consequence of the shorter flight time as a lower flight profile is encountered for the same amount of orbital energy depletion, leading to higher energy dissipation rates. For the total manoeuvre cost computation, the strategy used in [86], where the periapsis raise and the inclination correction is performanced simultaneously as reported in Equation 4.54.

$$\Delta V_{Tot.} = \Delta V_2 + \sqrt{\Delta V_1^2 + \Delta V_3^2} \tag{4.54}$$

This higher time of flight can also explain the trend of ΔV increment with respect to the entry Flight Path angle 4.19a. Since for higher trajectory time, higher will be the error accumulation effect. One out-layer can be found on the ΔV results. From 4.18g it can be addressed that the combination of two main effects produces it, the FPA and the navigation uncertainty effect reported on section 4.5. The combination of the high level of navigation uncertainty and high trajectory time of flight then explains the worst-behaving result.

No failure cases are obtained on this analysis, where introduce measurements given in section 4.3 are already applied. No correlation between guidance performance and dust storm intensity is found, and it can be concluded that the guidance is robust against them.

For the lateral channel case reported in 4.18f, most results lay well-within 0.5 degrees, improving the performance for the increase in the value of the entry flight path angle. It could be caused by the low control authority on the out-of-plane channel, as reported in the feasibility analysis. Also, due to this limitation, three out layers can be found, which have not been able to tackle the atmospheric uncertainty during the trajectory. A lateral channel's logic miss-behaviour can cause the out-layers, and further analysis would be required for its determination. However, the obtained maximum error for the final inclination is lower than two degrees.

The statistical performance data of the analysis is reported on Table 4.11. Here also, the reduced case delivery uncertainty has been considered since high variation with respect to the entry flight path angle has been observed—a 27% performance improvement over the full delivery dispersion is found on the 3σ value. The commanded aerodynamic angle profiles can be found on Figure 4.18.

Table 4.11: Monte Carlo Analysis Results

Case [deg]	Mean	3σ	1^{st} Percentile	50^{th} Percentile	99^{th} Percentile
Periapsis Raise FPA=[-12.3,-11.7]	87.5 [m/s]	106.5 [m/s]	74.2 [m/s]	86.7 [m/s]	107.8 [m/s]
Periapsis Raise FPA=[-12.3, -12]	90.5 [m/s]	105.8 [m/s]	83.4 [m/s]	90.1 [m/s]	111.6 [m/s]
Apoapsis Correction FPA=[-12.3,-11.7]	81.8 [m/s]	267.6 [m/s]	9.82e-4 [m/s]	71.5 [m/s]	306.9 [m/s]
Apoapsis Correction FPA=[-12.3, -12]	56.2 [m/s]	166.7 [m/s]	4.93e-4 [m/s]	45.9 [m/s]	144.2 [m/s]
Inclination Correction FPA=[-12.3,-11.7]	13.5 [m/s]	62.9 [m/s]	1.07e-4 [m/s]	12.5 [m/s]	103.4 [m/s]
Incliantion Correction FPA=[-12.3, -12]	17 [m/s]	65.9 [m/s]	6.5 [m/s]	14.6 [m/s]	103 [m/s]
Total FPA=[-12.3,-11.7]	171.43 [m/s]	339.90 [m/s]	95.74 [m/s]	160.74 [m/s]	381.59 [m/s]
Total FPA=[-12.3, -12]	149.39 [m/s]	248.26 [m/s]	96.19 [m/s]	144.78 [m/s]	230.32 [m/s]

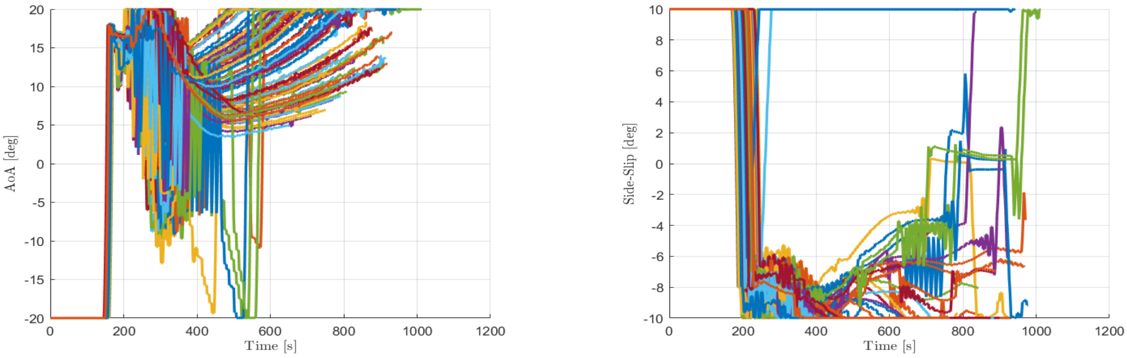

(a) Commanded Angle of Attack Profiles.

(b) Commanded Side Slip Profiles.

Figure 4.18: Online Guidance Commanded Aerodynamic Angle Profiles

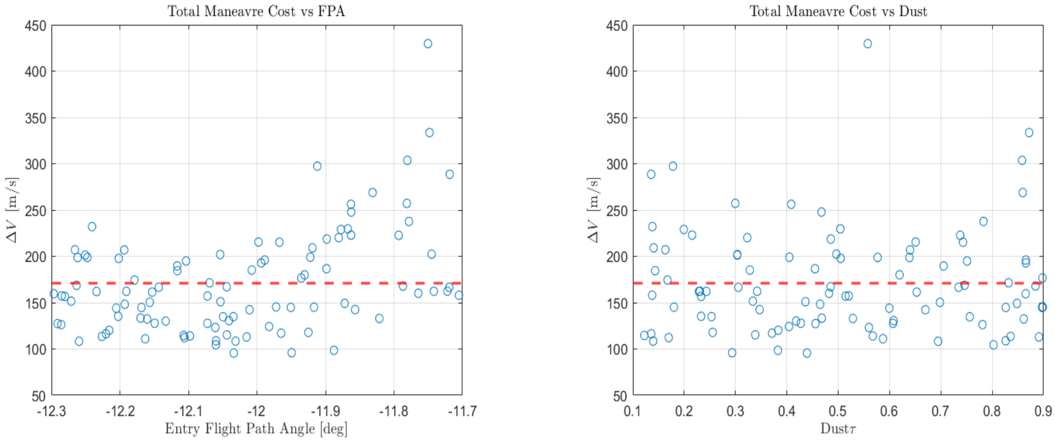

(a) ΔV vs FPA at EI.

(b) ΔV vs Atmospheric Dustτ parameter.

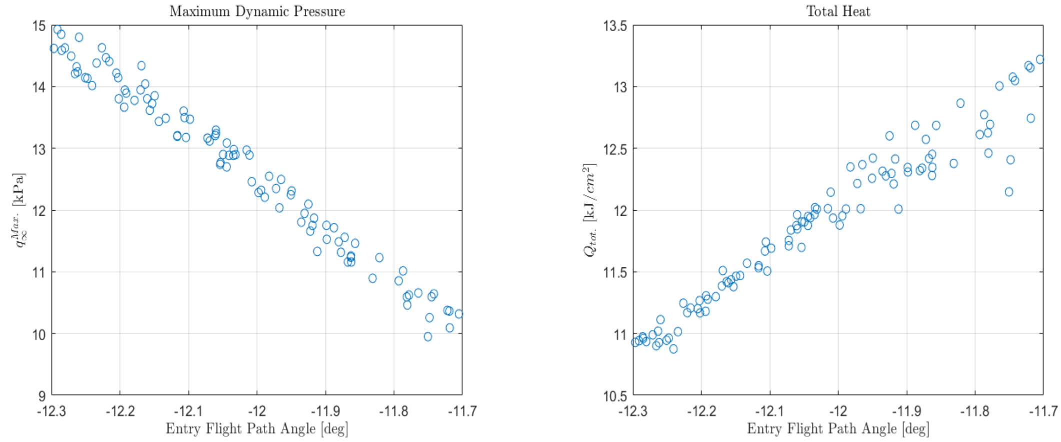

(c) Maximum Dynamic Pressure.

(d) Total Stagnation Point Trajectory Heat.

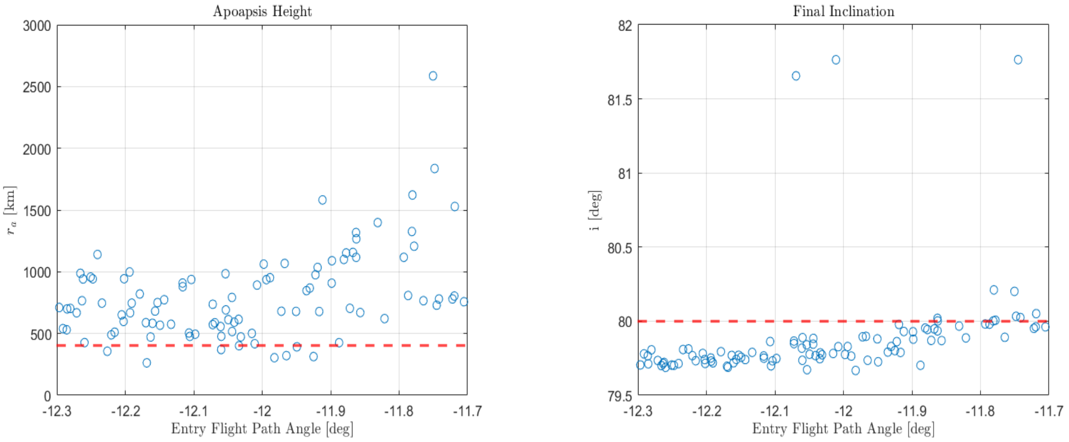

(e) Final Radius of Apoapsis Height.

(f) Final Orbit's inclination.

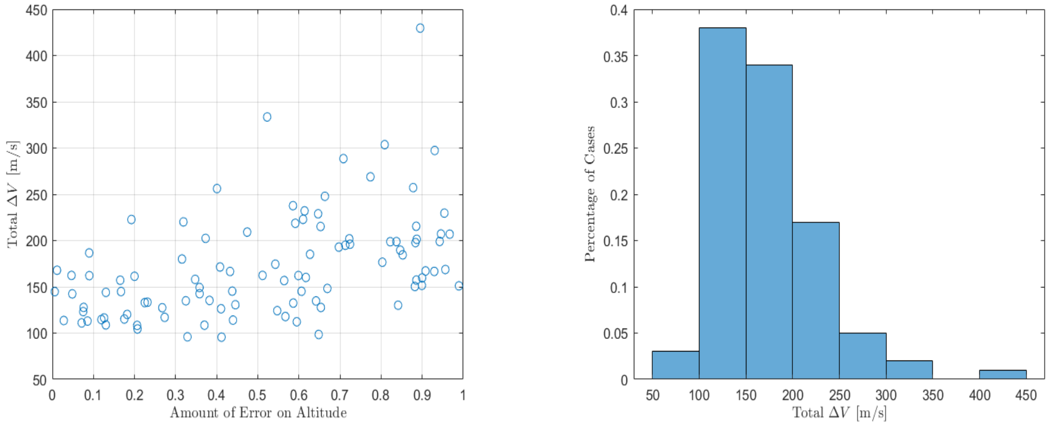

(g) ΔV vs Altitude Navigation error.

(h) ΔV Histogram for 0.6 degrees FPA insertion.

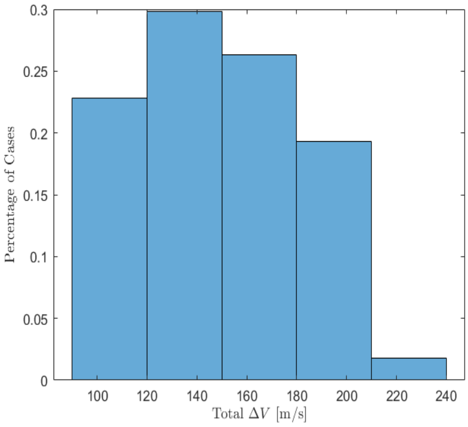

(i) ΔV Histogram for 0.3 degrees FPA insertion.

Figure 4.18: Monte Carlo Analysis Trajectory Results

4.6.3. Sizing and Fully-Propulsive Comparison

Both 3σ values provided in Table 4.11 are used for the aerocapture trajectory sizing comparison with respect to the fully-propulsive capture case. Some assumptions and simplifications have been considered for the sizing. The fully-propulsive computations have been performed through the process reported on section 2.7. For the aerocapture case, the process followed is reported on section 4.1. Some effects, such as worsened usable volume from capsule-like vehicle shape restrictions, have not been accounted for. A 25% safety margin has been introduced to account for the engine and tank for the propulsive sizings. The aerocapture sizing account for the propulsive and the thermal systems required for the manoeuvre. A total heat of 15 kJ/cm^2 for the total heat has been considered on the TPS sizing to account for a 10% margin with respect to the worst-case scenario. Small satellites' maximum mass and volume are reported on Table 3.1.

Table 4.12: 0.6[deg] FPA Dispersion Aerocapture vs Fully-Propulsive Capture

Property	Aerocapture	Fully-Propulsive	Benefit
ΔV (3σ)	340 [m/s]	2.65 [km/s]	87.17%
Mass	36.47 [kg]	156.26 [kg]	76.66%
Volume	0.0494 [m^3]	0.1556 [m^3]	68.25%
Available Mass from Maximum	79.84%	13.66%	119.78 [kg]
Available Volume from Maximum	88.20%	62.80%	0.106 [m^3]

Table 4.13: 0.3[deg] FPA Dispersion Aerocapture vs Fully-Propulsive Capture

Property	Aerocapture	Fully-Propulsive	Benefit
ΔV (3σ)	248.26 [m/s]	2.65 [km/s]	90.63%
Mass	28.42 [kg]	156.26 [kg]	81.81%
Volume	0.0413 [m^3]	0.1556 [m^3]	72.36%
Available Mass from Maximum	84.30%	13.66%	127.84 [kg]
Available Volume from Maximum	90.12%	62.80%	0.114 [m^3]

Results on Table 4.12 and Table 4.13 report the great advantage of aerocapture compared to the fully propulsive case. This resulted in accomplishing a doable mission for the small satellite class aerocapture.

4.6.4. Conclusions

The developed guidance scheme proved robust against the day of flight uncertainty on the tested real system model, including when dust storm conditions are present. The atmospheric entry flight path angle proved two different trends. For lower flight path angles, better longitudinal channel performance is obtained due to the reduced flight time. However, mainly provoked by the reduced control authority of the lateral channel, the out plane results are improved when the higher time of flights are encountered, leading to better results for higher entry flight path angles. The lateral guidance logic could be improved as performed on the longitudinal channel to prevent out-layer cases. However, due to the limited population, it has yet to be performed and has not been done in the current thesis guidance implementation.

Sizing results proved to lead feasible mission case when aerocapture is used on the provided mission. Aerocapture is a mission enabler technology, as fully-propulsive results appear unfeasible due to the high propulsive system requirements. These results can be even improved if navigation and insertion uncertainty is further reduced, leading to almost halved post-atmospheric manoeuvring cost as reported from section 4.5. This best case proves the near-optimal performance of the aerocapture scheme implementation adapted to trajectory uncertainty, with an approximate 25% performance worsening compared to the optimal deterministic case.

Provided results can not be argued to extract the better achievable performance with the present guidance scheme since higher-level analysis shall be performed for the parameter tuning, which is not achieved in the present work due to computational and time limitations. The parameters to be tuned on the guidance scheme are:

- Guidance Frequency.
- Maximum Number of Function Evaluations of the NPC.
- Navigation Filter Gain.
- Maximum/Minimum Aerodynamic angle achieved on the transition phase to prevent the control saturation.

Therefore, several measures for aerocapture guidance performance improvement are possible. Aerocapture then poses as a mission enabler on Mars for small satellites. In the case of DFC applied on aeroshell capsule-like vehicles, it provides a good suit for low-orbit insertions. The propulsive requirements for aerocapture can be reduced to the ΔV required for the periapsis raise, and apoapsis correction can be achieved by fast deep aerobraking provided heat shield and the close to the final obtained result of the orbit. However, this strategy implies an operationally intensive scenario and a risk increment on the manoeuvre.

5 | Conclusions

5.1. Thesis Conclusions

The research questions formulated at the beginning of the thesis, in section 1.2, will now be answered schematically.

- **Q1: Is using the direct force control on a small-satellite class mission with an aeroshell capsule-like vehicle feasible for Mars aerocapture?**
  It can be concluded that aerocapture on Mars using DFC on an aeroshell capsule-like vehicle is feasible. The relaxation provided by the aeroshell capsule-kind compared to drag sail vehicles enables the aerocapture to be performed on Mars. A correct capsule aerodynamic optimization shall be performed to increment the L/D ratio, so as to obtain enough corridor width for the vast range of arrival conditions and targeted orbits, even if low aerodynamic efficiency capsule shapes are employed. Since a lower reference surface is encountered, the vehicle shall dive deeper into the atmosphere, and higher heat and dynamic loads are encountered. As Mars presents an abrupt scenery, minimum altitude flight shall be restricted from the mission analysis phase to prevent a crash against the mons. Maximum Dynamic pressure is the most restrictive constraint, and relief logic shall be implemented in case this is overcome. The squeezing of the feasible region for the higher radius of apoapsis targeting leads to a better suit of the DFC on small satellites aeroshell capsule-like vehicles to low to medium target orbits. The non-jettisoning required during aerocapture allows its utilisation on later aerobraking manoeuvres, which can exploit the fact of deeper dives into the atmosphere to reduce the aerobraking manoeuvre time, taking advantage of the remaining TPS.

- **Q2: Does the guidance present enough robustness against expected trajectory uncertainties?**
  Not a conclusive answer can be provided in this respect. A 100% capture rate with no failure has been obtained from the 100 Monte Carlo analysis when the failure-preventing measures section 4.3 on the guidance were implemented. However, even

if realistic and stochastic trends have been implemented, the real system modelling does not completely represent the trajectory reality. Thus, it can be concluded that the guidance scheme shows robust behaviour when tested on the developed 'Real System' model developed, and high perturbation conditions are introduced, such as dust storms. From the mission analysis side, wide enough corridors are present for a vast range of mission scenarios. This parameter is directly related to the aerocapture trajectory robustness, leading to a reinforcement of the outcome obtained from the Monte Carlo analysis.

- **Q3: Does this approach provide any advantage compared to existing SmallSat aerocapture concepts?**
  Again, a closed answer cannot be reported since the guidance performance will depend on several factors, concerning mainly target and navigation dispersions and the real system's modelling. Some conceptually related advantages can be provided as a result. DFC provides the capability of out-of-plane manoeuvring, which presents a comparative advantage with respect to DM aerocapture. It also prevents the saturation of the control authority during the whole trajectory range, which leads to potential improvement of the results. Another comparative advantage is the non-depletion of the aerodynamic shield during the trajectory, allowing its utilization for a later aerobraking manoeuvre differently from jettison drag modulation techniques studied on small satellites. From section 4.5, a near-optimal result can be obtained from the case of zero atmospheric interface uncertainty, corresponding to a 25% worsening on the overall ΔV. Hence, the guidance could be considered to provide great performance, finding a bottleneck in the atmospheric insertion uncertainty, and on the online's navigation filter.

5.2. Critical Points

The main guidance bottleneck is found because of navigation limitations. Since no state updates during the trajectory exist, the initial state error is propagated forward in the model and added to the model's existing error. Consequently, state drift arises as the trajectory time increases, reported on Figure 5.1. This provokes drastic performance issues, greatly impacted by the dispersions of the state knowledge at the atmospheric insertion, as proved in section 4.5.

As a consequence, navigation uncertainty reduction campaigns will be necessary previous to the atmospheric entry. Radiometric tracking from DSN and OpNav, which is a technique that improves the angular position with respect to the planetary body [17] by exploitation of the onboard camera system, would be required. This would allow navigation uncertainty reduction, which would turn into drift mitigation.

Within this respect, limiting the number of TCM during the last hours prior to the atmospheric insertion would allow for lowering the uncertainty over the entry flight path angle, leading to a reduction of the time of flight, preventing shallower sides, that proved to provide worse results due to the error accumulation.

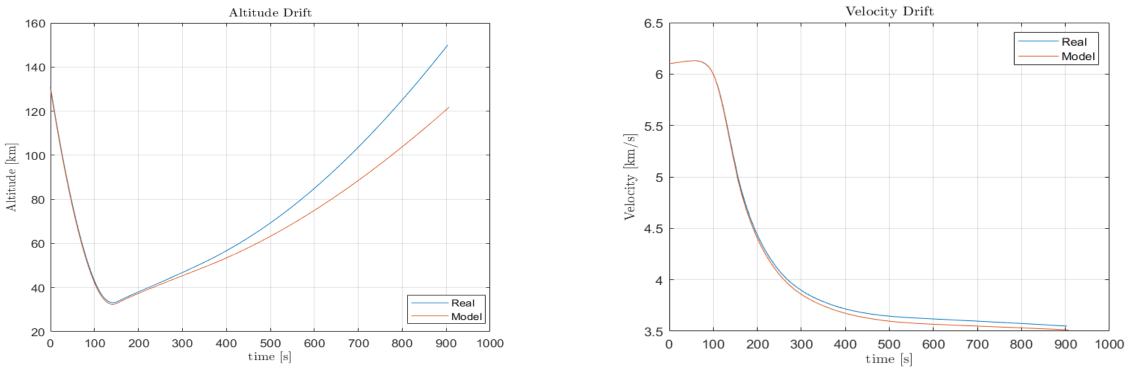

(a) Altitude Drift.

(b) Velocity Drift.

Figure 5.1: Online Model State Variables Drift

Considered vehicle aerodynamics are appropriate for a preliminary study, but higher detail analysis would be required. Some over-simplifying assumptions on the aerodynamic coefficient computations, such as not considering viscosity effects or assuming them constant over the whole hypersonic regime. Dynamical and stability analysis has not adequately been conducted to address the hyperbolic parameter variation aerodynamic effect, nor has the volume availability of the payloads and subsystems been considered.

Even if NPC guidance has been selected for its modularity and adaptability properties, initial tuning is required according to the target planet and the tested spacecraft. A thoughtful empirical analysis shall be conducted to achieve the parameters that result in better performance of the guidance scheme, where parameter variation combinations are considered, and results are compared. Such analysis has yet to be done in the present work. Consequently, it can not be stated to be working at its best.

The lateral channel displays 3% cases of misbehaviour. Similar debugging reported for the longitudinal channel on section 4.3 shall be performed. However, the low incidence and the small population's capability to perform the analysis prevented the suggestion of a solution introduction and correction verification. Further studies shall tackle this problem and perform a big enough Monte Carlo analysis to verify its correctness. Therefore, reported performance results have been worsened by this fact, and a considerable improvement in the 3σ scenario is expected when correction measures are effectively applied.

5.3. Suggested Future Work

From the aerocapture navigation-wise perspective, improving the navigation filtering capabilities could turn aerocapture into an even more appealing alternative, reducing the criticality of the atmospheric entry phase. This improvement could be achieved by several meanings, such as by introducing new measurement sources to the navigation filter or introducing more advanced navigation filters as suggested in [61]; where density array interpolator and ensemble correlation filters were suggested. For example, measurements from FADS could also be added to a Kalman Filter to improve the estimation capabilities. Another option is the one presented in [87], which introduced the stochastic optimization on aerocapture for BAM, reporting slightly improved results compared to the OAK [86] NPC algorithm. However, it introduced a much higher computational burden when compared to traditional NPC, which may prevent its applicability to small satellite-class missions.

Better filter implementation supposes an increment in the required computational power, which is limited for small satellites. AI solutions could provide some computational advantages for improving the computational cost of the guidance algorithm, such as machine learning networks to substitute the numerical integration of the NPC algorithm.

The optimal control structure is based on a deterministic environment case. In reality, the atmospheric environment does not behave deterministic-ally but in a random way instead. Then, it can be argued that the optimal solution does not correspond to the one provided on section 4.1. For the outcomes obtained in the present study, state drift on the model has been identified to be the most limiting factor in the guidance performance. Even if lower cost trajectories could be obtained on the guidance, no direct improvement would be obtained in the final results. These optimality-based algorithms could be an interesting study path if the navigation bottleneck is overcome.

Bibliography

[1] S. Aerisystems. Extreme materials - pica, 2023. URL `https://www.spiritaero.com/programs/defense/extreme-materials/pica/`.

[2] M. Amoroso, S. Pirrotta, V. Della Corte, E. Dotto, I. Bertini, J. Brucato, A. Capannolo, G. Zanotti, B. Cotugno, J. Deshapriya, et al. Liciacube: a deep space cubsat to witness the first asteroid kinetic impactor test. In *INTERNATIONAL ASTRONAUTICAL CONGRESS: IAC PROCEEDINGS*, pages 1–10, 2022.

[3] J. D. Anderson. *Hypersonic and high temperature gas dynamics*. Aiaa, 2000.

[4] R. C. B. AS and A. L. Xavier. A unified satellite taxonomy proposal based on mass and size. *Advances in Aerospace Science and Technology*, 4(04):57–73, 2019.

[5] A. Austin, G. Afonso, et al. Enabling and enhancing science exploration across the solar system: Aerocapture technology for smallsat to flagship missions. Technical Report 4, 2021.

[6] . S. T. R. Beauchamp, P. M. An assesment of aerocapture and applications to future missions. Technical report, Jet Propulsion Laboratory, Pasadena, California, 2 2016.

[7] S. Bhaskaran. Autonomous navigation for deep space missions. In *SpaceOps 2012*, page 1267135. 2012.

[8] C. Cerimele and J. Gamble. A simplified guidance algorithm for lifting aeroassist orbital transfer vehicles. In *23rd Aerospace sciences meeting*, page 348, 1985.

[9] A. Chakrabarty, S. S.-M. Swei, and D. K. Prabhu. Tree based trajectory planning for mars aerocapture. In *AIAA Atmospheric Flight Mechanics Conference*, page 0277, 2016.

[10] I. H. Cihan and C. A. Kluever. Analytical earth-aerocapture guidance with near-optimal performance. *Journal of Guidance, Control, and Dynamics*, 44(1):45–56, 2021.

[11] I. H. Cihan and C. A. Kluever. Analytical guidance for mars aerocapture via drag modulation. *The Journal of the Astronautical Sciences*, 69(3):857–878, 2022.

[12] R. G. Deshmukh. *System Analysis of a Numerical Predictor-Corrector Aerocapture Guidance Architecture*. PhD thesis, Purdue University Graduate School, 2021.

[13] R. G. Deshmukh, D. A. Spencer, and S. Dutta. Investigation of direct force control for aerocapture at neptune. *Acta Astronautica*, 175:375–386, 2020.

[14] H. D.J.Lickly and B.S.Crawford. Apollo reentry guidance. Technical report, NASA, Cambridge, Massachussets, 7 1963.

[15] D.Mages. *ESPA User's Guide*. MOOG Space and Defense Group, 1 edition, 11 2018.

[16] E. Dotto, V. Della Corte, M. Amoroso, I. Bertini, J. Brucato, A. Capannolo, B. Cotugno, G. Cremonese, V. Di Tana, I. Gai, et al. Liciacube-the light italian cubesat for imaging of asteroids in support of the nasa dart mission towards asteroid (65803) didymos. *Planetary and Space Science*, 199:105185, 2021.

[17] S. Dutta, G. Afonso, S. W. Albert, H. K. Ali, G. A. Allen, A. I. Alunni, J. O. Arnold, A. Austin, G. Bailet, S. Bhaskaran, et al. Aerocapture as an enhancing option for ice giants missions. Technical report, 2020.

[18] A. Dwyer Cianciolo and R. W. Powell. Entry, descent, and landing guidance and control approaches to satisfy mars human mission landing criteria. In *AAS/AIAA Space Flight Mechanics Meeting*, number AAS Paper 17-254, 2017.

[19] A. M. DwyerCianciolo, J. L. Davis, D. R. Komar, M. M. Munk, J. A. Samareh, R. W. Powell, J. D. Shidner, D. O. Stanley, A. W. Wilhite, D. J. Kinney, et al. Entry, descent and landing systems analysis study: Phase 1 report. Technical report, 2010.

[20] M. E.Sigal. Optimal aerocapture with minimum total heat load. Toulouse, France, 2001. 52nd International Astronautical Congress.

[21] G. M. Ewing. *Calculus of variations with applications*. Courier Corporation, 1985.

[22] G. Falcone, J. Williams, and Z. R. Putnam. Aerocapture system options for delivery of small satellites to mars. pages 271–284, 2018.

[23] G. Falcone, J. Williams, and Z. Putnam. Assessment of aerocapture for orbit insertion of small satellites at mars. *Journal of Spacecraft and Rockets*, 56(6):1689–1703, 2019.

[24] J. Gamble, C. Cerimele, T. Moore, and J. Higgins. Atmospheric guidance concepts

for an aeroassist flight experiment. *Journal of the Astronautical Sciences*, 36:45–71, 1988.

[25] J. K. Geiser and D. A. Matz. Optimal angle of attack control for aerocapture. In *AIAA SCITECH 2022 Forum*, page 0608, 2022.

[26] A. P. Girija. *A Systems Framework and Analysis Tool for Rapid Conceptual Design of Aerocapture Missions*. PhD thesis, Purdue University Graduate School, 2021.

[27] J. L. Hall, M. A. Noca, and R. W. Bailey. Cost-benefit analysis of the aerocapture mission set. *Journal of Spacecraft and Rockets*, 42(2):309–320, 2005.

[28] J.-F. Hamel and J. De Lafontaine. Improvement to the analytical predictor-corrector guidance algorithm applied to mars aerocapture. *Journal of guidance, control, and dynamics*, 29(4):1019–1022, 2006.

[29] H. Han, D. Qiao, and H. Chen. Optimal ballistic coefficient control for mars aerocapture. In *2016 IEEE Chinese Guidance, Navigation and Control Conference (CGNCC)*, pages 2175–2180. IEEE, 2016.

[30] M. R. Hestenes. *Calculus of variations and optimal control theory*. Wiley, 1966.

[31] S. Hughes, F. Cheatwood, R. Dillman, A. Calomino, H. Wright, J. DelCorso, and A. Calomino. Hypersonic inflatable aerodynamic decelerator (hiad) technology development overview. Technical report, 2011.

[32] G. Isoletta, M. Grassi, E. Fantino, D. de la Torre Sangrà, and J. Peláez. Feasibility study of aerocapture at mars with an innovative deployable heat shield. Technical Report 6, 2021.

[33] R. Jits and G. Walberg. High l/d mars aerocapture for 2001, 2003 and 2005 mission opportunities. page 299, 1998.

[34] M. Johnston, P. Esposito, V. Alwar, S. Demcak, E. Graat, and R. Mase. Mars global surveyor aerobraking at mars. Technical report, 1998.

[35] H. Justh. Mars global reference atmospheric model 2010 version: Users guide. Technical report, 2014.

[36] C. D. Karlgaard, P. Kutty, and M. Schoenenberger. Coupled inertial navigation and flush air data sensing algorithm for atmosphere estimation. *Journal of Spacecraft and Rockets*, 54(1):128–140, 2017.

[37] M. Kelly. An introduction to trajectory optimization: How to do your own direct collocation. *SIAM Review*, 59(4):849–904, 2017.

[38] O. K.Percy, E.Bright. Assesing the relative risk of aerocapture using probabilistic risk assesment. AIAA/ASME/SAE/ASEE Joint Propulsion Conference and Exhibit, 2005.

[39] J. M. Lafleur. The conditional equivalence of δv minimization and apoapsis targeting in numerical predictor-corrector aerocapture guidance. Technical report, 2011.

[40] H. S. LONDON. Change of satellite orbit plane by aerodynamic maneuvering. *Journal of Aerospace Sciences*, 56:323–332, 1962.

[41] A. C. Long, J. Cappellari Jr, C. Velez, and A. Fuchs. Goddard trajectory determination system (gtds) mathematical theory (revision 1). Technical report, 1989.

[42] S. M. Long, T.-H. You, C. A. Halsell, R. S. Bhat, S. W. Demcak, E. J. Graat, E. S. Higa, D. E. Highsmith, N. A. Mottinger, and M. K. Jah. Mars reconnaissance orbiter aerobraking daily operations and collision avoidance. Technical report, 2007.

[43] J. M. Longuski, J. J. Guzmán, and J. E. Prussing. *Optimal control with aerospace applications*. Springer, 2014.

[44] P. Lu, C. J. Cerimele, M. A. Tigges, and D. A. Matz. Optimal aerocapture guidance. *Journal of Guidance, Control, and Dynamics*, 38(4):553–565, 2015.

[45] D. T. Lyons, R. S. Saunders, and D. G. Griffith. The magellan venus mapping mission: aerobraking operations. *Acta Astronautica*, 35(9-11):669–676, 1995.

[46] K. Mall, M. J. Grant, and E. Taheri. Uniform trigonometrization method for optimal control problems with control and state constraints. *Journal of Spacecraft and Rockets*, 57(5):995–1007, 2020.

[47] J. Masciarelli, S. Rousseau, H. Fraysse, and E. Perot. An analytic aerocapture guidance algorithm for the mars sample return orbiter. In *Atmospheric flight mechanics conference*, page 4116, 2000.

[48] D. A. Matz and C. Cerimele. Development of a numeric predictor-corrector aerocapture guidance for direct force control. Technical report, 2020.

[49] M.Cruz. The aerocapture vehicle mission design concept. *Jet Propulsion Laboratory*, pages 195–201, 1980.

[50] A. Miele, Z. Zhao, and W. Lee. Optimal trajectories for the aeroassisted flight experiment. part 1: Equations of motion in an earth-fixed system. Technical report, 1989.

[51] E. Mooij. The motion of a vehicle in a planetary atmosphere. Technical report, 1994.

[52] NASA. 4.0 in-space propulsion, 2022. URL `https://www.nasa.gov/smallsat-institute/sst-soa/in-space-propulsion`.

[53] NASA. Mars fact sheet, 2023. URL `https://nssdc.gsfc.nasa.gov/planetary/factsheet/marsfact.html`.

[54] H. Otsu. Aerodynamic characteristics of re-entry capsules with hyperbolic contours. *Aerospace*, 8(10):287, 2021.

[55] Y.-m. Peng, B. Xu, B.-d. Fang, and H.-l. Lei. Analytical predictor-corrector guidance algorithm based on drag modulation flight control system for mars aerocapture. *International Journal of Aerospace Engineering*, 2018, 2018.

[56] Y.-m. Peng, B. Xu, X. Lu, B.-d. Fang, and H. Zhang. Analytical predictive guidance algorithm based on single ballistic coefficient switching for mars aerocapture. *International Journal of Aerospace Engineering*, 2019, 2019.

[57] B. Petropoulos and C. Macris. Physical parameters of the martian atmosphere. *Earth, Moon, and Planets*, 46:1–30, 1989.

[58] R. W. Powell and R. D. Braun. Six-degree-of-freedom guidance and control analysis of mars aerocapture. *Journal of Guidance, Control, and Dynamics*, 16(6):1038–1044, 1993.

[59] Z. R. Putnam and R. D. Braun. Drag-modulation flight-control system options for planetary aerocapture. *Journal of Spacecraft and Rockets*, 51(1):139–150, 2014.

[60] T. Ro and E. Queen. Study of martian aerocapture terminal point guidance. In *23rd Atmospheric Flight Mechanics Conference*, page 4571, 1998.

[61] E. Roelke, P. D. Hattis, and R. Braun. Improved atmospheric estimation for aerocapture guidance. In *2019 AAS/AIAA Astrodynamics Specialist Conference*, 2019.

[62] E. Roelke, J. W. McMahon, R. D. Braun, and P. D. Hattis. Multi-event jettison guidance approaches for drag-modulation aerocapture. *Journal of Spacecraft and Rockets*, 59(1):190–202, 2022.

[63] T. C. Rolim, S. C. Cintra, and M. M. d. C. Pellegrini. Development and application of computational tool using local surface inclination methods for preliminary analysis of hypersonic vehicles. *Journal of Aerospace Technology and Management*, 12, 2020.

[64] S. Rousseau. An energy controller aerocapture guidance algorithm for the mars sample return orbiter. In *Proceedings of the 11 th Annual AAS/AIAA Space Flight Mechanics Meeting, Santa Barbara, CA*, pages 67–83, 2001.

[65] S. Rousseau, E. Perot, C. Graves, J. Masciarelli, and E. Queen. Aerocapture guidance algorithm comparison campaign. In *AIAA/AAS Astrodynamics Specialist Conference and Exhibit*, page 4822, 2002.

[66] S. Sepka and J. A. Samareh. Thermal protection system mass estimating relationships for blunt-body, earth entry spacecraft. In *45th AIAA Thermophysics Conference*, page 2507, 2015.

[67] E. Sigal and M. Guelman. Optimal aerocapture with minimum total heat load. In *Proceedings of the 52nd International Astronautical Congress*, 2001.

[68] B. Smith, A. Cassell, C. Kruger, E. Venkatapathy, C. Kazemba, and K. Simonis. Nano-adept: An entry system for secondary payloads. In *2015 IEEE Aerospace Conference*, pages 1–11. IEEE, 2015.

[69] K. M. Smith. Predictive lateral logic for numerical entry guidance algorithms. In *AAS/AIAA Space Flight Mechanics Meeting*, number JSC-CN-35110-1, 2016.

[70] J. C. Smith Jr and J. L. Bell. 2001 mars odyssey aerobraking. *Journal of spacecraft and rockets*, 42(3):406–415, 2005.

[71] T. R. Spilker, M. Adler, N. Arora, P. M. Beauchamp, J. A. Cutts, M. M. Munk, R. W. Powell, R. D. Braun, and P. F. Wercinski. Qualitative assessment of aerocapture and applications to future missions. *Journal of Spacecraft and Rockets*, 56(2):536–545, 2019.

[72] M. Srinivasan and A. Ruina. Computer optimization of a minimal biped model discovers walking and running. *Nature*, 439(7072):72–75, 2006.

[73] A. G. Stephenson, D. R. Mulville, F. H. Bauer, G. A. Dukeman, P. Norvig, L. S. LaPiana, P. J. Rutledge, D. Folta, and R. Sackheim. Mars climate orbiter mishap investigation board phase i report, 44 pp. Technical report, 1999.

[74] M. Tigges, B. Bihari, J.-P. Stephens, G. Vos, K. Bilimoria, E. Mueller, H. Law, W. Johnson, R. Bailey, and E. Jackson. Orion capsule handling qualities for atmospheric entry. *AIAA Guidance, Navigation, and Control Conference 2011*, 08 2011. doi: 10.2514/6.2011-6264.

[75] H. Tran, C. Johnson, D. Rasky, F. Hui, M.-T. Hsu, and Y. Chen. Phenolic impregnated carbon ablators (pica) for discovery class missions. In *31st Thermophysics Conference*, page 1911, 1996.

[76] E. Venkatapathy, K. Hamm, I. Fernandez, J. Arnold, D. Kinney, B. Laub, A. Makino,

M. McGuire, K. Peterson, D. Prabhu, et al. Adaptive deployable entry and placement technology (adept): a feasibility study for human missions to mars. In *21st AIAA Aerodynamic Decelerator Systems Technology Conference and Seminar*, page 2608, 2011.

[77] K. F. Wakker. Fundamentals of astrodynamics. Technical report, 2015.

[78] D. W. Way, R. W. Powell, A. Chen, A. D. Steltzner, A. M. San Martin, P. D. Burkhart, and G. F. Mendeck. Mars science laboratory: Entry, descent, and landing system performance. In *2007 IEEE Aerospace Conference*, pages 1–19. IEEE, 2007.

[79] D. W. Way, R. W. Powell, A. Chen, A. D. Steltzner, A. M. San Martin, P. D. Burkhart, and G. F. Mendeck. Mars science laboratory: Entry, descent, and landing system performance. In *2007 IEEE Aerospace Conference*, pages 1–19. IEEE, 2007.

[80] P. Wercinski, W. Henline, H. Tran, F. Milos, P. Papadopoulos, Y.-K. Chen, E. Venkatapathy, M. Tauber, P. Wercinski, W. Henline, et al. Trajectory, aerothermal conditions, and thermal protection system mass for the mars 2001 aerocapture mission. In *35th Aerospace Sciences Meeting and Exhibit*, page 472, 1997.

[81] M. S. Werner and R. D. Braun. Mission design and performance analysis of a smallsat aerocapture flight test. *Journal of Spacecraft and Rockets*, 56(6):1704–1713, 2019.

[82] T. K. West IV and A. M. Brandis. Stagnation-point aeroheating correlations for mars entry. *Journal of Spacecraft and Rockets*, 57(2):319–327, 2020.

[83] Wikipedia. List of mountains on mars by height, 2023. URL `https://en.wikipedia.org/wiki/List_of_mountains_on_Mars_by_height`.

[84] O. D. Y. W. C. H. F. J. L. D. R. E. E. K. T. Wright, H. S. Mars aerocapture system study. Technical report, NASA, Hampton, Virginia, 11 2006.

[85] S. J. Zhang, B. Açikmeşe, S. S.-M. Swei, and D. Prabhu. Convex programming approach to real-time trajectory optimization for mars aerocapture. In *2015 IEEE Aerospace Conference*, pages 1–7. IEEE, 2015.

[86] E. Zucchelli and E. Mooij. Minimum radiative heat-load aerocapture guidance with attitude-kinematics constraints. In *2018 AIAA Guidance, Navigation, and Control Conference*, page 1319, 2018.

[87] E. M. Zucchelli, G. A. Hanasusanto, B. A. Jones, and E. Mooij. Two stage optimization for aerocapture guidance. In *AIAA Scitech 2021 Forum*, page 1569, 2021.

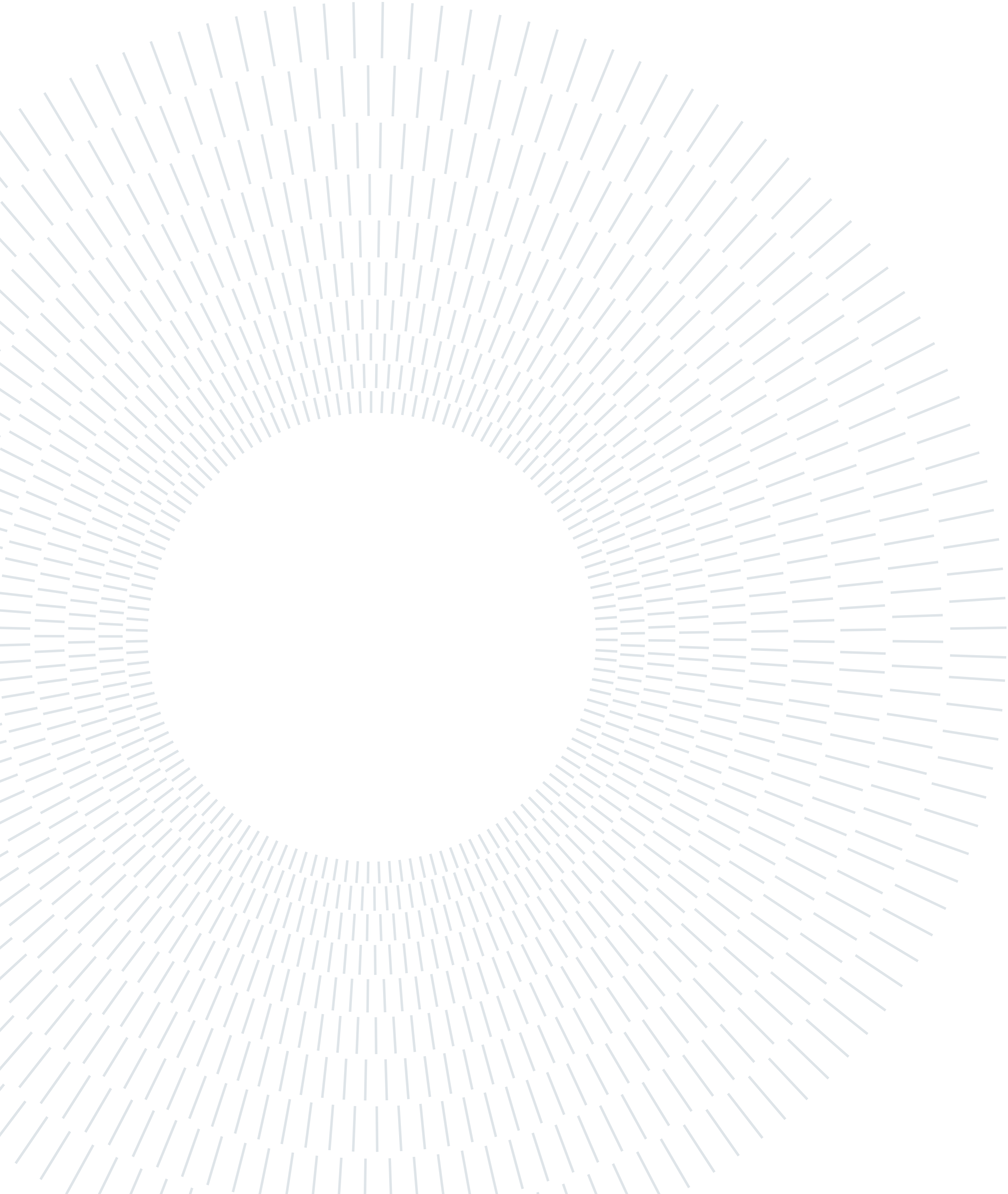

A | Appendix A - Reference Frames and Transformations

A.1. Reference Frames (RF) Definition

Based on definitions provided by [51].

Inertial Planetocentric RF Origin on the planet's centre of mass. The X-Y plane lays on the equatorial plane, and the Z-axis points towards the north pole. The X-axis defines the zero-longitude at initial time.

Rotational Planetorcentric RF Origin on the vehicle's centre of mass, and is coincident with Inertial planetocentric at zero time.

Body RF Origin on the vehicle's centre of mass, X-axis on the plane of symmetry of the spacecraft, and positive on the direction of velocity. Z-axis lies on the vehicle's symmetry plane, positive downwards.

Vertical RF Origin on the planet's centre of mass, Z-axis points towards the centre of mass of the central body. X-axis lies on the meridian plane, pointing towards the northern hemisphere.

Trajectory Ground-Based RF Origin on the vehicle's centre of mass, X-axis towards the velocity vector with respect to the rotating planetocentric reference frame. Z-axis in the vertical plane, pointing downwards.

Trajectory Frame Airspeed-Based RF Equivalent to the Trajectory Ground-Based RF, but the velocity vector is defined with respect to the atmosphere.

Aerodynamic GroundSpeed RF Different with respect to the Trajectory Ground-Based RF on the Z-axis definition, Z-axis is col-linear with the groundspeed-based Lift force vector and opposite direction.

Aerodynamic Airspeed RF Different with respect to the Trajectory Airspeed-Based RF on the Z-axis definition, Z-axis is col-linear with the airspeed-based Lift force vector and opposite direction.

Wind RF X-axis is co-linear with the wind-velocity vector. Z-axis is positive pointing downwards.

A.2. Spherical Components Definitions

Position Components

- r: Distance of the CoM of the SC with respect to the CoM of the central body.
- θ : Measured positive towards the east. Defined as the angle formed by the X-axis rotation planetocentric RF and the projection of r on the equatorial plane.
- ϕ : Positive in north direction. Defined as the angle formed by r with respect to the equatorial plane.

Velocity Components

- V: Groundspeed-based relative velocity with respect to the rotating planetocentric frame.
- γ: Angle formed between the velocity vector and the local horizontal plane, positive when the velocity is above the local horizon.
- ψ : Angle formed by the local north and the projection of the velocity vector into the local horizontal plane. At $\psi = 90[deg]$ the flight is parallel to the equator, and at $\psi = 0[deg]$, the flight is polar.

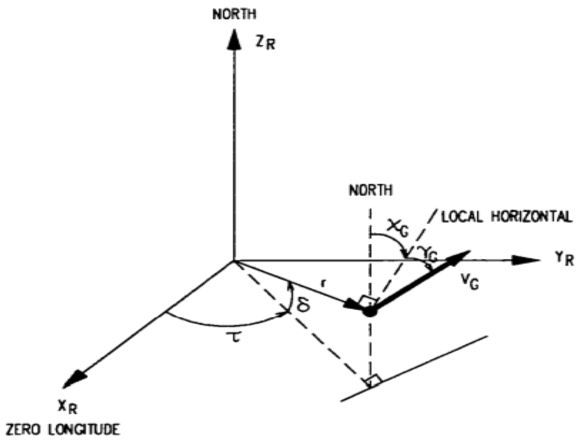

Figure A.1: Spherical Parameters Definition [51]

A.3. Frame Transformations

Unit Axis-Rotations By exploitation of the unit rotation direction cosine matricesprovided for each axis rotation:

$$\boldsymbol{C_1}(\alpha) = \begin{bmatrix} 1 & 0 & 0 \\ 0 & \cos\alpha & \sin\alpha \\ 0 & -\sin\alpha & \cos\alpha \end{bmatrix} \tag{A.1}$$

$$\boldsymbol{C_2}(\alpha) = \begin{bmatrix} \cos\alpha & 0 & -\sin\alpha \\ 0 & 1 & 0 \\ \sin\alpha & 0 & \cos\alpha \end{bmatrix} \tag{A.2}$$

$$\boldsymbol{C_3}(\alpha) = \begin{bmatrix} \cos\alpha & \sin\alpha & 0 \\ -\sin\alpha & \cos\alpha & 0 \\ 0 & 0 & 1 \end{bmatrix} \tag{A.3}$$

Rotating Planetocentric to Inertial Planetocentric $\boldsymbol{C_{I,R}} = \boldsymbol{C_3}(-\omega t)$

Vertical to Rotating Planetocentric Frame $\boldsymbol{C_{R,V}} = \boldsymbol{C_3}(-\theta)\boldsymbol{C_2}\left(\frac{\pi}{2} + \phi\right)$

Wind to Vertical $\boldsymbol{C_{V,W}} = \boldsymbol{C_3}(-\psi_w)\boldsymbol{C_2}(-\gamma_w)$

Trajectory Groundspeed-based to Vertical $\boldsymbol{C_{V,TG}} = \boldsymbol{C_3}(-\psi_G)\boldsymbol{C_2}(-\gamma_G)$

Trajectory Airspeed-based to Vertical $\boldsymbol{C_{V,TA}} = \boldsymbol{C_3}(-\psi_A)\boldsymbol{C_2}(-\gamma_A)$

Aerodynamic Airspeed-based to Trajectory Airspeed-based $\boldsymbol{C_{TA,AA}} = \boldsymbol{C_1}(-\sigma_A)$

Aerodynamic Airspeed-based to Vertical Airspeed-based $\boldsymbol{C_{V,AA}} = \boldsymbol{C_3}(-\psi_A)\boldsymbol{C_2}(-\gamma_A)\boldsymbol{C_1}(-\sigma_A)$

Aerodynamic Airspeed-based to Trajectory Groundspeed-based $\boldsymbol{C_{TG,AA}} = \boldsymbol{C_2}(-\gamma_G)\boldsymbol{C_3}(-\Delta\psi_G A)\boldsymbol{C_2}(-\gamma_A)\boldsymbol{C_1}(-\sigma_A)$ with $\Delta\psi_{GA} = \psi_G - \psi_A$

Body to Aerodynamic Airspeed-Based $\boldsymbol{C_{AA,B}} = \boldsymbol{C_3}(\beta_A)\boldsymbol{C_2}(-\alpha_A)$

Body to Aerodynamic Groundspeed-Based $\boldsymbol{C_{AG,B}} = \boldsymbol{C_3}(\beta_G)\boldsymbol{C_2}(-\alpha_G)$

Vertical to Inertial $\boldsymbol{C_{I,V}} = \boldsymbol{C_3}(\tilde{\theta})\boldsymbol{C_2}\left(\frac{\pi}{2} + \phi\right)$ where $\tilde{\theta} = \theta + \omega t$

B | Aerodynamic Results

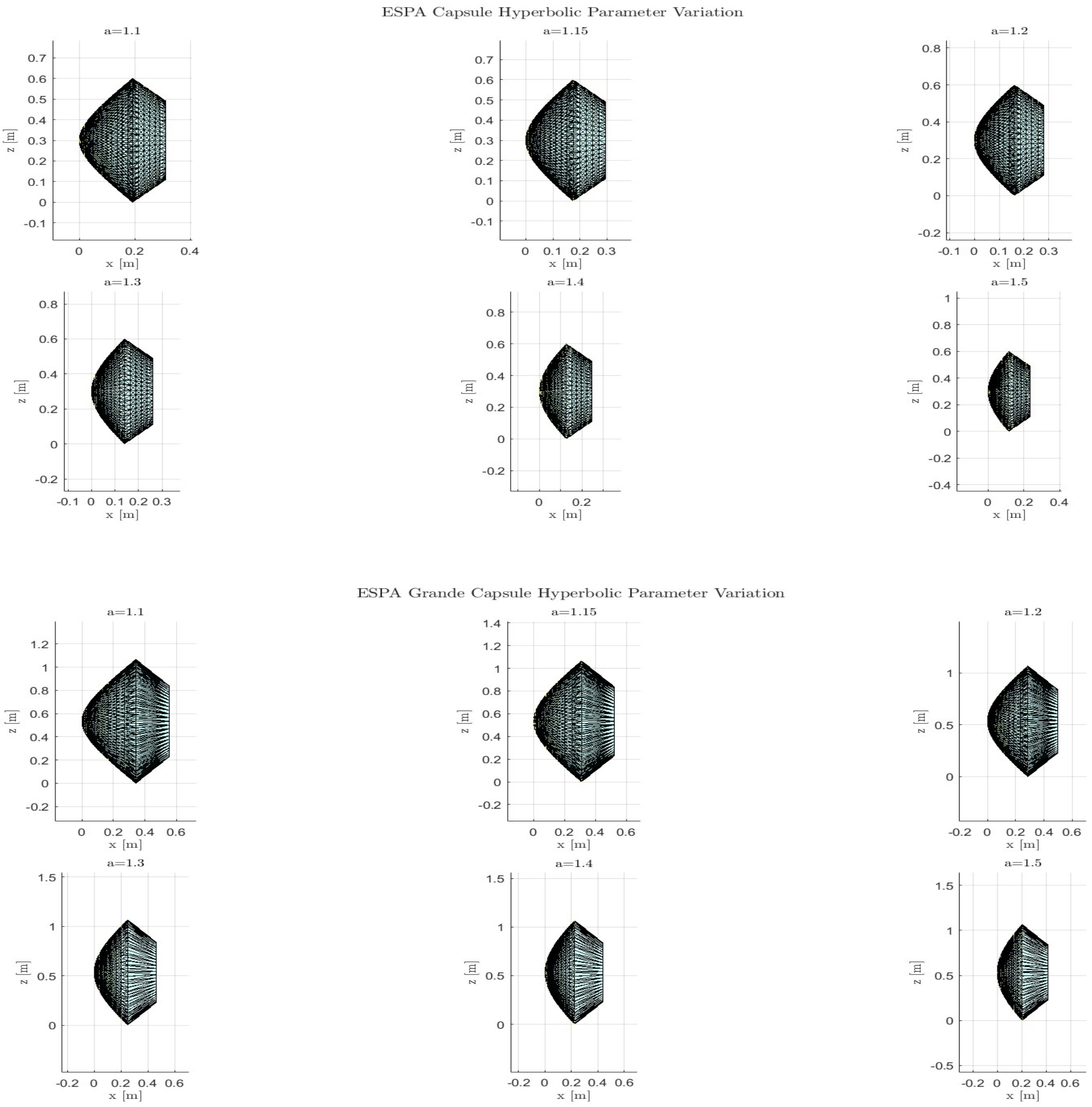

Figure B.1: Capsule Design Iterations with hyperbolic parameter Variation

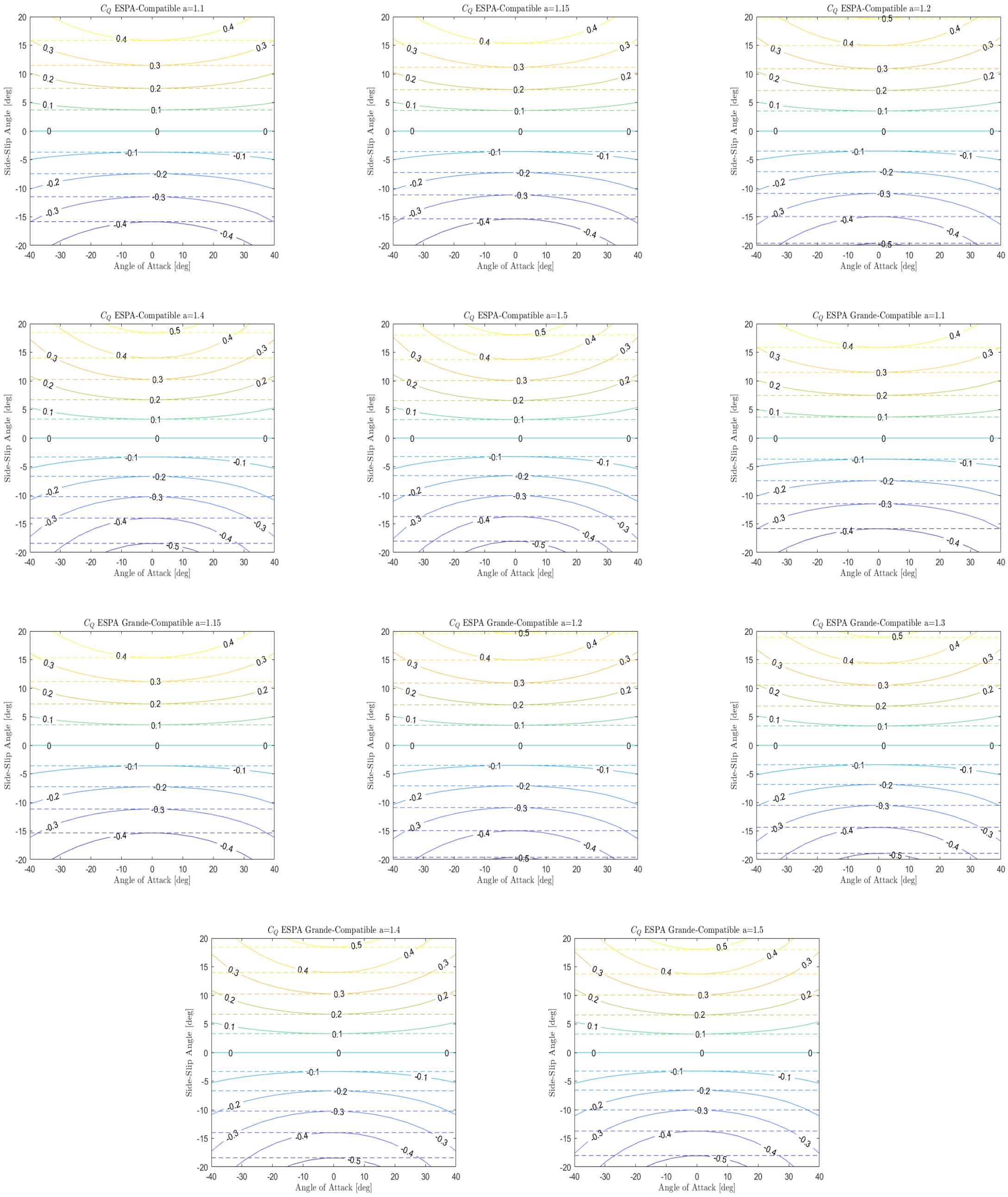

Figure B.2: C_Q ESPA and ESPA Grande compatible capsules

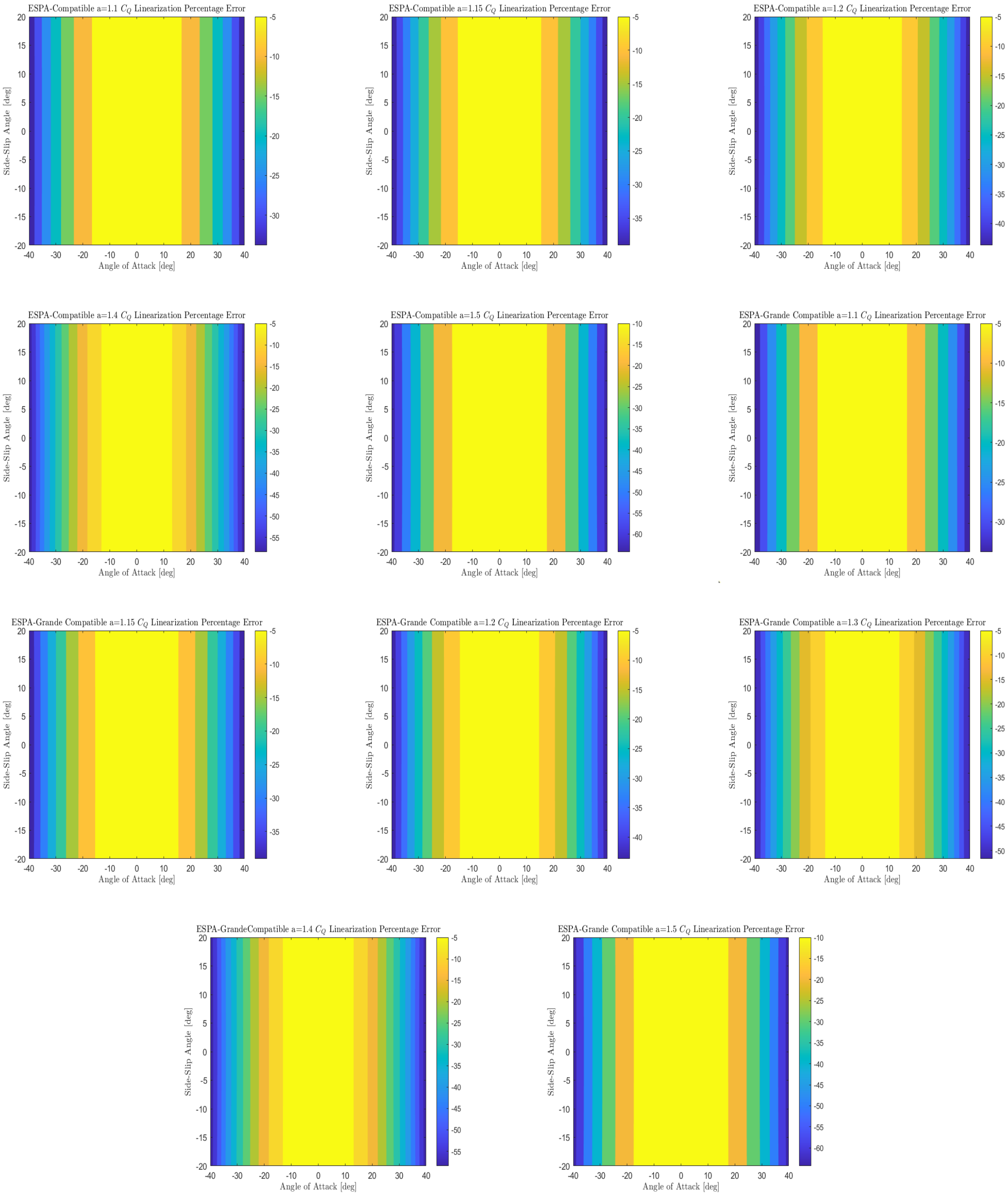

Figure B.3: C_Q Error on ESPA and ESPA Grande compatible capsules

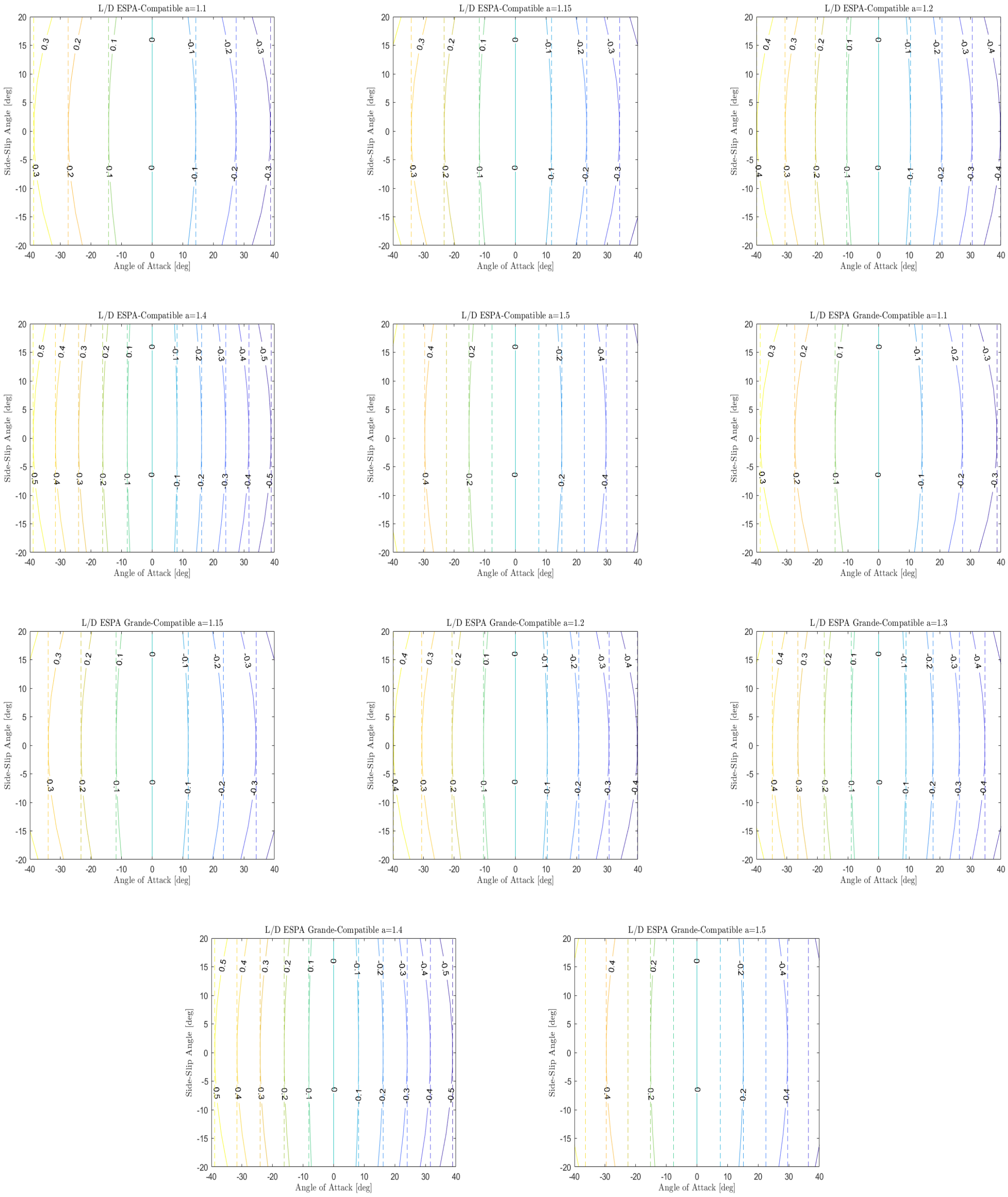
L/D ESPA-Compatible a=1.1
L/D ESPA-Compatible a=1.15
L/D ESPA-Compatible a=1.2
L/D ESPA-Compatible a=1.4
L/D ESPA-Compatible a=1.5
L/D ESPA Grande-Compatible a=1.1
L/D ESPA Grande-Compatible a=1.15
L/D ESPA Grande-Compatible a=1.2
L/D ESPA Grande-Compatible a=1.3
L/D ESPA Grande-Compatible a=1.4
L/D ESPA Grande-Compatible a=1.5

Figure B.4: L/D on ESPA and ESPA Grande compatible capsules

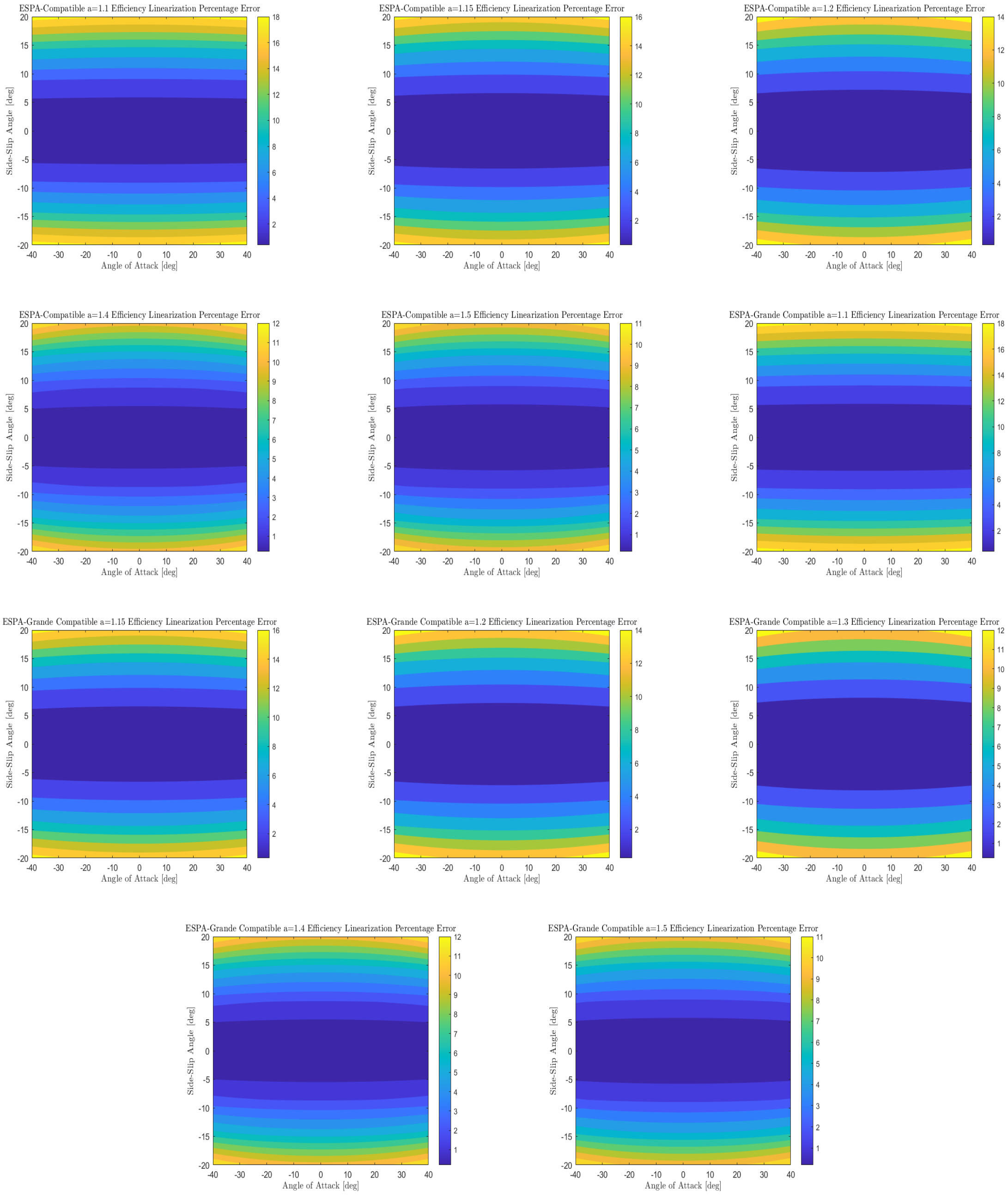

Figure B.5: L/D error on ESPA and ESPA Grande compatible capsules

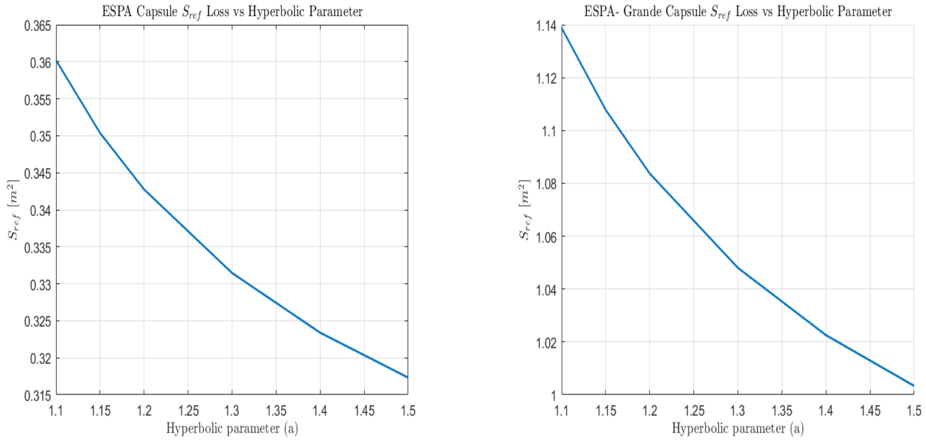

Figure B.6: Reference Surface Loss

C | Transformation between Cartesian and Rotational Components

Position Components The position components transformation is straightforward, and both transformations are provided in Equation C.1 and Equation C.2.

$$\begin{cases} r = \sqrt{x_R^2 + y_R^2 + z_R^2} \\ \theta = \arctan\left(\dfrac{y_R}{x_R}\right) \\ \phi = \arcsin\left(\dfrac{z_R}{\sqrt{x_R^2 + y_R^2 + z_R^2}}\right) \end{cases} \tag{C.1}$$

$$\begin{cases} x_R = r\cos\phi\cos\theta \\ y_R = r\cos\phi\sin\theta \\ z_R = r\sin\phi \end{cases} \tag{C.2}$$

Velocity Components From the Cartesian velocity on the rotational frame, the spherical velocity component is computed from $V = ||\boldsymbol{V_R}||$. By means of the $\boldsymbol{C_{V,R}}$ transformation matrix, the Cartesian velocity is projected into the vertical frame. And the transformation given in Equation C.3 follows. The inverse transformation to obtain the Cartesian components in the vertical frame from the spherical variable is provided in Equation C.4.

$$\begin{cases} \psi = \arctan\left(\dfrac{V_y^v}{V_x^v}\right) \\ \gamma = -\arcsin\left(\dfrac{V_z^v}{V}\right) \end{cases} \tag{C.3}$$

$$\begin{cases} V_x^v = V\cos\gamma\cos\psi \\ V_y^v = V\cos\gamma\sin\psi \\ v_z^v = -V\sin\gamma \end{cases} \tag{C.4}$$

D

Mars Environment Multi-Model (MEMM) Scientific-Tool

The MEMM is a tool that merges different already existing models of the Mars environment, consisting of MarsGram (atmosphere), MarsRad (radiation) and Dycus (meteoroid flux). It coordinates the execution of all the models which are executed as a single cooperative unit.

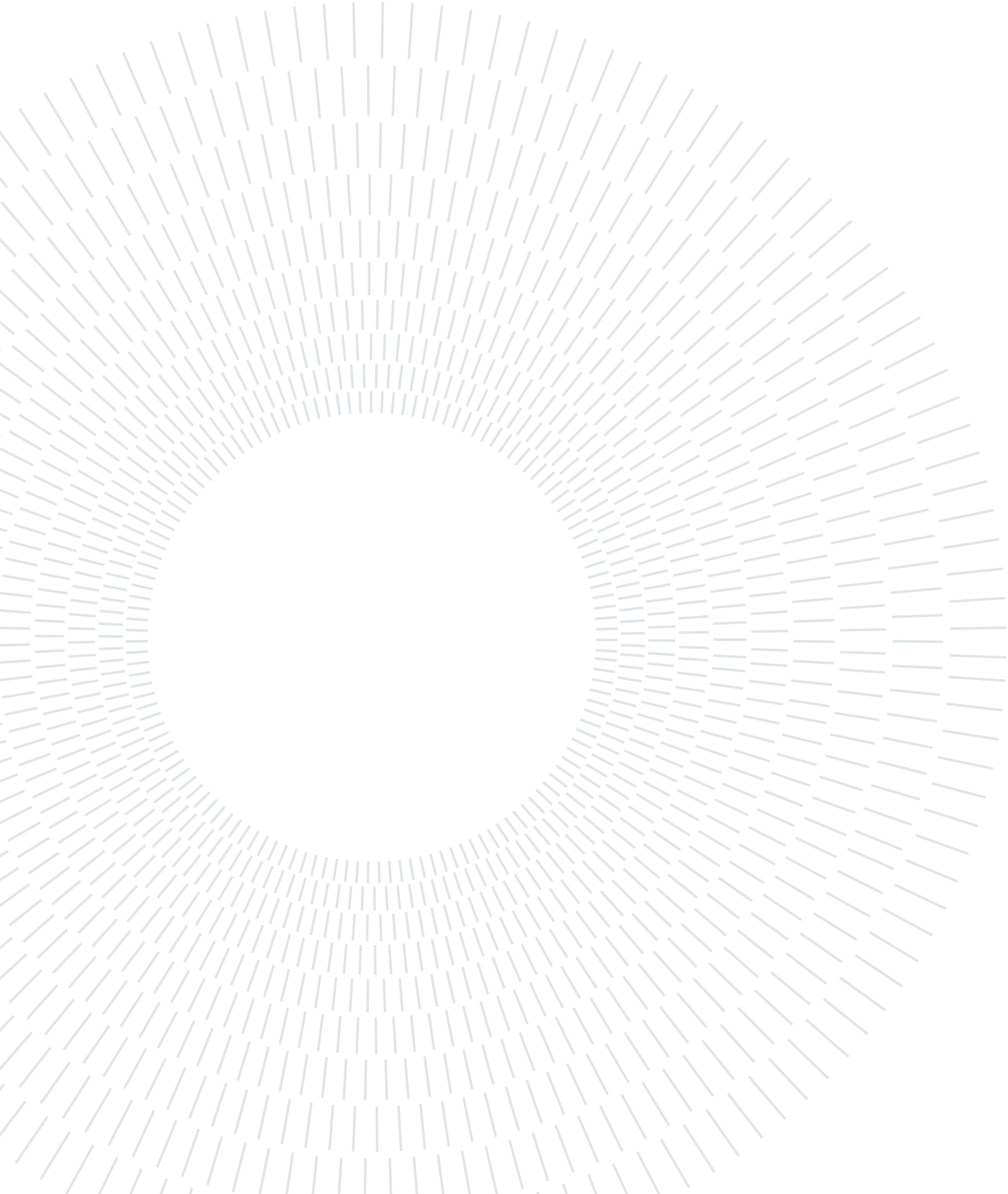The models are based on *Fortran* code, and MEMM is based on *Matlab*. The models are compiled into MEX files and are called by MEMM by exploitation of MEX modules. In this project, MEMM has been used in a wrapper-like mode, to call MarsGram model through the MEMM script that bridges the result to Matlab, which has simplified the operation, configuration and interface with MarsGram model. For the guidance implementation, a script that modified the Trajectory file at each atmospheric call was developed, updating with the trajectory parameter.